Nonlinear optical properties of molecules and metallic nanoparticles for photonics

Hoang Minh Ngo

université PARIS-SACLAY

école normale supérieure paris–saclay

NNT : 2016SACLN050

THESE DE DOCTORAT
DE
L'UNIVERSITE PARIS-SACLAY
PREPAREE A
L'ECOLE NORMALE SUPERIEURE PARIS-SACLAY

ÉCOLE DOCTORALE N°575
Electrical, optical, bio-physics and engineering

Spécialité de doctorat : Physique

Par

M. Hoang Minh NGO

Propriétés optiques non linéaires de molécules et de nanoparticules métalliques pour la photonique

Thèse présentée et soutenue à Cachan, le 15 Novembre 2016 :

Composition du Jury :

Mme. Agnès MAITRE	Professeur, Université Pierre et Marie Curie	Présidente du Jury
M. Eric FREYSZ	Directeur de Recherche CNRS	Rapporteur
Mme. Katarzyna MATCZYSZYN	Professeur assistant, Université de Wrocław	Rapporteur
Mme. Hynd REMITA	Directeur de Recherche CNRS	Examinatrice
M. Joseph ZYSS	Professeur, ENS Cachan	Examinateur
Mme. Isabelle LEDOUX-RAK	Professeur, ENS Cachan	Directrice de thèse

Résumé

L'optique non linéaire est un outil très puissant pour l'étude des propriétés photoniques de molécules, de matériaux et de nanostructures. La taille et la forme des nanoparticules de métaux nobles (NMNPs) influencent fortement leurs propriétés optiques non linéaires du second ordre. Dans cette thèse, nous proposons une étude systématique de l'influence de la surface de nanoparticules sur leurs valeurs de première hyperpolarisabilité β. Des nanoparticules en poudre d'argent (de diamètres ~7 nm) ainsi que des solutions colloïdales sur NMNPs -avec différentes compositions, tailles et formes -ont été synthétisés : des nanosphères d'argent (de diamètres ~10 nm), des nanosphères d'or (de diamètres 3,0; 11,6; 15,8; 17,4; 20,0 et 43,0 nm), des nanobâtonnets d'or (de rapports d'aspect 1,47; 1,63 et 2,30), des nanobâtonnets d'argent (de rapports d'aspect 5,0; 6,3; 7,5; 8,2 et 9,7), des nanofleurs de platine (de diamètres 7,0; 8,0; 10,0; 14,0; 20,0 et 31,0 nm) ainsi que des nanoprismes d'or (d'une longueur de côtés de 47,5 à 112,3 nm). La diffusion harmonique de la lumière (HLS) à 1064 nm est utilisée pour étudier la génération du second harmonique des NMNPs colloïdaux, et d'en déduire leurs valeurs de première hyperpolarisabilité β. Pour les nanosphères et les nanorods étudiés dans ce travail, nous démontrons que leurs valeurs de β présentent une forte dépendance avec leur surface, qui est le paramètre dominant dans l'évolution des valeurs de β. Par ailleurs, la rugosité de la surface des particules ainsi que la forme des irrégularités des nanofleurs sont responsables de valeurs exceptionnellement élevées de β. En outre, nous démontrons expérimentalement, pour la première fois dans la littérature, que les valeurs de β des nanoprismes présentent non seulement une dépendance linéaire par rapport à la surface, mais sont également sensibles aux courbures des sommets du triangle.

Abstract

Nonlinear optics is well known to be a highly powerful tool to investigate the photonic properties of molecules, materials and nanostructures. Size and shape of noble metal nanoparticles (NMNPs) strongly influence their second-order nonlinear optical properties. In this PhD thesis, we propose a systematic investigation of the influence of the nanoparticle surface area on their first hyperpolarizability β values. Powdery-silver nanoparticles (diameters ~7 nm) and colloidal solutions on NMNPs with different composition, sizes and shapes have been synthesized, *i.e.* silver nanospheres (diameters ~10 nm), gold nanospheres (diameters 3.0; 11.6; 15.8; 17.4; 20.0 and 43 nm), gold nanorods (aspect ratios 1.47; 1.63 and 2.30), silver nanorods (aspect ratios 5.0; 6.3; 7.5; 8.2 and 9.7), platinum nanoflowers (diameters 7.0; 8.0; 10.0; 14.0; 20.0 and 31.0 nm) and gold nanoprisms (edge length tuned from 47.5 to 112.3 nm). Harmonic light scattering (HLS) at 1064 nm is used to investigate the second harmonic generation from colloidal NMNPs, and to infer their first hyperpolarizability tensor β. For the nanospheres and nanorods investigated in this work, we demonstrate that their β values display a strong dependence with their surface area, which is the dominant parameter in the evolution of β values. Otherwise, particle surface corrugation and shape irregularities of nanoflowers are responsible for exceptionally high β values. Moreover, we report for the first time in the literature that the β values of nanoprisms display not only a linear dependence with respect to the surface area, but are also sensitive to the sharpness of the triangle vertices.

Acknowledgements

Firstly, I would like to express my deepest regard and heartfelt gratitude to my graduate supervisor, Prof. Isabelle LEDOUX-RAK for all her support and guidance, sentiment and kindness. Her wide knowledge and her detailed and constructive comments have been of great value for me. Her understanding, encouraging and personal guidance have provided a good basis for the present thesis. My research with her for the last three years has been a wonderful experience.

I wish to express my warm and sincere thanks to Prof. Joseph ZYSS, Assoc. Prof. Ngoc Diep LAI and Assoc. Prof. Phuong Phong NGUYEN for their orientations and fruitful discussions.

Besides I would like to thank all researching members of Quantum and Molecular Photonics Laboratory (LPQM) for their guidance, discussions, and friendship. They have made a friendly and harmonious environment in which to work and study.

Last but not least, I am most grateful and wish to offer my sincere thanks to my parents, younger brother and fiancée who always encourage me in my life. I dedicate this thesis to my parents.

Table of Contents

List of Publications

Parts of the thesis have been published in:

- **H. M. Ngo**, T. T. Luong, M. H. Luong, I. Ledoux-Rak and J. Zyss. Quadratic nonlinearities of gold nanoprisms in solution. (*submitted 2016*).
- **H. M. Ngo**, T. T. Luong and I. Ledoux-Rak. Surface area-dependent second harmonic generation from silver nanorods. *Phys. Chem. Chem. Phys.* **18**, 23215-23219 (2016).
- **H. M. Ngo**, N. D. Lai, and I. Ledoux-Rak. High second-order nonlinear response of platinum nanoflowers: the role of surface corrugation. *Nanoscale* **8**, 3489–3495 (2016).
- **H. M. Ngo**, P. P. Nguyen, and I. Ledoux-Rak. Optimization of second harmonic generation of gold nanospheres and nanorods in aqueous solution: the dominant role of surface area. *Phys. Chem. Chem. Phys.* **18**, 3352–3356 (2016).
- **H. M. Ngo** and I. Ledoux-Rak. Second harmonic generation from silver nanoparticles in aqueous solution with different protective agents. *Proc. SPIE **9171**, Nanobiosystems: Processing, Characterization, and Applications VII,* 91710Y (2014).

Related publications with author's contribution

- D. T. T. Nguyen, T. H. Au, Q. C. Tong, M. H. Luong, A. Pelissier, K. Montes, **H. M. Ngo**, M. T. Do, D. B. Do, D. T. Trinh, T. H. Nguyen, B. Palpant, C. C. Hsu, I. Ledoux-Rak, and N. D. Lai. Coupling of a single active nanoparticle to a polymer-based photonic structure. *J. Sci. Adv. Mater. Devices* **1,** 18–30 (2016).
- R. Ayadi, J. Lhoste, **H. M. Ngo**, I. Ledoux-Rak, T. Mhiri, M. Boujelbene. Spectral and nonlinear optical studies of Propane-1, 3-diaminium nitrate. *Journal of Crystal Growth* **448**, 36–43 (2016).
- D. T. T. Nguyen, A. Pelissier, K. Montes, Q. C. Tong, **H. M. Ngo**, I. Ledoux-Rak, and N. D. Lai. Deterministic embedding of a single gold nanoparticle into polymeric microstructures by direct laser writing technique. *Proc. SPIE **9884**, Nanophotonics VI,* 98842C (2016).

- C. P. Gros, C. Michelin, G. Depotter, N. Desbois, K. Clays, Y. Cui, L. Zeng, Y. Fang, **H. M. Ngo**, C. Lopez, I. Ledoux-Rak, J. F. Nicoud, F. Bolze and K. M. Kadish. Non-linear optical, electrochemical and spectroelectro- chemical properties of amphiphilic inner salt porphyrinic systems. *J. Porphyrins Phthalocyanines* **20**, 1–14 (2016).
- M. T. Do, D. T. T. Nguyen, **H. M. Ngo**, I. Ledoux-Rak, and N. D. Lai. Controlled coupling of a single nanoparticle in polymeric microstructure by low one-photon absorption—based direct laser writing technique. *Nanotechnology* **26,** 105301 (2015).
- A. Merhi, G. Grelaud, K. A. Green, **H. M. Ngo**, M. Reynolds, I. Ledoux-Rak, A. Barlow, G. Wang, M. P. Cifuentes, M. G. Humphrey, F. Paul, and C. O. Paul-Roth. A hybrid ruthenium alkynyl/zinc porphyrin "Cross Fourchée" with large cubic NLO properties. *Dalton Trans.* **44,** 7748–7751 (2015).
- Z. Csók, P. Szuroczki, L. Kollár, **H. M. Ngo**, I. Ledoux-Rak, N. A. M. S. Caturello, and R. Q. Albuquerque. Intramolecular Cooperative Effects in Multichromophoric Cavitands Exhibiting Nonlinear Optical Properties. *J. Phys. Chem. C* **119,** 12608–12615 (2015).
- N. Novoa, T. Roisnel, P. Hamon, S. Kahlal, C. Manzur, **H. M. Ngo**, I. Ledoux-Rak, J.-Y. Saillard, D. Carrillo, and J.-R. Hamon. Four-coordinate nickel(II) and copper(II) complex based ONO tridentate Schiff base ligands: synthesis, molecular structure, electrochemical, linear and nonlinear properties, and computational study. *Dalton Trans.* **44,** 18019–18037 (2015).

Conference attended and contributions

- **Summer School** MONABIPHOT 2016 organized by Erasmus Mundus from 26 June to 02 July, 2016, Anglet, France.
- D. T. T. Nguyen, A. Pelissier, K. Montes, Q. C. Tong, **H. M. Ngo**, I. Ledoux-Rak, and N. D. Lai. Deterministic embedding of a single gold nanoparticle into polymeric microstructures by direct laser writing technique. **Poster**, SPIE Photonics Europe 2016, Brussels, Belgium (April 2016).
- D. T. T. Nguyen, A. Pelissier, K. Montes, M. T. DO, Q. C. Tong, **H. M. Ngo**, I. Ledoux-Rak, and N. D. Lai. Precisely embedding a single gold nanoparticle into

polymer photonic structure by LOPA direct laser writing. **Poster**, Optic Bretagne, Rennes, France (July 2015).

- **Summer School** MONABIPHOT 2015 organized by Erasmus Mundus from 21-27 June, 2015, Anglet, France.
- **H. M. Ngo**, and I. Ledoux-Rak. Second harmonic generation from silver nanoparticles power. **Poster**, French Israeli Symposium on Non-linear & Quantum Optics (FRISNO13), Aussois, France (March 2015).
- **H. M. Ngo** and I. Ledoux-Rak. Second harmonic generation from silver nanoparticles in aqueous solution with different protective agents. **Poster**, SPIE Optics + Photonics, California, United States (August 2014).

Introduction

One of the most attractive properties of noble metal nanoparticles (NMNPs) is their large optical second-order nonlinearities. Huge hyperpolarizabilities have been reported in numerous publications in relation with their localized surface plasmon resonance. In this work, we want first to consolidate the already existing results for gold and silver nanospheres, by performing a systematic investigation of size effect on their nonlinear optical (NLO) responses, especially for gold particles for which a large number of data is already available. In that respect, we have explored the upper and lower limits of particle diameters corresponding to a dipolar origin of the second harmonic response. The validity of this dipolar hypothesis has been tested by systematic studies of the dependence of hyperpolarizabilities with respect to gold nanosphere surface area on one hand, and by a verification of the dipolar response by performing harmonic light scattering (HLS) polar plots on the other hand. Then we have extended our investigations of nanoparticles beyond gold and silver nanospheres (AuNSs and AgNSs), towards more specific geometries: gold and silver nanorods (AuNRs and AgNRs), platinum nanoflowers (PtNFs) and gold nanotriangles or nanoprisms (AuNPrs), the rationale of this presentation being to extend quadratic NLO studies of NMNPs to new metals and geometries, *i.e.* to non-spherical objects and finally to non-centrosymmetric ones. Their first hyperpolarizabilities have been measured in water by HLS at 1064 nm, using the set-up described above.

The present thesis is organized as follow:

- In Chapter 1, we briefly introduce nonlinear optics and noble metal nanomaterials for photonics as well as their optical properties.

- In Chapter 2, we summarize some of the methods used for the fabrication of NMNPs and outline some investigation tools used to characterize the structure and nonlinear optical properties of NMNPs.

- Chapter 3 is devoted to the synthesis, structural and NLO studies of AuNSs and AgNSs. The objectives of this part are 3-fold:
  a) To perform a systematic investigation of the NLO response of AuNSs with different diameters, in order to identify the limits of the dipolar nonlinear response of these nano-objects. It is expected that the upper limit is related to the emergence of multipolar contributions beyond the pure Rayleigh scattering limit (non-local effects), the lower one corresponding to a decrease of the metallic character of nanoparticles containing small number of metal atoms.
  b) To explore the possibility to stabilize over several months the stability of colloidal AgNSs, which are known to be less stable than gold ones in water solutions
  c) To evidence, for the first time to the best of your knowledge, a strong SHG emission from "dry", powdery metallic nanoparticles, especially powdery AgNSs fabricated by thermal decomposition and characterized by a Kurtz and Perry Powder test using a set-up similar to HLS.

- Chapter 4 is devoted to the synthesis, structural and NLO studies of AuNRs and AgNRs. This particle geometry is now widely used because nanorods absorb in the near IR, and generate heat when excited with IR light, then making them interesting for cancer treatment. If these nanorods can be incorporated to tumor cells, the patient can be exposed to IR light (which passes through body tissue), and nanorods located tumor cells are locally heated, leading to the death of cancerous tissues only, while leaving healthy parts of the body intact.

  As recent studies conducted in our lab had evidence the influence of nanorod aspect ratio on their quadratic nonlinear properties, we decided to perform a more systematic study of AuNRs and AgNRs (no second-order NLO characterization having been reported yet for the latter ones) in order to explore other effects, such as nanoparticle surface area, and to compare the respective hyperpolarizabilities of AuNRs and AgNRs. For this purpose, colloidal solutions of AuNRs (aspect ratios 1.47; 1.63 and 2.30) have been synthesized by the seed-mediated method, and colloidal solutions of AgNRs with various average values of aspect ratios (5.0; 6.3; 7.5; 8.2 and 9.7) have been elaborated using a rapid one-pot seedless growth method.

- Chapter 5 is dedicated to present, for the first time, a large hyperpolarizability β values of PtNFs. Highly corrugated surface for nanoparticle with irregular shape seem to be the dominant factor governing these exceptionally high β values. These nanoflowers have been synthesized in aqueous solution for six different diameters (~7.0; 8.0; 10.0; 14.0; 20.0 and 31.0 nm) by chemical reduction and seed-mediated methods.

- In Chapter 6, noncentrosymmetric AuNPrs with various edge lengths, ranging from 47.5 to 112.3 nm, have been elaborated by using a seedless growth method. As expected, these nanotriangles display higher hyperpolarizability values than centrosymmetric AuNPs showing a similar surface area, and displayed a linear dependence with respect to the surface area. However, other measurements performed on AuNPrs with smoother corners, did not confirm this superiority of acentric nanoparticles over centrosymmetric ones then suggesting that the significant increase of β values for "sharp corner" nanoprisms originates from sharp tip effects rather than from symmetry considerations.

Finally, the main results obtained within the frame of the thesis are discussed in terms of further additional studies to be implemented beyond the present work, together with potential perspectives which can be further investigated and exploited in the near future.

Chapter 1
Nonlinear optics and noble metal nanoparticles: general presentation

Part A. Introduction to nonlinear optical (NLO) materials

1.1. Overview of nonlinear optics

Nonlinear optics is the study of phenomena related to the modification of the optical properties of a molecule or a material system by the presence of light. However, only laser light is sufficiently intense to modify the optical properties of a material system. As a consequence, all-optical nonlinear optical (NLO) effects were not discovered until the discovery of lasers. The starting point of experimental nonlinear optics is associated to the first evidence of second harmonic generation (SHG) by Franken *et al.* (1961)[1] from a quartz crystal pumped by a ruby laser beam, shortly after the invention of the laser by Maiman in 1960.[2] Nonlinear optics is the study of the interactions of light with matter under conditions involving a significant modification of the matter optical response induced by light itself. The propagation of a wave through a material produces changes in the spatial and temporal distribution of electrical charges as electrons and atoms interact with the electromagnetic fields of the wave. The main effect of the forces exerted by the field on charged particles is the displacement of the valence electrons from their normal orbits. This perturbation creates electric dipoles whose macroscopic manifestation is the polarization. Thus, interaction of intense electromagnetic field with materials produce modified fields that are different from the input field in phase, frequency or amplitude. For example, SHG occurs as a result of the part of the atomic response that scales quadratically with the strength of the applied optical

field. Consequently, the intensity of the light generated at the second harmonic frequency tends to increase as the square of the intensity of the applied laser light.[3]

When a material is submitted to an oscillating external electric field, its electro-magnetic response is usually described by the induced electrical polarization. In the case of linear optics, in the presence of a relatively weak electromagnetic field, this polarization is proportional to the amplitude of the applied field.[3–5]

$$P = \varepsilon_0 \chi^{(1)} E \tag{1.1}$$

where P is the polarization vector, E is the electric field vector, the $\chi^{(1)}$ tensor is known as the linear susceptibility and ε_0 is the permittivity of free space.

In nonlinear optics, when the optical electric field strength is very high and comparable to the intra-atomic electric field, the induced polarization is given by

$$P = \varepsilon_0 \left[\chi^{(1)} E + \chi^{(2)} E^2 + \chi^{(3)} E^3 + ... \right] \tag{1.2}$$

$$\equiv P^{(1)} + P^{(2)} + P^{(3)} + ...$$

where $\chi^{(2)}$ and $\chi^{(3)}$ are second and third order nonlinear optical susceptibilities. $P^{(2)}$ and $P^{(3)}$ are second and third order nonlinear polarization. Examples of second order $\chi^{(2)}$ processes are sum frequency generation (SFG) ($\omega_3 = \omega_1 + \omega_2$) and difference frequency generation ($\omega_3 = \omega_1 - \omega_2$), where SHG ($\omega_2 = 2\omega_1$) is a special case of sum frequency generation. The most commonly employed third order $\chi^{(3)}$ processes are third harmonic generation (THG) ($\omega_2 = 3\omega_1$) and four-wave mixing ($\omega_3 = 2\omega_1 - \omega_2$).

On the single molecule level, the polarization leads to nonlinear effect and can be expressed as

$$P = \alpha_{ij} E_j + \beta_{ijk} E_j E_k + \gamma_{ijkl} E_j E_k E_l + ... \tag{1.3}$$

where,

α_{ij} : linear polarizabilities

β_{ijk} : first hyperpolarizability (second order effects)

γ_{ijkl} : second hyperpolarizability (third order effects)

i,j,k,l correspond to the molecular coordinates

Nonlinear optics impacts a wide range of technical fields, including optical communications, fiber optics, ultrafast lasers, quantum computing, ultra-cold atoms, plasma physics, particle accelerators, *etc*. Both chemistry and biology are increasingly using investigation tolls based on nonlinear optics. Nonlinear optics applies to numerous specific applications, such as in fiber optics, spectroscopy, photo-refractivity, liquid crystals, polymers, semiconductors, organics, switching, ultraviolet, X-rays, quantum optics, telecommunications, signal processing, and so on.

1.2. Second harmonic generation (SHG)

Within the last decades, various types of second order NLO processes, including SHG, SFG or difference frequency generation, linear electro-optic effect or Pockels effect and optical rectification, have been observed in plasmonic nanostructures, emphasizing their great potential to design advanced nonlinear nanosources of light and to manipulate light at small scales.

One of the most intensively studied NLO phenomena is SHG corresponding to second-order NLO properties. SHG is a second-order nonlinear optical process, whereby two photons at the fundamental frequency ω_1 (corresponding to the frequency of the incident light) are converted into one photon at the second harmonic frequency ($\omega_2 = 2\omega_1$) (see Figure 1.1).

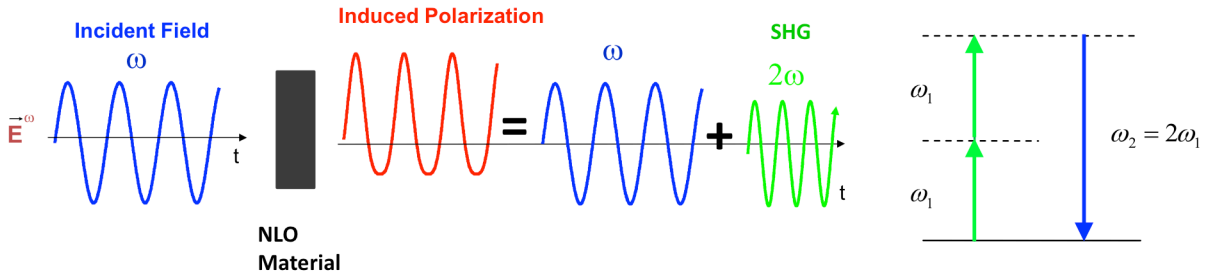

Figure 1.1 *Diagram of the SHG process (left) and energy level diagram (right) of SHG.*

According to a classical electromagnetic description, the source to the SHG light is the nonlinear polarization $P^{(2)}(\omega_2)$ oscillating at the second harmonic frequency.[3] In the electric dipole approximation, the nonlinear polarization results from the interaction of the fundamental electric field $E(\omega_1)$ with the nonlinear medium, via the second order nonlinear susceptibility tensor $\chi^{(2)}$:

$$P^{(2)}(\omega_2) = \varepsilon_0 \chi^{(2)} E^2(\omega_1) \tag{1.4}$$

For a centrosymmetric material, if the sign of optical field is changed from *E* to -*E*, the sign of polarization must also change reversely due to the inversion symmetry. Hence,

$$-P^{(2)}(\omega_2) = \varepsilon_0 \chi^{(2)} \left[-E(\omega_1)\right]^2 = \varepsilon_0 \chi^{(2)} E^2(\omega_1) \tag{1.5}$$

where $-P^{(2)}(\omega_2) = P^{(2)}(\omega_2)$, which can only occur if $P^{(2)}(\omega_2) = 0$ .This demonstrates that the nonlinear susceptibility $\chi^{(2)}$ must vanish in centrosymmetric media. Thus, SHG is forbidden in the bulk face-centered cubic metals such as gold, platinum, and silver. On the contrary, noncentrosymmetric materials possess a nonzero $\chi^{(2)}$, resulting in the emission of SHG signals.

Under proper experimental conditions, (phase-matching) the process of SHG can be so efficient that up to 50% of the power of the incident beam at frequency ω is converted to radiation at the second harmonic frequency 2ω. A common use of SHG is to convert the output of a fixed-frequency laser to a different spectral region. For example, the Nd: YAG laser operates in the near infrared at a wavelength of 1064 nm. SHG is routinely used to convert the wavelength of the radiation to 532 nm, in the middle of the visible spectrum.

The SHG method is widely used for NLO analysis of films and interfaces. For NLO analysis of species in solution, the SHG technique named harmonic light scattering (HLS, so-called hyper-Rayleigh scattering) is the most suitable one. While HLS was experimentally demonstrated in 1965,[6] it became popular decades later as a tool to measure the first hyperpolarizabilities tensor β for solution species.[7] Currently, this is the most effective and versatile technique to determine β values, both for molecules and nanoparticles.[8–24]

1.3. Materials for nonlinear optics

At the end of the 1960's, the Kurtz and Perry powder SHG method was introduced.[25] For the first time, a rapid, but still qualitative evaluation for second order NLO effects was possible. The set-up was set for a quick screening of new materials, both inorganic and organic. The early history summarized here is based on a more extensive book authored by D. S. Chemla and J. Zyss[26] and entitled "Nonlinear Optical Properties of Organic Molecules and Crystals". The development of NLO materials has been driven by a multitude of important technological applications that can be realized if suitable materials are available. Future generations of optoelectronic devices for telecommunications, information storage, optical switching, and signal processing are based, to a large extent, on the development of novel materials with exceptional NLO responses, *e.g.* conversion of light wavelength, amplification of light, and modification of the refractive index with respect to optical intensity. Various NLO materials have been investigated both experimentally and theoretically, including inorganic or organic crystals, semiconductor or metal nanostructures, polymer thin films, chiral surfaces, *etc*.[3–5,26–32]

1.3.1. Molecular engineering: Dipoles and Octupoles

The vast majority of molecular compounds that possess large β values contain conjugated π-systems with donor (D) and acceptor (A) moieties (see Figure 1.2). The linear optical properties of such dipolar, polarizable molecules are characterized by low energy, intramolecular charge transfer (ICT) transitions. Over the past decades, much work has been focused towards the optimization of their β values.[26,27,33]

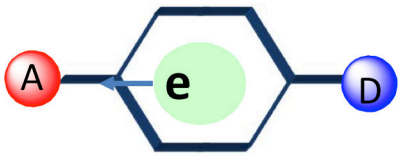

Figure 1.2 *Typical electronic structure of nonlinear, dipolar push-pull molecules (A = Electron-Acceptor group, D = Electron-Donor group).*

Nonlinearities can be enhanced by either increasing the conjugation length between the donor and acceptor group (and or by improving delocalization) or by increasing the strength

of donor or acceptor groups (improving electron asymmetry). The position and number of acceptor and donor groups in the molecule play also an important role.[26]

In addition to push-pull dipolar molecules, a recently new strategy was introduced for second generation of compounds. Studies based on group theory and quantum mechanics have built-up the theoretical basis of the field of non-dipolar molecules for nonlinear optics, which became known as octupolar, and more generally multipolar molecules. The concept of octupolar nonlinearities was described in the early 1990 by Zyss.[5,34,35]

Basically, purely octupolar symmetries can be derived from a cubic structure made of alternate positive and negative charges located a corners of a cube. A projection of these charges along a plane perpendicular to the C_3 axis of the cube, gives rise to D_{3h} or D_3 symmetry (TATB route) systems, *i.e.* two-dimensional (2D) octupolar materials, or by the fusion of one type of charge in the barycenter of the cube, leading to T_d, or D_{2d} symmetry like tetrahedral metal complexes or substituted biphenyls, *i.e.* three-dimensional (3D) octupolar materials (see Figure 1.3). Thus, the molecular engineering of octupoles is based on a spatially controlled organization of charge transfers within a molecule compatible with a non-polar symmetry.

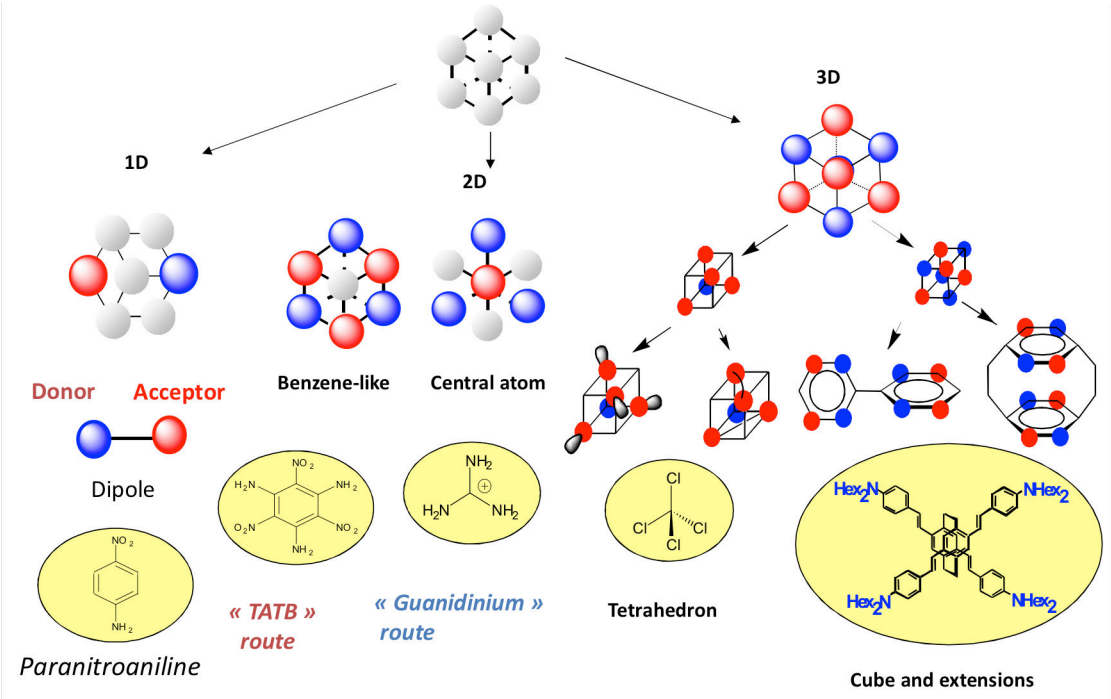

Figure 1.3 *From 1-D to 3-D molecular templates for multipolar molecular engineering.*[35]

1.3.2. Inorganic NLO materials

The search for nonlinear optical materials began soon after the demonstration of second-harmonic generation of light in quartz crystal by Franken *et al.* (1961)[1]. Inorganic materials exhibiting second-order NLO properties have attracted interest in the recent past due to their ability to be processed into crystals, their wide optical transparency domain, their large nonlinear figure of merit for frequency conversion, their fast optical response time and wide phase-matching angular acceptance.[27] These ionic-bonded inorganic crystals are easy to synthesize, and to grow and they have a high melting point and high degree of thermal and chemical stability.[36,37] Studies were concentrated on inorganic materials such as lithium niobate ($LiNbO_3$),[38] potassium niobate ($KNbO_3$),[39] potassium dihydrogen phosphate (KH_2PO_4, KDP),[40] potassium titanyl phosphate ($KTiOPO_4$, KTP),[41] barium titanate ($BaTiO_3$)[42] and zinc oxide (ZnO)[43]. More recently, several typical borate derivatives, including β-BaB_2O_4 (BBO), LiB_3O_5 (LBO),[44] $Sr_2B_2Be_2O_7$ (SBBO),[45] BiB_3O_6 (BiBO)[46] and the latest $Ca_4LnO(BO_3)_3$ (CLnOB, where Ln = Gd, La, Y)[47] with different chemical bonding structures of boron atoms are investigated as promising NLO crystals. The family of the various borate crystals thus plays a very important role in the field of nonlinear optics.[48] NLO semiconductors materials are gallium arsenide[49] or cadmium selenide[50], which are mostly used as quantum dots.

These crystals played an important role in the development of nonlinear optics as a major area of laser science and of techniques such as harmonic generation, frequency mixing and parametric generation as viable methods for generating coherent radiation in new regions of the optical spectrum. Many of these materials have also been successfully used in commercial frequency doublers, mixers and parametric generators to provide coherent laser radiation with high frequency conversion efficiency in new regions of the spectrum, which are inaccessible by other conventional nonlinear crystal sources.[37,51] For example, KDP, potassium dideuterium phosphate (KD_2PO_4, DKDP) and ammonium dihydrogen phosphate ($NH_4H_2PO_4$, ADP) are widely used as second, third and fourth harmonic generators for Nd:YAG and Nd:YLF lasers (see Figure 1.4). The crystals are also widely used for electro-optic applications as Q-switches for Nd:YAG, Nd:YLF, Ti:Sapphire and Alexandrite lasers, as well as for Pockels cells and as for acousto-optic applications. The most commonly used electro-optic crystal is DKDP with a deuteration rate higher than 98%. These crystals are grown by a water-solution method and can be reach very large sizes (thousands of cm^3). Therefore, low-

cost and large-size nonlinear components are currently available. For frequency doubling (SHG) and tripling (THG) of Nd:YAG laser at 1064 nm, both type I and type II phase-matching configurations can be employed for KDP and DKDP. For frequency quadrupling (4HG, output at 266 nm) of Nd:YAG laser, KDP crystal is normally recommended.

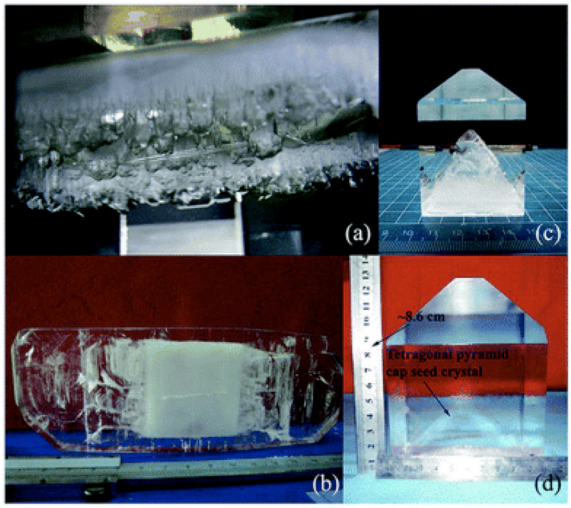

Figure 1.4 *Photograph of ADP crystals grown on (a) a Z-cut KDP seed crystal, (b) an X-cut KDP seed crystal, (c) an ADP seed crystal and (d) a tetragonal pyramid as seed crystal.*[52]

However, inorganic materials also show some drawbacks, as their optical nonlinearity remains modest. Moreover, they display a large dispersion of their dielectric constant within the electro-magnetic spectrum (from GHz to the optical domain), then limiting the bandwidth of electro optic modulations to a few tens of GHz).

1.3.3. Organic NLO materials

As an alternative to inorganic materials, organic molecules and polymers can suppress the limitations identified above and have been investigated widely due to their high nonlinear optical properties, rapid response in electro-optic effect and large second or third order hyperpolarizibilities compared to inorganic NLO materials. The NLO effects in organic materials are usually electronic in nature, which leads to a fast nonlinear response. Benzopyrene was the first observation of SHG in an organic material by Rentzepis and Pao[53] in 1964. In the same year, SHG from a hexamethylenetetramine single crystal was evidenced.[54] Soon later, hippuric acid and benzil also have been found.[55] Benzil, the first organic NLO material, proved relatively easy to grow into large single crystals. Over the last two decades, NLO processes in organic and polymer materials were studied with a rapid and

sustained growth. The most important feature of organic molecules is a typical push-pull structure, *i.e.*, π-conjugated systems connecting an electron-donating group and an electron-withdrawing group. Various examples of donor or acceptor groups and of the conjugated backbone are shown in Figure 1.5. Organic NLO molecules often possess donor-acceptor groups attached to an aromatic ring system that increases charge transfer through p-electron delocalization.

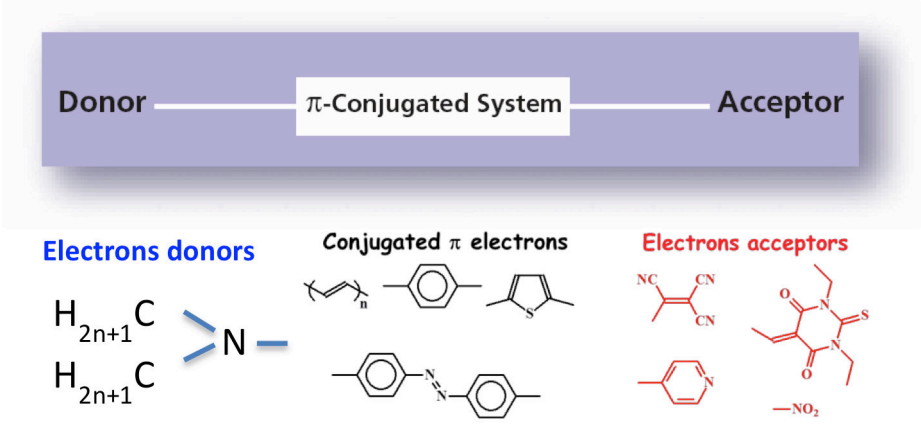

Figure 1.5 *Examples of organic NLO molecules with donor-acceptor electron groups, push-pull chromophore* [56].

A large number of good quality organic NLO materials have been investigated such as l-(4-nitrophenyl)-2-(4-methoxyphenyl)-l-cyanoethene (CMONS),[57] urea,[58,59] p-nitroaniline (PNA),[60] 3-methyl-4-nitropyridine-1-oxide (POM),[61] 2,4,6-triamino-1,3,5- trinitrobenzene (TATB),[62] N-(4-nitrophenyl)-(L)-prolinol (NPP),[63] 4-dimethylamino-N-methyl-4-stilbazolium tosylate (DAST),[64] and so on. Further, organometallic complexes have been investigated and displayed high molecular hyperpolarizabilities. Metals coordinated with NLO chromophores result in molecules of much greater complexity than for the first generation of "push-pull" organic molecules and can give rise to tunable optical properties. In a greater design flexibility, the metal center may be an extremely strong electron donor or acceptor, e.g. by variation in metal oxidation state, ligand environment and geometry, a requirement for electron asymmetry and hence second-order nonlinearity.[65,66] Additionally, several polymers have interesting $\chi^{(2)}$ properties. Poly(vinylidene flouride), PVF2, and its copolymers with poly(trifluoroethylene), PVF3, show piezoelectric properties, and SHG emission. These NLO properties can be enhanced by poling the material under an electric field.[67] Similar effects are observed in alternating copolymers of vinyl acetate and vinylidene cyanide, co(PVCN-

PVAc).[68] The incorporation of highly nonlinear push-pull molecules to polymer matrices, preferably in the form of functionalized macromolecules where NLO units are chemically grafted to the polymeric chain, resulted in high-performance electro-optic polymers with EO coefficient above 100pW/V and a very wide bandwidth (hundreds of GHz).

1.3.4. Noble metal NLO nanomaterials

Since 1998, various nanomaterials with high second order NLO properties and interesting applications in photonics as well as chemical and biological detection have been researched and developed. The surface-enhanced phenomenon is predicted to have a particularly important impact in NLO applications, since the generally weak nonlinear effects can be significantly increased via strong electromagnetic fields at the surfaces of noble metal nanoparticles (NMNPs) (plasmonic resonance).[8–24]

Equation 1.4 clearly emphasizes that SHG increases nonlinearly with the fundamental electric field amplitude. The basic idea behind nonlinear plasmonics is to use the enhanced electric field associated with plasmon resonances to increase the strength of NLO effects. The first plasmon enhancement of SHG was reported in 1974 for surface plasmon polaritons propagating at the surface of a silver film.[69] The localized surface plasmon resonance (LSPR) enhancement of SHG from metallic nanoparticles has also been theoretically predicted and experimentally confirmed.[70,71] Due to the LSPR enhancement, SHG from plasmonic nanostructures is much higher than that from the best chromophores[72] and comparable, if not higher to that from nanoparticles made of nonlinear materials as $KNbO_3$, $LiNbO_3$, $BaTiO_3$, KTP, and ZnO[73]. In plasmonic structures with nanometer sizes, an enhancement of the second harmonic intensity is clearly observed when the wavelength of the incident light matches the resonant wavelength of a LSPR.[74–76] Currently, scientists are focused on studying the development of NMNPs based second order NLO materials with different sizes and shapes.

Part B. Noble metal nanoparticles (NMNPs): introduction, properties and applications

1.4. Introduction

The word "nano" is a Greek prefix meaning dwarf or something very small and depicts one billionth of a unit. Nanotechnology is the science that deals with matter at the scale of 1 billionth of a meter (*i.e.*, 1 nm = 10^{-9} m), and is also the study of manipulating matter at the atomic and molecular scales. A nanoparticle is the most fundamental component in the fabrication of a nanostructure, and is far smaller than everyday objects that are described by Newton's laws of motion, but bigger than an atom or a simple molecule that are governed by quantum mechanics.

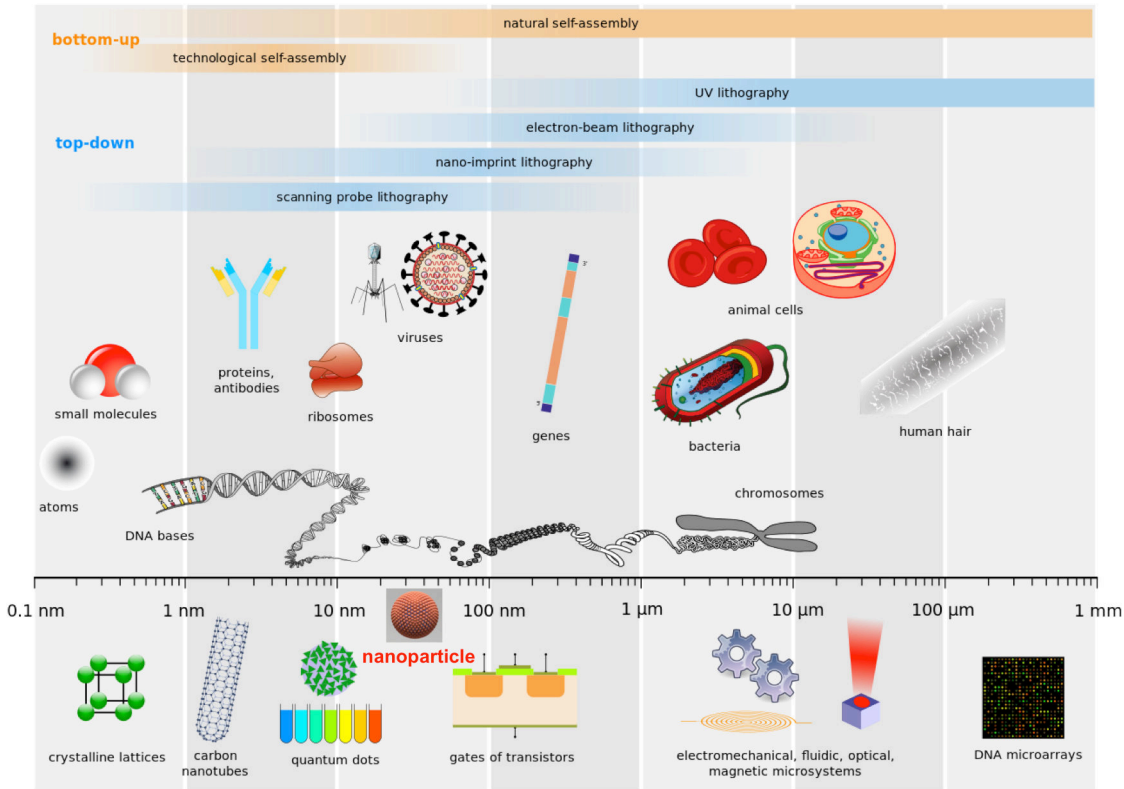

Figure 1.6 *Sizes of nanoparticles in comparison of the scales of various biological and technological objects.*

In general, the term "metallic nanoparticle" is used to describe nanosized metals with dimensions (length, width or thickness) within a size range between 1 and 100 nm (see Figure 1.6).[77,78] NMNPs made of gold, silver and platinum belong to the most extensively studied

colloidal systems in the field of nanoscience and nanotechnology because of their unique properties. Nanoparticles of noble metals display physical, chemical, and attractive linear and nonlinear properties that strongly differ from those of bulk metals (e.g., lower melting points, higher specific surface areas, specific optical properties, mechanical strengths, *etc*.), making them potentially attractive in various applications.[78] The optical properties of NMNPs are tunable throughout the visible and near-infrared region of the spectrum as a function of nanoparticle size, shape, surface state, and local environment.

The physicochemical properties of NMNPs can be tuned by a proper control of their size and shape and by carefully selecting appropriate surface functionalities. The implementation of proper synthetic methods is thus crucial in optimizing the size and shape of nanoparticles and thereby in tuning their properties for given specific applications.[79] Nonspherical plasmon resonant nanoparticles offer favorable properties for their use as analytical tools, or for diagnosis and as therapeutic agents. Anisotropic features in nonspherical nanoparticles have shown to improve their performances for various applications such as photonics, information storage, electronic and optical detection systems, sensing, imaging, electronics, energy harvesting, catalysis and biomolecular manipulation.[80–94]

1.5. Historical background

The first use of metallic nanoparticles emerged several centuries before the development of modern science. Perhaps the oldest object is the Lycurgus chalice from fourth-century Rome, which contains gold nanoparticles (AuNPs) and is exhibited at the British Museum in London (see Figure 1.7 (a)). Nanotechnology is easily evident in various old churches. A well-known application of early nanotechnology is the ruby red color that was used for stained glass windows during the Middle Ages. Beautiful examples of these applications can be found in glass windows of many Gothic European cathedrals. Among them, the stained glass of a wonderful rose can be seen at the world heritage Cathédrale Notre-Dame de Chartres in France, where the size and shape of silver and gold nanoparticles are responsible for the colors of the glass. The stained glass made in medieval times is displayed in Figure 1.7 (b) and (c).[77,95,96] These effects are caused by one of the most important types of interaction of metal nanoparticles with the electromagnetic field, LSPR, which will be discussed in this chapter.

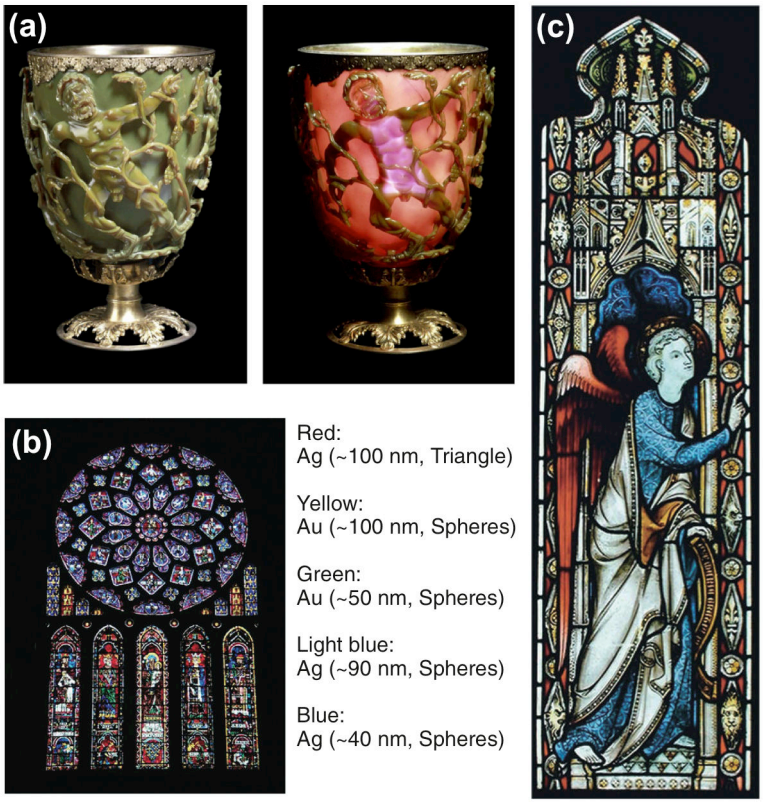

Figure 1.7 *(a) The Lycurgus cup, from the British Museum, displays a different color depending on being illuminated from outside (left) and illuminated from inside (right). (b) Rosace stained glass in the Cathédrale Notre-Dame de Chartres (France).*[97] *(c) Stained glass museum, Great Britain.*[96]

Systematic chemical synthesis of colloidal nanoparticles was pioneered by Michael Faraday in 1857[98] (the word *colloid* itself did not exist at the time of Faraday's work). This is considered to be a major step in the development of nanotechnology. To date, Faraday original samples are still preserved and are on display at the Faraday Museum in London (see Figure 1.8). In 1861, Graham coined the word *colloid* from the French word *colle.*[99,100] Mie's 1908 paper[101] represents the first theoretical treatment of the optical properties of spherical metal particles. Mie scattering theory is applied today to a variety of systems, including nonmetal particles. Following Faraday, a large number of experimental methods have been reported for the synthesis of AuNPs.

Figure 1.8 *(a) Michael Faraday. (b) Faraday's gold preserved at the Royal Institution of Great Britain.*[100]

Similar to gold, silver has also been used for thousands of years in various fields. Long before the introduction of antibiotics, colloidal silver had been known and used as a bactericide for at least 1200 years.[102] In 1889, Lea,[103] then Frens and Overbeek,[104] accomplished a major landmark in chemistry by preparing a silver colloid for the first time through reduction of silver nitrate using ferrous sulfate and ensured a consequent protection of colloidal particles by citrate ions. A huge interest in colloidal silver followed this first controlled synthesis, and a large number of researchers worked on the antibacterial properties of silver in the early twentieth century.[100]

Besides the other precious metals, over the past decade, research into the design of platinum nanoparticles (PtNPs) with unique properties has been greatly intensified due to the potential for new applications and improving current applications such as fuel cells, sensors, and the petroleum and automotive industries due to their high catalytic activity and stability.[105–122] Since platinum is a precious metal, most of the recent efforts have focused on decreasing platinum utilization via increasing the catalytic efficiency of Pt-based catalysts by tailoring high-performance Pt-based nanostructured materials, revealing that the shape of PtNPs plays a critical role in catalysis.[122–127]

Since the 1970s, the innovative development of NMNPs is due to theoretical as well as experimental developments in the fields of physics, chemistry, materials science, and biosciences. Specific phenomena (chemical and physical properties), not limited to the optical properties of NMNPs, have led to new possibilities in various fields.

1.6. Optical properties

1.6.1. Localized surface plasmon resonance (LSPR)

The resonant oscillation of conduction electrons at the interface between two materials with a negative and a positive permittivity respectively is stimulated under an incident electromagnetic wave, a phenomenon known as surface plasmon resonance (SPR). The electrons on the surface are the most significant ones, since the electromagnetic wave can penetrate within a very limited (< 100 nm) depth in a metallic structure, such as metallic films.

In the case of metallic nanoparticles, the collective oscillations of free electrons are confined to a finite volume defined by the particle dimensions. When surface plasmons are confined to a nanostructure that is much smaller than the wavelength of light, they are localized and do not propagate, and they show a specific resonance frequency known as LSPR. Figure 1.9 depicts the difference between SPR and LSPR.

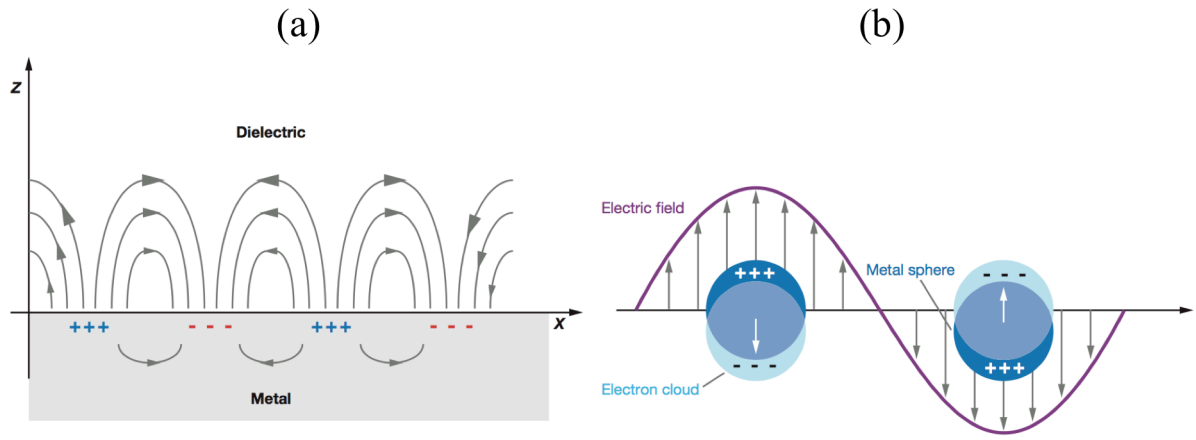

Figure 1.9 *Schematic diagrams for (a) SPR in a metallic film (macroscopic scale) and (b) LSPR in metallic nanoparticle (case of nanoparticles with diameter << λ).*[128]

When the free electrons in a metallic nanostructure are driven by the incident electric field to collectively oscillate at a certain resonant frequency, the incident light is absorbed by the nanoparticles. Some of these photons will be scattered, *i.e.*, released in all directions with the same frequency, while some others will turn into vibrations of the lattice, which is known as absorption. This is responsible for the very specific colors of NMNPs.[129]

The frequency and width of the surface plasmon absorption depend on the size and shape of the nanoparticle as well as on the dielectric constant of the metal and on the surrounding environment. For NMNPs made of gold, silver, and copper, the plasmon resonance is strongest and appears in the visible part of the electromagnetic spectrum, which make them important in many fields. On the contrary, for PtNPs, the LSPR frequency lies in the UV region of the spectrum, and does not display well-defined LSPR bands that are tunable like those of the other noble metals.[79] The size and shape dependence of the plasmon absorption of NMNPs in aqueous solution has been investigated by different groups.[130–133] Figure 1.10 shows the extinction spectra of NMNPs of different shape and size.

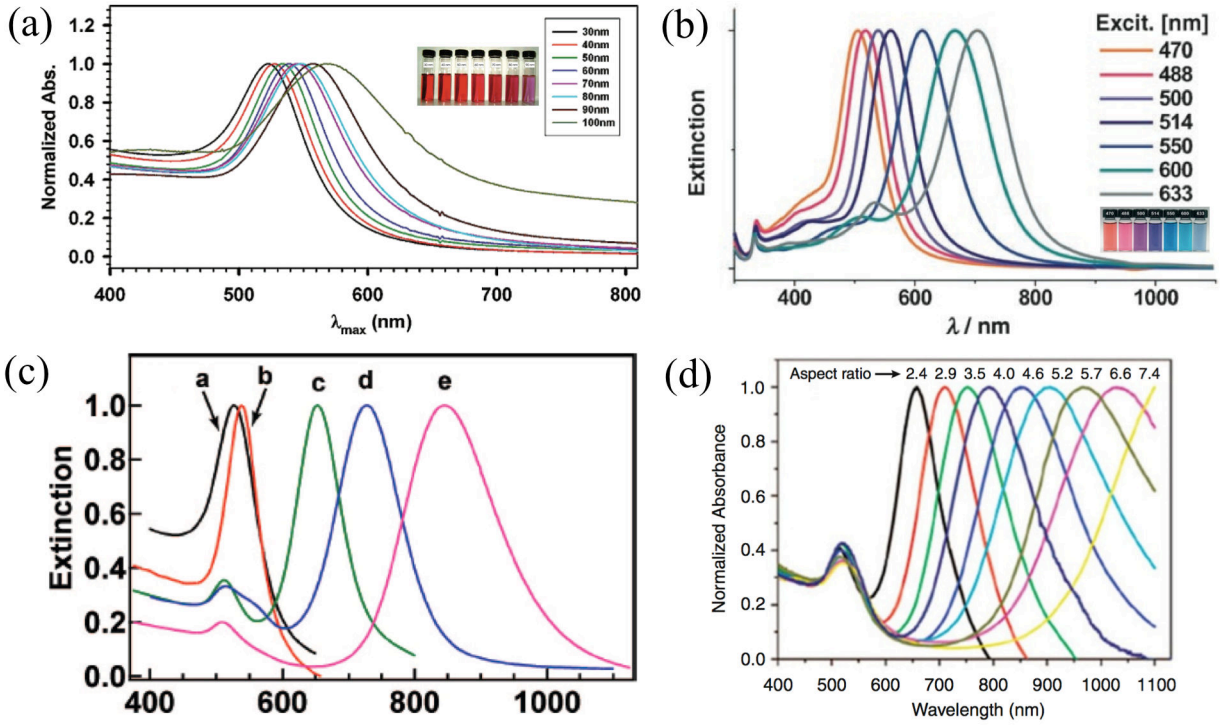

Figure 1.10 *(a) UV-Vis spectra (normalized) for AuNPs with different particle sizes in aqueous solution.*[130] *(b) Extinction spectra and corresponding solutions of silver nanoprisms with varying edge length.*[131] *(c) Normalized extinction spectra a-e of AuNPs correspond to nanospheres*[(a)]*, nanocubes*[(b)]*, and nanorods with aspect ratios of 2.4*[(c)]*, 3.4*[(d)]*, and 4.6*[(e)] *respectively.*[132] *(d) Extinction spectra of experimentally fabricated gold nanorods with different aspect ratios.*[133]

The red shifted absorption peaks from 500 to 550 nm corresponds to an increase in particle size of spherical AuNPs, giving red colored solution with particles smaller than 90 nm and purple or blue color for bigger particles (Figure 1.10 (a)). This phenomenon is also observed when increasing the edge length of Ag nanoprisms and the aspect ratios (AR, *i.e.* length divided by width) of gold nanorods (AuNRs) (see Figure 1.10 (b) and (d)). Au nanospheres and nanocubes have one surface plasmon peak while Au nanoprisms show one surface plasmon peak and a weak shoulder. AuNRs exhibit two major surface plasmon peaks, one is associated with electron oscillation along the transverse direction, and the other one is associated with electron oscillation along the longitudinal direction (Figure 1.10 (c)). It has been known that the number, location, and intensity of LSPR peaks of NMNPs strongly depend on several factors, such as particle size, shape, aggregate morphology, ligand, medium dielectric property and refractive index of the surrounding medium.[134–142]

1.6.2. Size and shape dependent second-order nonlinear optical properties of NMNPs: state of the art

In the past decade, scientists have explored size- and shape-dependent nonlinear optical properties of NMNPs driven by the excitement of understanding a new science and by the expected applications in nano-scale photonic and photoelectronic devices. This is due to the large enhancements of electromagnetic fields through LSPR. The NLO properties of NMNPs are often evaluated through their hyperpolarizability values. Due to the lack of dipole moment, HLS is the relevant method for the measurement of the first hyperpolarizability tensor β of nanoparticles dispersed in a liquid solution.[9–24]

Hyperpolarizabilities of NMNPs are expected to display large magnitudes because of the possibility of resonance enhancements through surface plasmon excitations.[13,15,23] Au and Ag nanoparticles have been investigated principally since copper particles are not stable in aqueous solutions. Copper particles require a careful passivation to prevent oxidation of the metal. The value of the hyperpolarizability for aqueous suspensions of gold and silver nanospheres (AuNSs and AgNSs) has been reported with diameter ranges from 10 to 150 nm and from 20 to 80 nm respectively.[15]

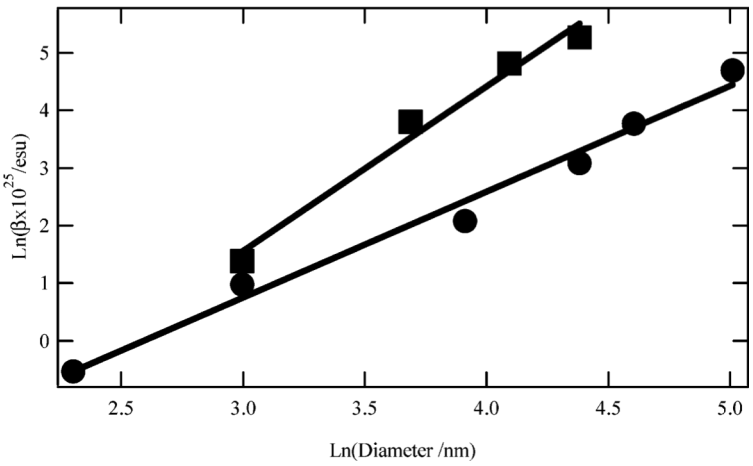

Figure 1.11 *Log-log plot of the hyperpolarizability magnitude against particle diameter for silver (squares) and gold (disks) spherical particles at the harmonic wavelengths of 390 and 400 nm, respectively.*[15]

The results in Figure 1.11 clearly show that the absolute magnitude of the first hyperpolarizability tensor obtained for AuNSs at the fundamental wavelength of 800 nm is smaller than that of AgNSs using 780 nm incident light. In this experiment, the LSPR enhancement for the AgNSs is indeed rather strong, owing to the harmonic wavelength involved in these experiments, in close vicinity to the LSPR wavelength. Additionally, β values obtained for AuNSs by Galletto *et al.*[13] at the nearly resonant second harmonic wavelength of 532 nm are higher than those obtained at 400 nm[15].

To understand how β value changes with diameter of the AuNPs, Griffin *et al.*[143] measured the β values of AuNPs of different diameters (Figure 1.12). The results indicate that the β value increases by two orders of magnitude on moving from 5 to 110 nm AuNPs. Since λ_{max} values for AuNPs (510–620 nm) are very far from the excitation source (860 nm) or second harmonic generated frequency (430 nm), the two-photon induced luminescence contributions in HRS experiment can be neglected.

It must be pointed-out that β values as reported in ref.[143] and Figure 1.12 cannot be compared to results obtained in our works, as β value of the reference solvent (water) has

been wrongly taken equal to 0.56×10^{-30} esu instead of the correct one ($\beta_{H_2O} = 0.055 \times 10^{-30} esu$ taken in our work, see part 2.6 of the Chapter 2).

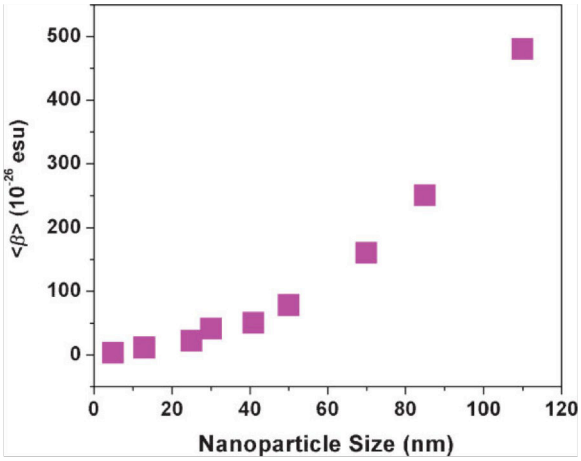

Figure 1.12 *Variation of β with particle size in water solvent.*[143]

The influence of AR on the optical second harmonic response of AuNRs was explored in ref.[9] and are displayed in Figure 1.13. It is observed that β per particle increases with the aspect ratio of nanorods having the same surface area. Brevet *et al.*[14] also reported that the HLS intensity collected from a solution of a mixture of AuNRs and AuNSs in water solution confirms that the HLS signal mainly arises from the AuNRs.

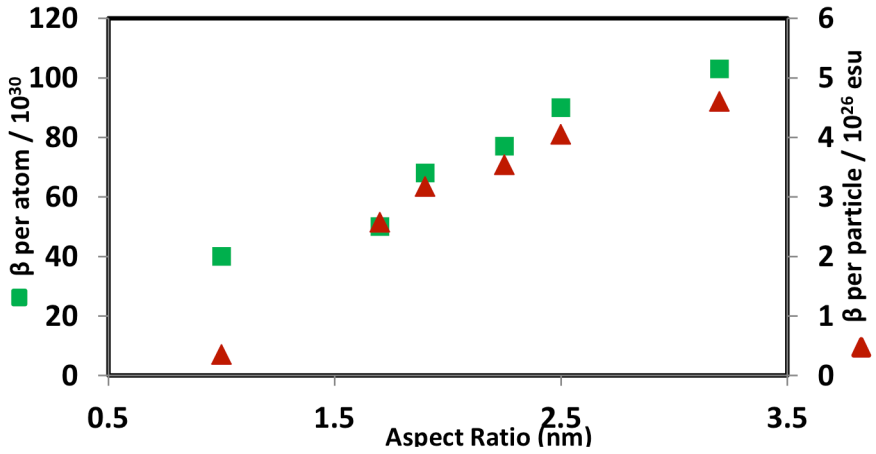

Figure 1.13 *Absolute value of the first hyperpolarizability β calculated per Au atom and per Au particle in water solution versus the AR of AuNRs.*[9]

Further, the first hyperpolarizability values of five different shape AuNPs including nanospheres, nanotetrapods, nanostars, nanorods and nanoflowers were compared using their HLS properties.[12] The first hyperpolarizability values depend significantly on their symmetry as well as the presence of sharp tips on the gold nanoparticle surface. Star- and flower-shaped AuNPs, which are non-centrosymmetric, show maximum β values while AuNPs having centrosymmetric shapes like spherical (or nearly spherical), rod and tetrapod shape display lower β values (see Figure 1.14).

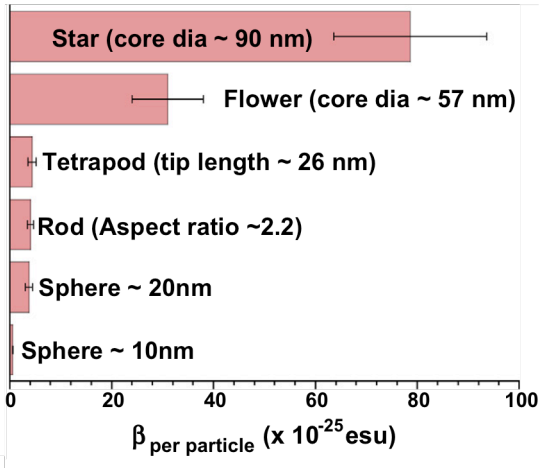

Figure 1.14 *First hyperpolarizability β values of five different shaped AuNPs.*[12]

It is generally believed that the presence of sharp tips/edges in metallic nanoparticles generates intense electric fields in their vicinity, which is expected to increase their β value. When β values are normalized with respect to the number of atoms per particle, tetrapod, flower and star-shaped AuNPs yield similar hyperpolarizability values. However, it is important to note that an accurate estimation of their number densities are not possible as some of these AuNPs do not show a regular geometrical shape. This study shows how the presence of pointed structures or tips can significantly affect the beta values and makes them better candidates for sensing applications based on nonlinear optical properties of these AuNPs.

The question of the origin of the first hyperpolarizability from small metallic particles has been raised in the past with, to date, no definitive experimental answer. It has been

demonstrated that the frequency conversion process finds its origin at the surface of the particles when the shape of the particles is not perfectly spherical. As a consequence, the total HRS response is of electric dipole nature for small particles; however, for larger particles, retardation effects in the electromagnetic fields must be considered, and a non-negligible quadrupolar contribution is observed. In order to verify this hypothesis via HLS, the fundamental input beam is linearly polarized, and its polarization angle is modified using a rotating half-wave plate. The fundamental beam propagates along the Z direction, its electric field being linearly polarized in the {X,Y} plane with a variable polarization angle, and the harmonic light is collected along the Y direction, at a 90° angle with respect to the fundamental beam propagation direction (see part C for more details).[16] The polar plot of the HRS intensity as a function of the polarization angle γ of the incoming fundamental wave for an aqueous suspension of NMNPs was reported by various groups.[15,16,143–145]

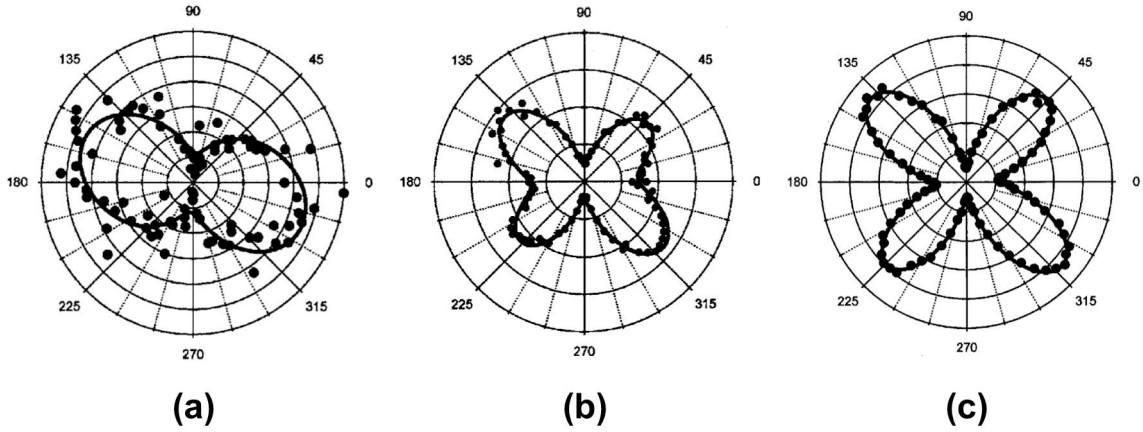

Figure 1.15 *Polar plot of the HRS intensity as a function of the incoming fundamental beam polarization angle: (filled circles) experimental points and (solid) fit to the experimental data points using theoretical modeling for an aqueous suspension of (a) 50 nm diameter, (b) 100 nm diameter, and (c) 150 nm diameter gold particles.*[144] *The fundamental wavelength was set at 800 nm and the HLS light collected at 400 nm.*

The experimental results (as shown in Figure 1.15) clearly show that, for the particles with a diameter smaller than 50 nm, the response is dominated by the dipolar contribution arising from the deviation of the particle shape from that of a perfect sphere. For larger

diameter particles, retardation effects in the interaction of the electromagnetic fields with the particles cannot be neglected any longer and the response deviates from the pure dipolar response, exhibiting a strong quadrupolar contribution. The experimental plot for a 50 nm diameter nanoparticle shows two lobes, which are similar to the one for a pure electric dipole response from noncentrosymmetric organic molecules, as reported by several groups.

Because of the centrosymmetry rule, the design of nanostructures with non-centrosymmetric shapes has become essential. Nowadays, both top-down and bottom-up approaches have been optimized for the fabrication of nanoparticles with excellent reproducibility. The SHG response from lithographed nanoparticles with various geometries has been investigated including holes in metallic films,[146–148] split-ring resonators with U-shape,[149–151] chiral G-shaped nanoparticles,[152–154] chiral gold nanoprisms,[155] L-shaped nanoparticles,[156–158] *etc*.

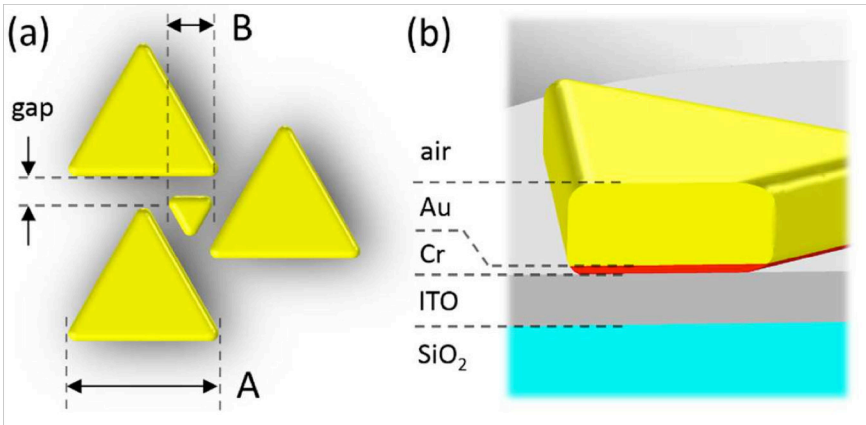

Figure 1.16 *Geometry of acentric and chiral gold nanostructures: (a) three parameters defining the lateral geometry, presented on the example of the left-enantiomer: A ≈ 200 nm – side length of the gold nanoprisms, B ≈ 60 nm – side length of the smaller central gold nanoprism (referred to as "central nanoparticle"), the gap between nanoprisms is around 40 nm; (b) cross-section of the sample, showing its layered structure: SiO_2 substrate (blue), ITO layer (25 nm, gray), chromium adhesion layer (3 nm, red) and gold nanostructure (40 nm, yellow), surrounded by air.*[155]

Particularly, 2D chiral arrangements of gold nanostructures were fabricated by means of EBL. Chiral nanostructures are composed of four gold nanoparticles: three gold nanoprisms

arranged into a “pinwheel” and a smaller gold nanoparticle in the center. The structure and composition of these samples are presented in the Figure 1.16 (a) and (b), respectively.

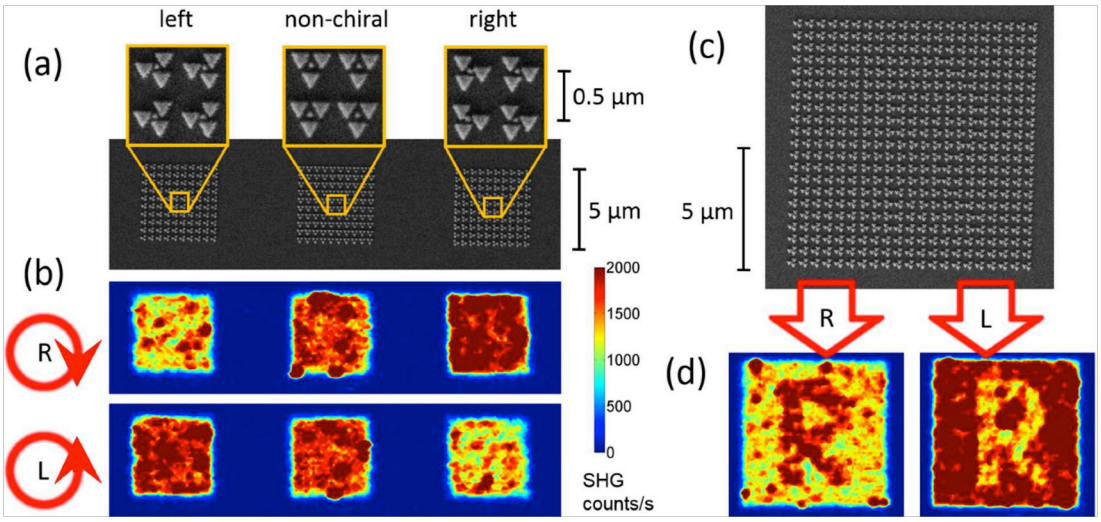

Figure 1.17 *(a) SEM image of three arrays, composed of: left-enantiomers (on the left), non-chiral reference nanostructures (in the middle), and right-enantiomers (on the right); (b) SHG scanning microscopy images of the three arrays, obtained under excitation at fundamental wavelength 850 nm with R (top) and L (bottom) circular polarization; (c) SEM image of the “watermark” formed by a mixture of right- and left- enantiomers; (d) SHG images of the “watermark” obtained with R and L polarization (as indicated). The SHG intensity scale in between (b) and (d) is common for all SHG images presented in the following figure.*[155]

In Figure 1.17, strong chiroptical effects in the backscattered SHG from 2D chiral arrangements of gold nanoprisms have been evidenced using nonlinear microscopy and confirmed by numerical simulations. The triangular motif of the investigated nanostructures, provide efficient dipole-allowed SHG due to lack of inversion symmetry, as well as sharp corners are prone to large local field enhancements. Because the investigated nanostructures are built from non-chiral elements (triangular nanoprisms), the observed chiroptical effects can be attributed to the plasmonic near-field coupling between the nanotriangles. These results open the perspectives of a new class of superchiral metamaterials, composed of interacting nanoparticles making chiral nonlinear “meta-molecules”, where chirality

originates from the mutual arrangement and inter-particle plasmonic interactions and not from the shape of individual nanoparticles.

1.7. Applications of NMNPs

Due to their unique physical and chemical properties, NMNPs have been used for various applications as presented below (see Figure 1.18). Extensive studies on AuNPs during the last few decades, exploited their different fascinating properties such as electronic, optical and catalytic properties together with their high degree of biocompatibility, rich surface functionalization chemistry, and high photostability. Therefore, these particles have been shown to be very attractive and useful material for applications in the fields of photonics, information storage, electronic and optical detection systems, sensing, imaging, diagnostics, therapeutics, electronics, energy harvesting, catalysis and biomolecular manipulation.[80–94] Further, for several (in vivo) applications, nonspherical AuNPs are also advantageous because their LSPR can be tuned to the near-infrared wavelength range, the so-called biological window, where absorption, scattering, and fluorescence from endogenous biological chromophores are minimal.[82,159]

Figure 1.18 *Applications of NMNPs.*

Particularly, in biomedical and environmental fields, AgNPs are mostly used in the medical field due to their antimicrobial effect, and AuNPs are used in cosmetics. In addition to their antimicrobial activities, AgNPs have also been proven to be more effective in designing sensors. For example, biogenic AgNPs were successfully used in the fabrication of an optical fiber-based sensor for the detection of H_2O_2 that is cost effective and portable and can be used in various industrial applications.[160] Furthermore, based on the higher efficiency and biocompatible nature of biological metal nanoparticles, it has been assured that biological nanoparticles may improve the action of typical anticancer drugs by facilitating drug delivery to specific cells, which reduces the required drug doses and avoids their side effects. The second application area of biological nanoparticles is also used in gene delivery and cell labeling in plants and in medicine (see Figure 1.19).[161]

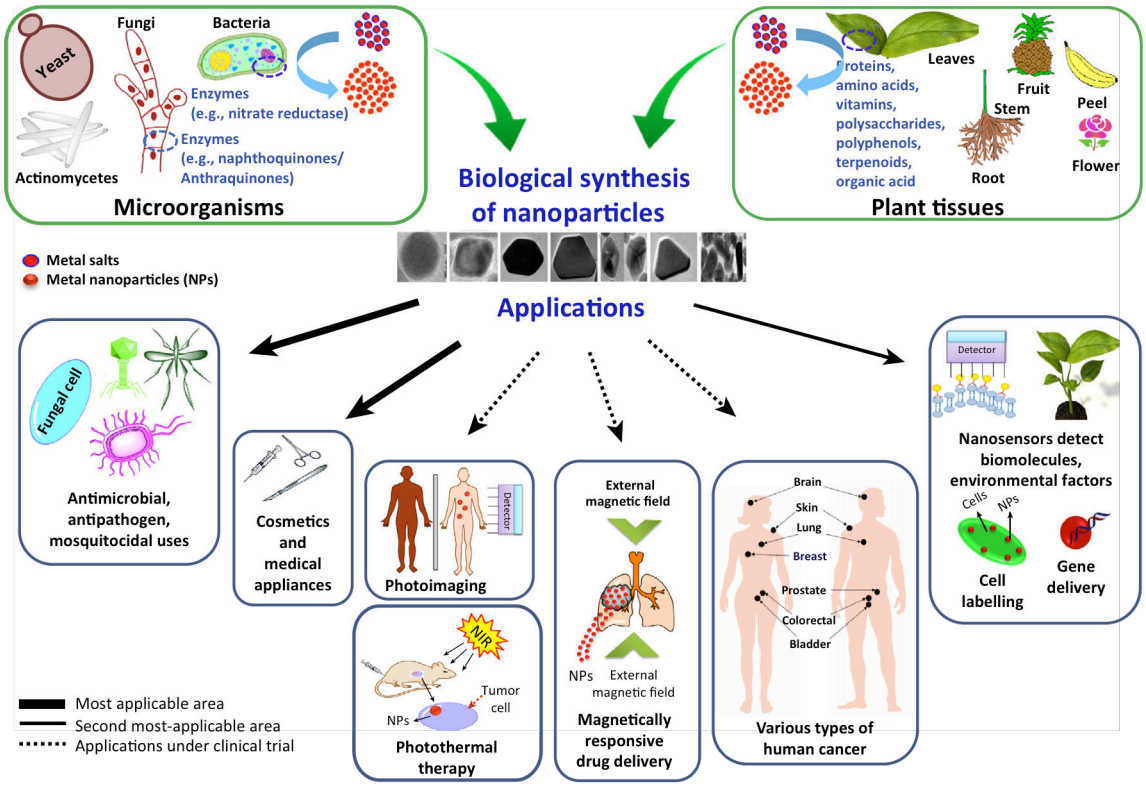

Figure 1.19 *Biological synthesis and applications of NMNPs in biomedical and environmental fields.*[161]

AuNPs possess distinct physical and chemical attributes that make them excellent scaffolds for the fabrication of novel chemical and biological sensors (see Figure 1.20).[91–94,162–167]

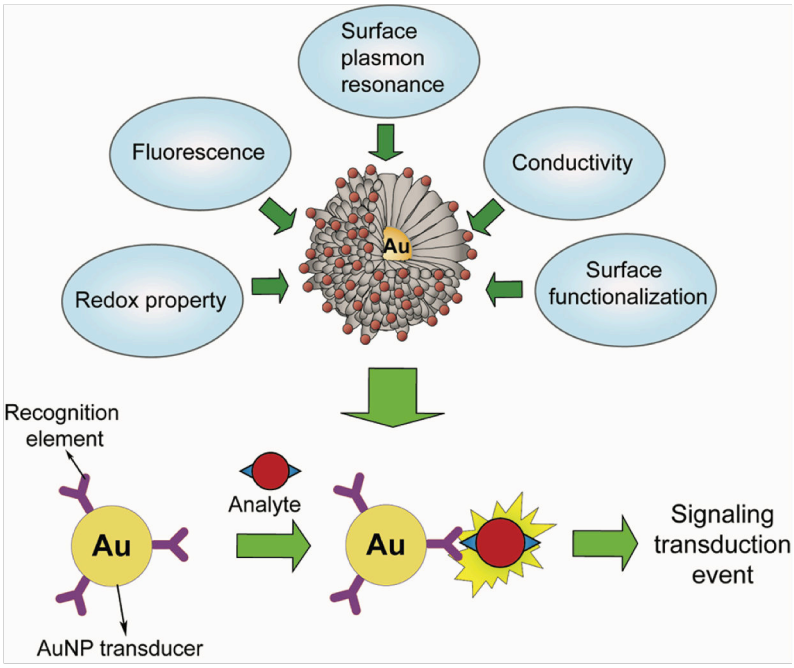

Figure 1.20 *Physical properties of AuNPs and schematic illustration of a AuNP-based detection system.*[91]

A typical sensor must satisfy the two following requirements: (i) it should have a ligand that selectively attaches the analyte and (ii) it should show a measurable change of some property during the recognition event. By exploiting different sensing strategies, AuNPs have been used as sensors including colorimetric sensors, fluorescence sensors and electrochemical sensors for the detection and measurements of a variety of analytes such as metal ions, anions, and molecules like toxins, saccharides, proteins, nucleotides and bacteria (see Figure 1.21).[79]

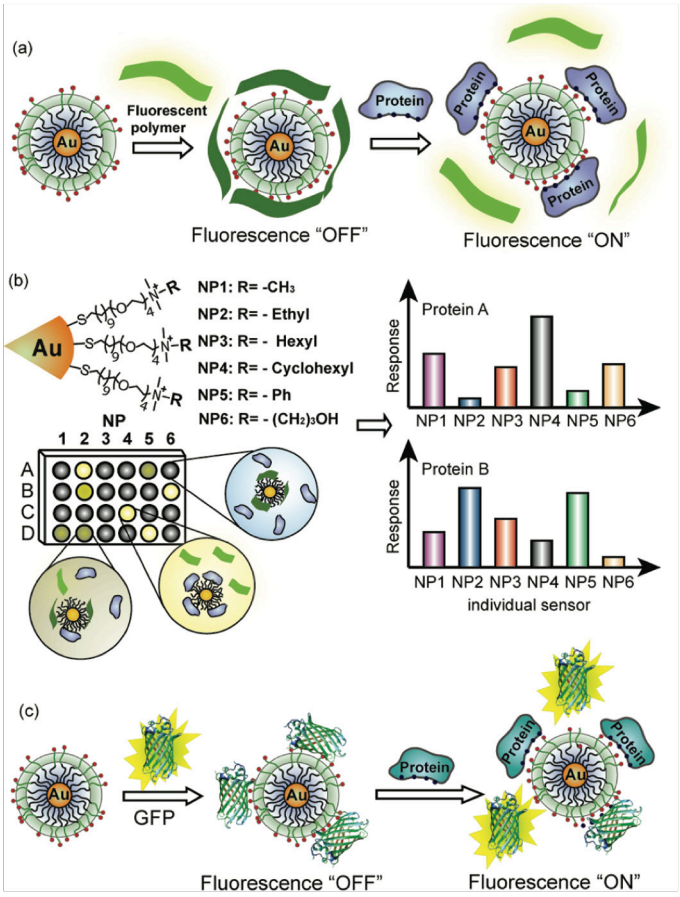

Figure 1.21 *Schematic illustration of a "chemical nose" sensor array based on AuNP-fluorescent polymer/Green Fluorescent Protein conjugates. (a) The competitive binding between protein and quenched polymer-AuNP complexes leads to the restoration of fluorescence (b) The combination of an array of sensors generates fingerprint response patterns for individual proteins. (c) The competitive binding between protein and nanoparticle−Green Fluorescent Protein complexes leads to fluorescence light up.*[91,168]

Carbon monoxide (CO) is a highly toxic gas that causes potential harm to the environment and human health; therefore, it is of great interest to limit its emission from vehicles and other industries. Platinum and most other noble metals are good catalysts for CO oxidation.[169–172] Gold was widely believed to be an exception until the striking discovery by Haruta *et al.*[173] showing that supported AuNPs smaller than 5 nm are more active than other noble-metal catalysts for low-temperature CO oxidation. The best activity was found when reducible

oxides (TiO_2, CeO_2, Fe_2O_3) were used as substrates; this naturally led to the hypothesis that lattice oxide ions were somehow involved, or that anion vacancies caused by surface reduction of the substrates by CO provided possible sites for the adsorption of O_2 molecules adjacent to the gold particles (see Figure 1.22).[174–176] It now appears that ceramic oxide substrates (Al_2O_3, SiO_2, MgO) can also be effective if the gold particles are small enough.

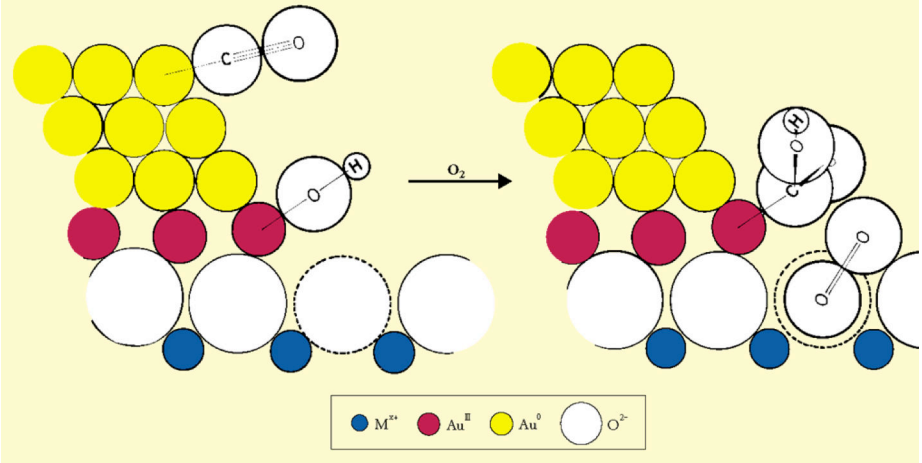

Figure 1.22 *Mechanism of oxidation of CO over AuNPs deposited on a reducible oxide.*[176]

Additionally, there are many applications of NMNPs based on their SHG properties. The relationship between the specific properties of SHG from plasmonic nanostructures and some advanced applications has been outlined in Figure 1.23.[76,177–183]

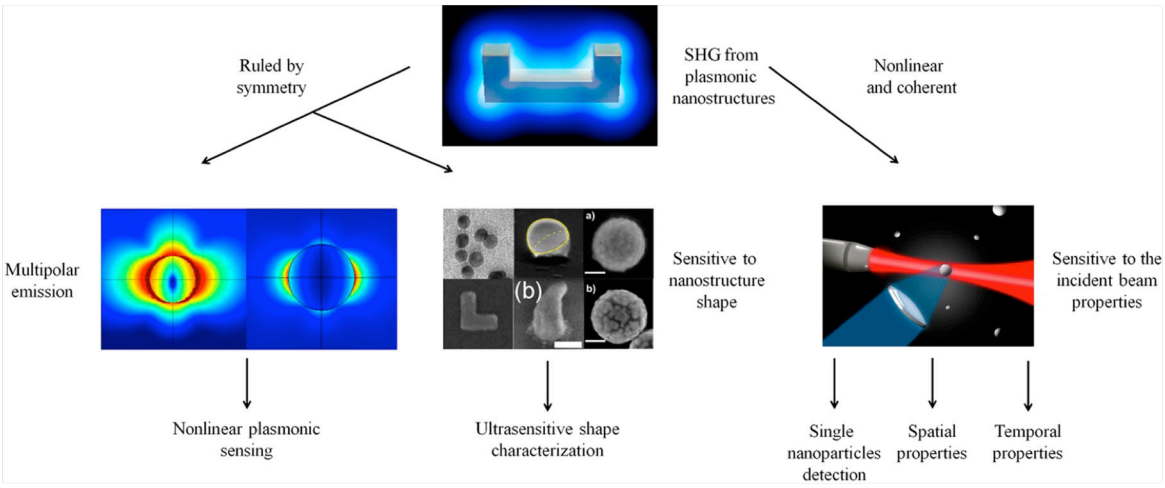

Figure 1.23 *Outline of a review with the different links between fundamental principles of SHG in plasmonic nanostructures and practical applications.*[76]

Looking further to future potential applications, one can expect that NMNPs of controlled morphologies will find applications as in vivo force sensors, smart catalysts (for fuel cells, waste treatment, bioprocessing, *etc.*), enhancers in photovoltaics and other energy conversion devices, performance therapeutic and imaging agents, probes for single-molecule sensing of drugs, toxins, and environmental pollutants, and key components in energy transport and novel optoelectronic devices.[82]

Chapter 2

Experimental methods and instrumentation

2.1. Fabrication methods

In the synthesis of noble metal nanoparticles (NMNPs), controlling their shape and size is currently one of the most important and challenging tasks. Anisotropic NMNPs show interesting light absorption and scattering phenomena, resulting from extraordinary shape-dependent collective electronic resonances. Therefore, during the past two decades, the exploration of anisotropic NMNPs and of their properties has been applied successfully in a variety of fields such as therapeutics, detection and diagnostics, biolabeling, drug delivery, chemical and biological sensing, imaging, nonlinear optics, photovoltaics and catalysis, *etc*.[80–94] The fabrications of NMNPs are based on two basic nanoparticle preparation methods: top-down physical nanofabrication on one hand, bottom-up wet chemistry on another hand. A general schematic diagram of these two strategies is shown in Figure 2.1 below.

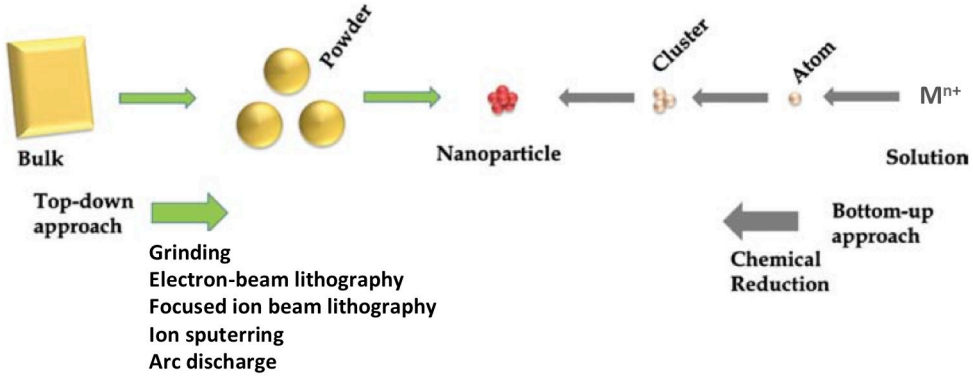

Figure 2.1 *Two basic nanoparticle preparation strategies methods: top-down and bottom-up.*[79]

A very basic top-down mechanical method to produce NMNPs is shattering and/or grinding bulk material. However, the sizes of resulting particles are usually relatively large and widely scattered, which leads to many difficulties either to control the size and shape of particles or to obtain a narrow particle size distribution. More advanced top-down approaches involve physical methods like electron-beam lithography (EBL),[184,185] focused ion beam (FIB) lithography,[186] ion sputtering,[187] arc discharge,[188] UV and IR radiation,[189,190] aerosol technology,[191] *etc*.

On the other hand, the bottom-up method uses wet chemical process to prepare metallic nanoparticles, including chemical reduction, electrochemical pathways and organometallic compound decomposition, *etc*. Among them, the chemical reduction method is simple and allows to prepare particles with various sizes and shapes with good yields and controllable polydispersity. Typically, the synthesis of metallic nanoparticles by chemical reduction involves two major parts: reduction of a precursor using suitable reducing agents, and stabilization of the obtained nanoparticles by suitable stabilizing or capping agents preventing aggregation of nanoparticles and their subsequent precipitation.

2.2. Top-down: “non solution” methods

Among the top-down physical lithography methods, electron-beam lithography (EBL) is the most widely used one. EBL is a technique used for the fabrication of micro- and nanostructures. This method is based on scanning a focused beam of electrons to draw custom shapes on an electron-sensitive film surface called a photoresist. The electron beam changes the solubility of the resist, enabling selective removal of the either exposed or non-exposed regions of the resist by washing it out with a developing agent. The primary advantage of electron-beam lithography is that it can draw custom patterns (direct-write) with sub-10 nm resolution. Then, noble metal can be deposited onto the opening patterns drawn by the electron beam. The remaining resist is then eliminated together with the metallic layer deposited on it, leaving only the metallic nanostructures that are in direct contact with the substrate. This lift-off technique can produce anisotropic nanoparticles with controllable positions, shapes and sizes in tens of nanometers length-scale.[184,192]

In Figure 2.2, e-beam was used to chemically modify the $-NO_2$ group of the surface nitrobenzene layers to $-NH_2$ group. Finally this modified surface was exposed to an acidic solution of colloidal gold nanoparticles (AuNPs), and the particles were selectively adhered to the NH_2 functionalized regions.

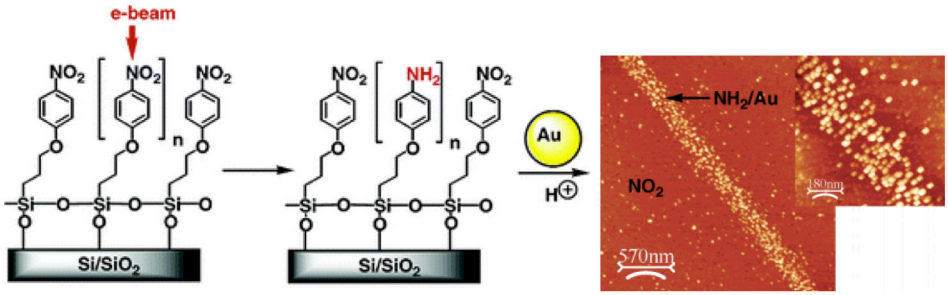

Figure 2.2 *Topography image of AuNPs assembled on to e-beam-irradiated 3-(4-nitrophenoxy)-propyltrimethoxysilane monolayer.*[185]

Similar to electrons, ions can also be used to lithographically pattern structures on suitable substrate surfaces. Direct ion writing methods, such as focused ion beam lithography (FIB), exist along with projection ion beam lithography. Ion lithography is considered as an alternative to electron beam lithography for two reasons: resist materials are far more sensitive to ions than to electrons and proximity effects due to scattering of the ions at the wafer/resist interface are reduced. As compared to optical lithography, where the resolution is diffraction-limited, and to e-beam lithography, where the resolution is limited by lateral scattering effects of electrons, the resolution limit for patterned structures using ion beams is estimated to be lower than 30 nm. The limit is determined by the lateral scattering of the ions in the resist material and the mean free path of the secondary electrons produced by the ions on their way through the resist layer. Figure 2.3 shows a schematic outline of a FIB.

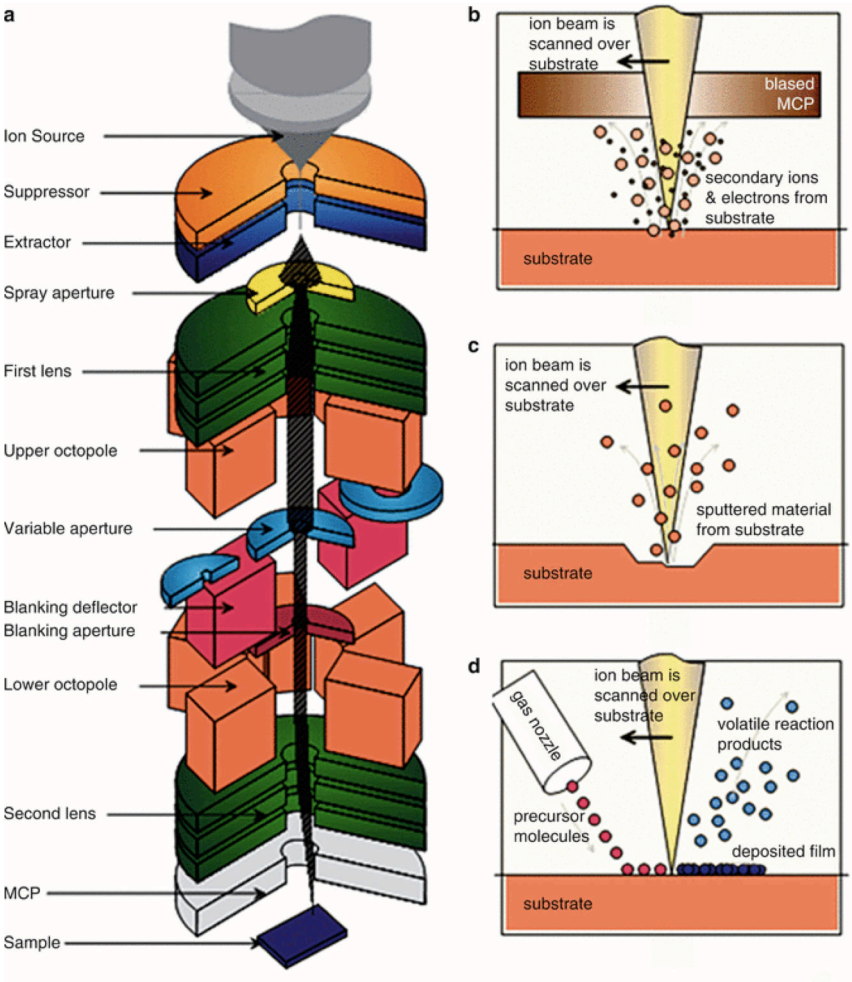

Figure 2.3 *(a) Schematic diagram of a (FIB) ion column, (b) work principle of FIB imaging, (c) FIB milling and (d) FIB induced deposition.*[193]

Although the top-down lithography techniques can produce nanoparticles with controllable size, shape, and position, their scaling down is limited and smaller nanoparticles with sizes less than 10 nm are not easily accessible. Further, the biggest problems with the top-down approach are the imperfections of the surface structure and the duration of the nanofabrication process. The surface of nanoparticles plays an important role in the properties of nanomaterials, especially optical properties.

2.3. Bottom-up: particle size and shape control

The chemical, electronic, and optical properties of NMNPs are extremely dependent upon their size and shape; therefore numerous approaches to synthetically and systematically control morphology and surface state of nanoparticles have been developed in recent decades.

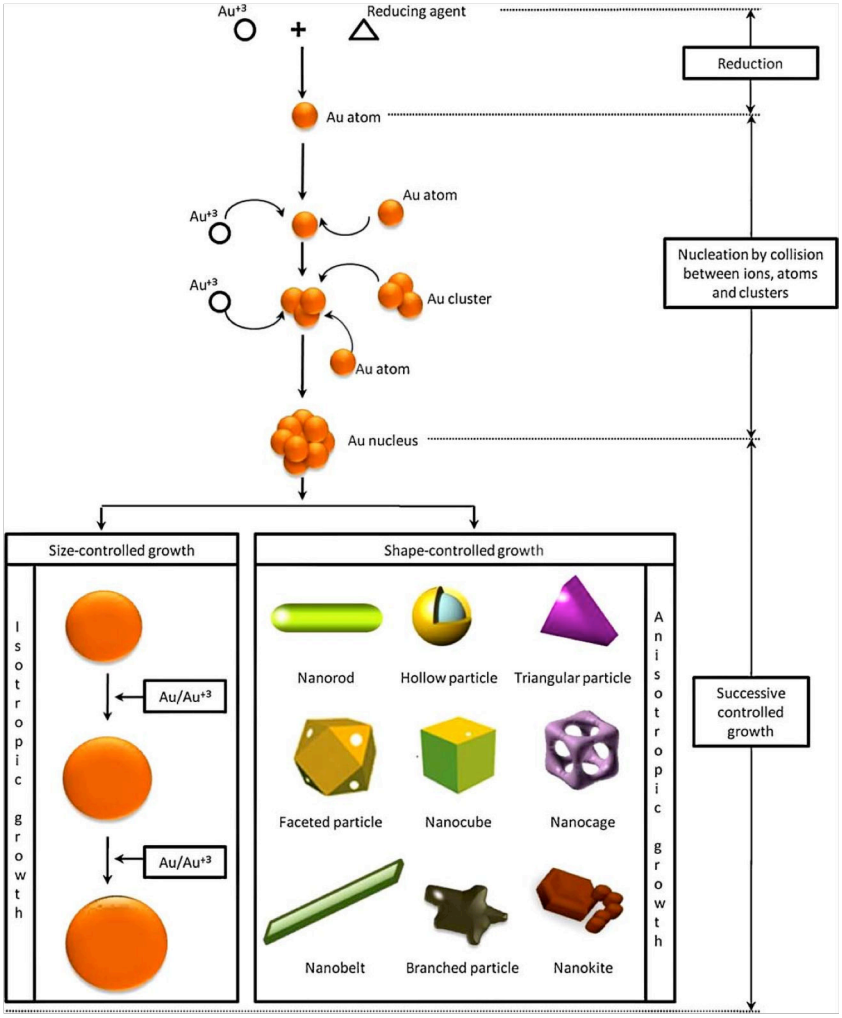

Figure 2.4 *Formation mechanism of AuNPs with various particle sizes and shapes by chemical reduction method.*[142]

Among them, the chemical reduction method is the simplest and most controllable. Figure 2.4 presents the general formation mechanism of AuNPs by the chemical reduction method in

solution. In the following descriptions, the synthetic strategies are called by the name of the first person to have proposed the method.

2.3.1. Turkevich method

For the synthesis of spherical AuNPs, the most popular method is based on the reduction of tetrachloroauric (III) acid ($HAuCl_4$) by trisodium citrate in water at 90-100 °C. This is the most commonly used process to synthesize gold nanospheres (AuNSs) due to its simplicity and environmental friendliness. Turkevich proposed this method in 1951,[194] which was improved later in 1973 by Frens.[195] In the experimental reduction process, sodium citrate solution was added quickly to a boiling point of aqueous solution of $HAuCl_4$ under vigorous stirring. The solution turned wine-red after few minutes, indicating particle formation with size around 20 nm. In this procedure, citrate ions act as both reducing and stabilizing agent (see Figure 2.5). By changing the relative amounts of Au precursor to reducing agent, we can control the particle size of AuNSs in a wide range between 10 and 150 nm.

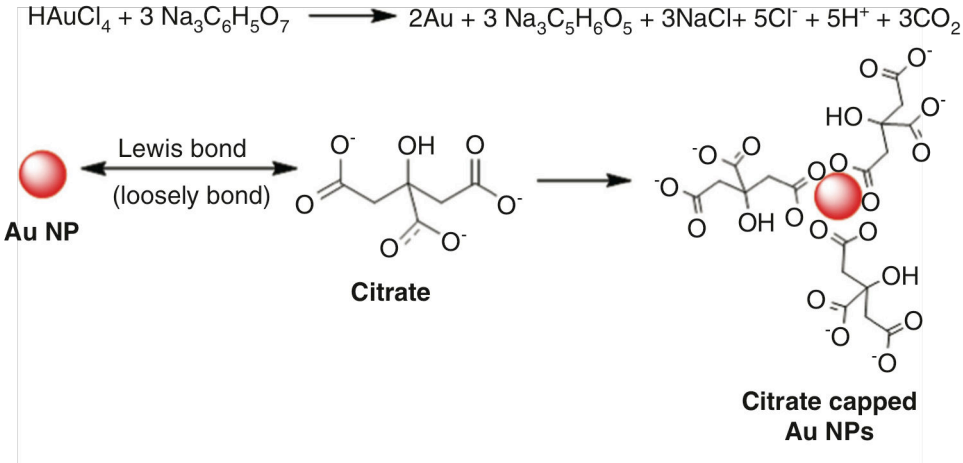

Figure 2.5 *Synthesis of AuNSs in aqueous solution by reducing $HAuCl_4$ with trisodium citrate.*[196]

In the preparation of AuNSs by citrate reduction, the particle size decreases as the relative concentration of citrate increases because of the stabilizing process of citrate. A high citrate concentration allows the fast and complete stabilization of small AuNPs, while, for lower citrate concentrations, the coverage of citrate is incomplete and the aggregation process results in the formation of larger particles. As many factors such as pH, concentration of reactants, stirring speeds and temperature influence the reaction process, the AuNSs obtained

by the Turkevich method usually show a broad distribution of size and shape. However, it is useful to remember that if uniformity in geometry is not a key-point for the final application, the Turkevich method is the easiest and fastest process to obtain water-soluble AuNSs in a large quantity.[79,142,197] In our work, we have used a modified Turkevich method by using, as reducing agent, $NaBH_4$ instead of citrate.[19]

2.3.2. Brust - Schiffrin method

The Brust−Schiffrin provides an easy and effective method at room temperature for the synthesis of highly stable functionalized AuNPs of small sizes.[198] Small particles were obtained by a two-phase reduction procedure based on a fast chemical reduction of gold ions by borohydride at ambient conditions at an oil–water interface, immediately followed by adsorption of thiolated molecules, which allowed handling of such particles as a simple chemical compound (see Figure 2.6).

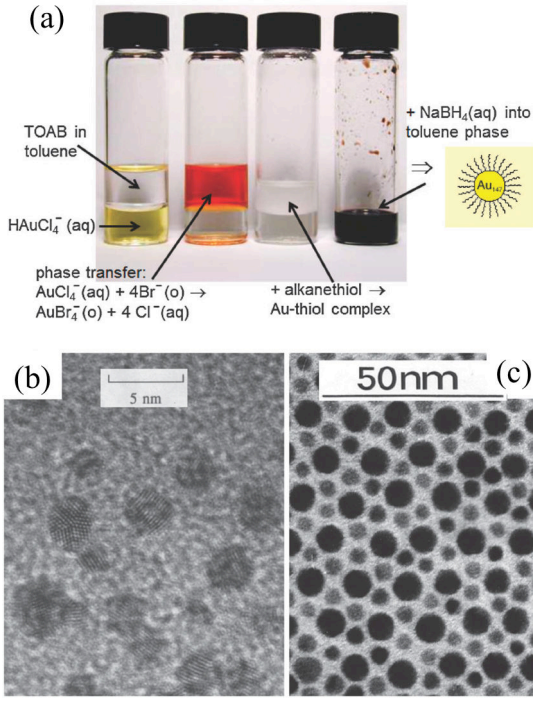

Figure 2.6 *(a) Schematic view of the Brust–Schiffrin method for the synthesis of monolayer-protected clusters. (b, c) TEM images of gold nanoparticles from the original Brust et al. Chem. Commun. paper*[199] *(b) and a two-dimensional binary crystal made by monodisperse gold and silver nanoparticles of appropriate sizes (c), also reported by Brust et al. Adapted with permission from ref.*[200].

An aqueous solution of $HAuCl_4$ was stirred with an organic solvent, toluene, and then the gold precursor is transferred to toluene using tetraoctylammonium bromide (TOAB) as the phase-transfer reagent. The Au^{3+} ions are reduced by $NaBH_4$ in the presence of dodecanethiol as a protecting ligand in organic phase. Upon addition of the reducing agent, the organic phase changes color from orange to deep brown within a few seconds. The particle size ranges between 1.5 and 5.2 nm. The chemical reaction involved can be represented as below, where de source of electron is BH_4^-.

$$AuCl_4^-(aq) + N(C_8H_{17})_4^+(toluene) \rightarrow N(C_8H_{17})_4^+ AuCl_4^-(toluene)$$

$$mAuCl_4^-(toluene) + nC_{12}H_{25}SH(toluene) + 3me^- \xrightarrow{BH_4^-} 4mCl^-(aq) + (Au_m)(C_{12}H_{25}SH)_n(toluene)$$

This two-phase reduction method has been preferred over many other alternatives because of its simplicity, and became the most widely used method for synthesizing nanoparticles of size less than 5 nm in organic solvents. Additionally, the method can be easily adapted to gram-scale production. The synthesis of other NMNPs such as that of Pt, Ag and Cu has been achieved successfully with different protecting ligands and reducing reagents by modifying the Brust–Schiffrin methods. We did not use this method in our PhD, as all NMNP solutions were prepared with water.

2.3.3. Seed-mediated growth method

Noble metal nanospheres is obtained by isotropic growth on the surface of metal nuclei, whereas anisotropic growth of particles will induce the formation of NMNPs of particular shapes. However, the shape of NMNPs is much more difficult to control. Among a large number of the chemistry methods, during the past two decades scientists have discovered and improved the seed-mediated growth method to prepare anisotropic NMNPs with high efficiency and excellent size distribution. This method is the most successful one in synthesizing anisotropic NMNPs with various nanostructures such as rods, wires, triangles, stars, flowers, and so on. Additionally, the seeding strategy has been usually used to synthesize large nanoparticles with excellent monodispersity.[19,20,130,132,201–203]

A typical seed-mediated growth process involves two steps: the synthesis of seed nanoparticles and their subsequent growth in growth solutions containing metal precursors, mild reducing reagents, and surfactant or shape-directing reagents. In the first step, to obtain the seed nanoparticles, the metal salt is reduced by reducing agents (e.g. commonly sodium

borohydride) in the presence of stabilizing agents. The seed does not need to be a metal nanoparticle in all cases. After the formation of seed nanoparticles, the second step of this process is their growth towards the desired shape and size. In this procedure, metal salts will get reduced on the surface of the seed nanoparticles. The activation energy for metal reduction onto preformed seeds is significantly lower than that for homogeneous nucleation of seed particles in solution; therefore, it only allows autocatalytic growth of metal atoms on the pre-existing seeds. The surfactant molecules will form suitable templates that facilitates the growth process to yield nanoparticles of desired morphology.[204,205]

Au and Pt nanospheres with controllable size and high monodispersity with 10-100 nm diameters have been synthesized in aqueous solutions by seeded growth.[19,130,201] The actual sizes of the resulting nanoparticles depend on seed sizes and on precursor concentrations. Figure 2.7 shows a typical set of TEM micrographs of AuNSs with different sizes.

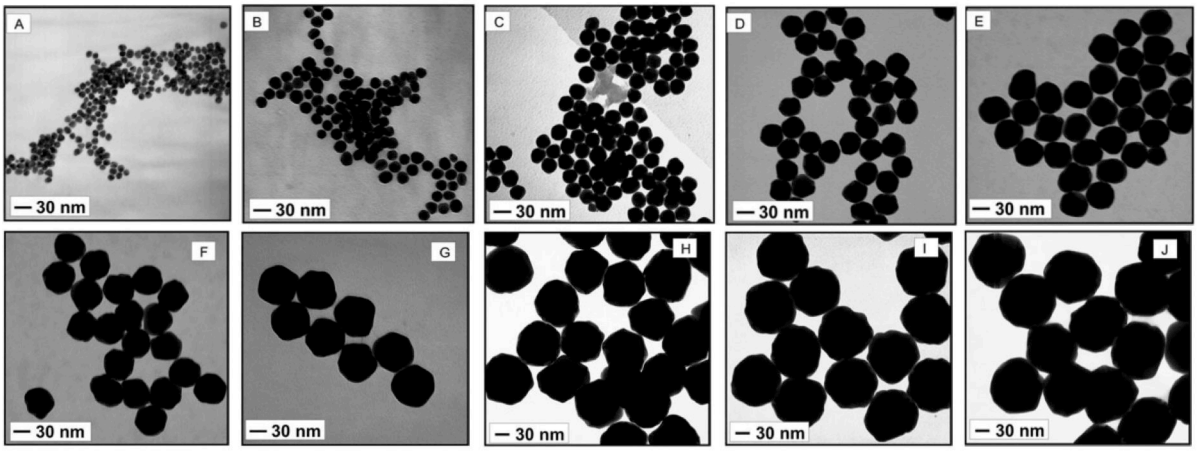

Figure 2.7 *TEM micrographs of AuNSs of different sizes: 10 nm (A); 20 nm (B); 30 nm (C); 40 nm (D); 50 nm (E); 60 nm (F); 70 nm (G); 80 nm (H); 90 nm (I); and 100 nm (J).*[130]

The simplest and most easily accessible anisotropic gold nanorods (AuNRs) have drawn great attention from scientists. The seed-mediated growth offers a convenient and versatile wet chemistry way to synthesize AuNRs with excellent yield, monodispersity, controllable aspect ratio (AR, *i.e.* length divided by width), size, and reproducibility. A typical procedure is shown in Figure 2.8.

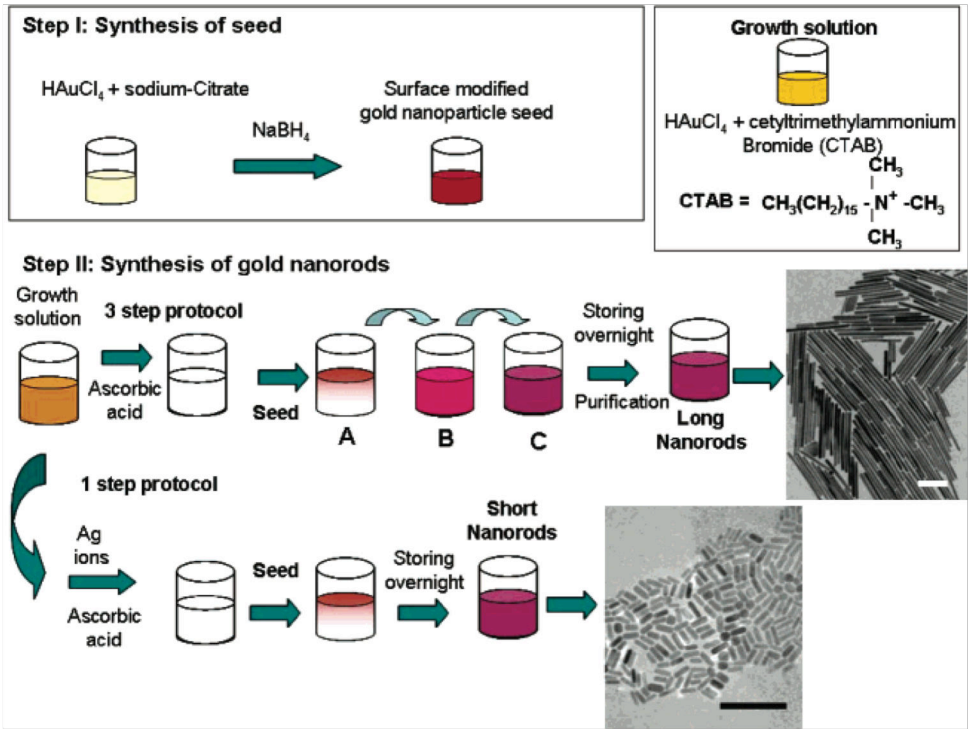

Figure 2.8 *Two-step seed-mediated growth approach for making AuNRs with a controlled AR. (bottom right). Shown at the right are TEM micrographs of the final purified (centrifuged and washed) gold nanorod products. Scale bars represent 200 nm.*[206]

In the first step, citrate-capped AuNPs prepared by the reduction of $HAuCl_4$ with sodium borohydride were used as the seed and the surfactant hexadecyltrimethylammonium bromide (CTAB) is used for micelle template. In the second step, $HAuCl_4$ is reduced to $HAuCl_2$ by ascorbic acid in the presence of CTAB and $AgNO_3$, and then citrate-capped spherical AuNPs are added to this $HAuCl_2$ solution. These spherical AuNPs catalyze the reduction of Au^I to Au^0 by ascorbic acid. A three-step procedure in the absence of $AgNO_3$ allows longer AuNRs with AR of up to 25 to be prepared. For short gold nanorods, $AgNO_3$ and ascorbic acid are added to the growth solution, followed by the seed solution. The yield, monodispersity and tunable AR of AuNRs depends on concentration, size, structure of seed particles; temperature; surfactant; pH; added precursor concentration; aging time; *etc.*[9,133,207–209]

The morphology of the seed particle is one important parameter that triggers the anisotropic growth. Beautiful gold mesoflowers (see Figure 2.9) can be synthesized in large quantity by the seed-mediated method from an oligoaniline capped AuNP seeds at 80 ^{0}C.[203] In this case, presence of multiple twinning in the seed particle leads to anisotropic growth at high temperature.

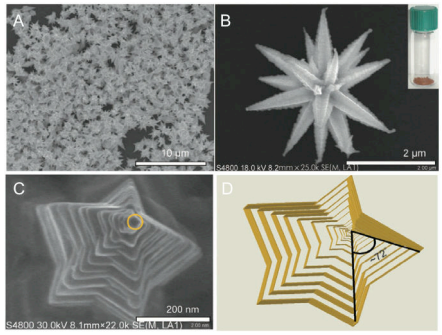

Figure 2.9 *(a) Large area FESEM image of gold mesoflowers anchored on a conducting glass substrate; (b) FESEM image of a gold mesoflower. The inset shows a photograph of the mesoflower powder. (c) Top view of a single stem of the mesoflower showing the pentagonal structure and a nanoparticle on the apex (marked) and (d) a corresponding model.*[203]

The seeded growth procedure for producing five types of differently shaped AuNPs including nanospheres, nanocubes, nanobranches, nanorods, and nanobipyramids in high yield is reported by Chen *et al.*[132]. Nanorods have three different aspect ratios, and nanobipyramids have four different aspect ratios. Two types of AuNP seeds were used. Au nanospheres, nanocubes, and nanorods were grown using the CTAB-stabilized seeds in the presence of CTAB. The growth of Au nanobranches and nanobipyramids employed the citrate-stabilized seeds. Figure 2.10 shows TEM images of AuNPs of different shapes and size. Their yields are shape-dependent, ranging from 50% to 95%.

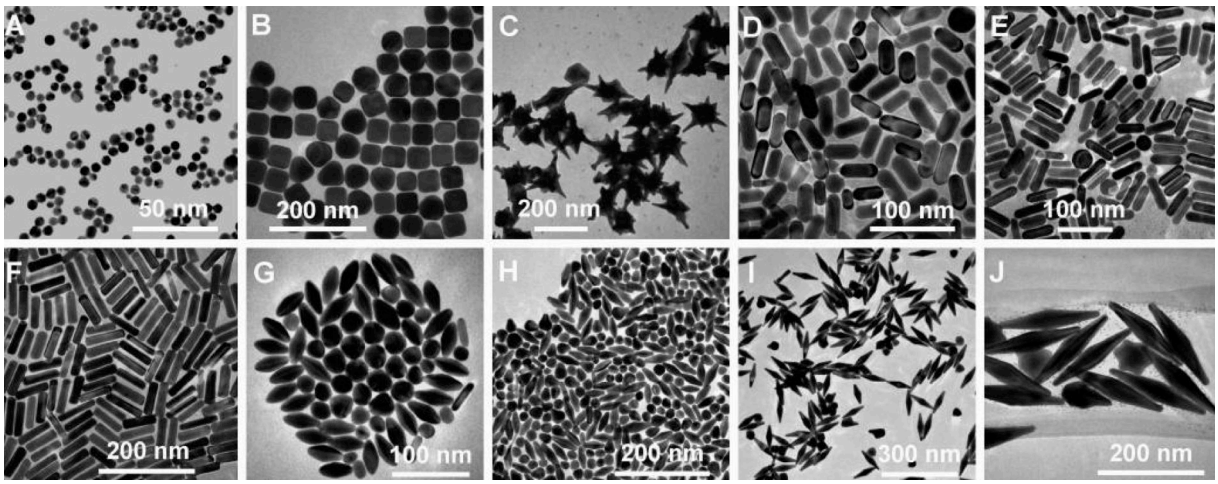

Figure 2.10 *TEM images of AuNPs of different shapes and sizes. (A) Nanospheres. (B) Nanocubes. (C) Nanobranches. (D) Nanorods (AR = 2.4). (E) Nanorods (AR = 3.4). (F)*

Nanorods (AR = 4.6). (G) Nanobipyramids (AR = 1.5). (H) Nanobipyramids (AR = 2.7). (I) Nanobipyramids (AR = 3.9). (J) Nanobipyramids (AR = 4.7).[132]

A new synthetic route has been utilized for the formation of multiple-shaped PtNPs in the presence of a cationic surfactant, CTAB under UV- photoirradiation. The method exclusively generates different shapes, such as spherical particles with different sizes, nanocubes, short or long nanowires, and nanoflakes within a very short time. The reduction of the Pt(IV) ions was done with alkaline 2,7-dihydroxynaphthalene (2,7-DHN) under 3 h UV- photoirradiation in the presence of CTAB. The particle size and shape can be controlled just by changing the molar ratios of the surfactant-to-metal ion and the concentration of the 2,7-DHN[210] (see Figure 2.11).

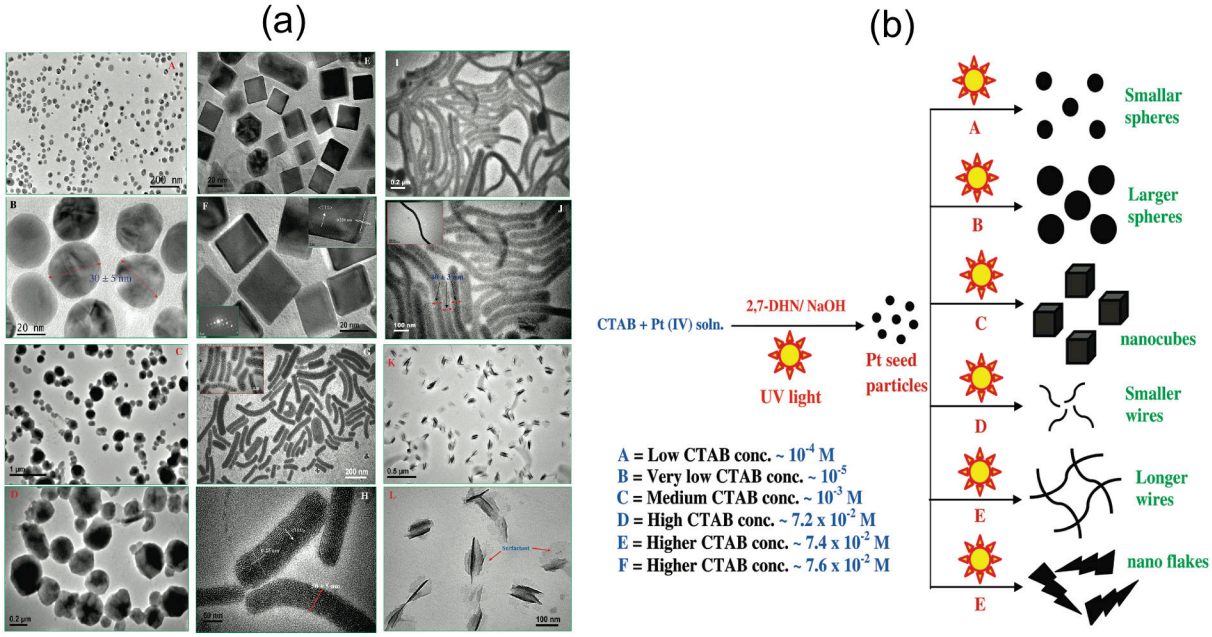

Figure 2.11 *(a) TEM images of different shaped PtNPs. (b) Schematic presentation for the formation of multiple shaped PtNPs at different reaction conditions.*[210]

We have used the seed-mediated synthesis technique for the elaboration of various NMNPs (gold nanospheres and nanorods, platinum nanoflowers).[19,20]

The polyol synthesis, where different seeds can grow towards nanoparticles having different shapes (see Figure 2.12), must also be mentioned. For example, a single-crystal seed can grow to an octahedron or cube by controlling the relative growth rates along the (100) and (111) directions, plate-like seeds grow to hexagonal and then eventually triangular plates, *etc*.

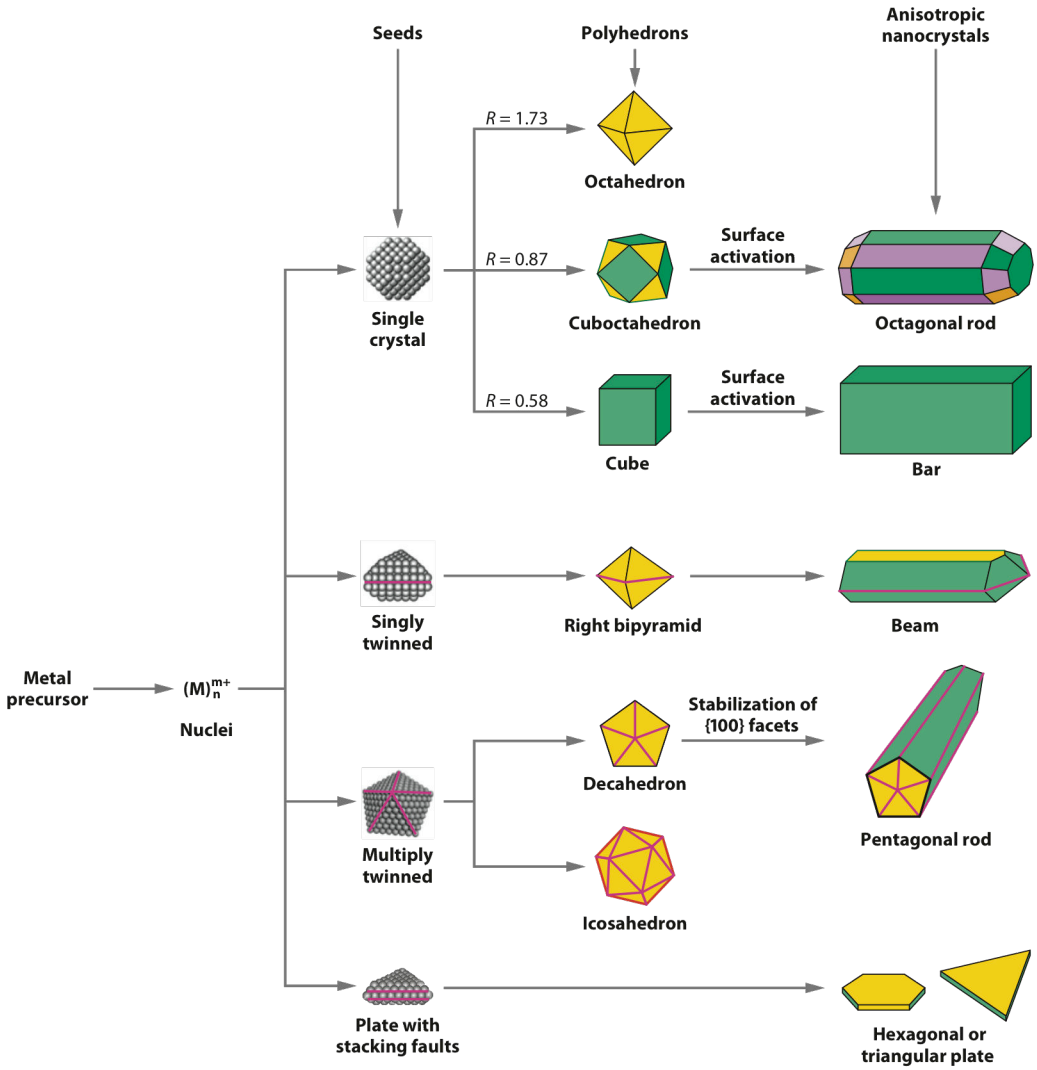

Figure 2.12 *A scheme illustrating the various stages of the reaction that leads to the formation of noble-metal nanoparticles with different shapes. After the formation of nuclei (small clusters), they become seeds with a single-crystal, singly twinned, or multiply twinned structure. Stacking faults in the seeds results in plate-like structures. Green, orange, and purple represent the (100), (111), and (110) facets, respectively. The parameter R is defined as the ratio between the growth rates along the (100) and (111) directions. Twin planes are delineated in the drawing with magenta lines.*[202,204,211]

The strong electromagnetic fields at the surfaces of anisotropic NMNPs make them useful for NLO applications in photonics as well as chemical and biological detection. This seed-mediated growth method has specific advantages over the other existing methods to control the size and shape of nanoparticles. A considerable amount of effort has been devoted for developing various NMNPs with high second-order NLO properties.[204,212]

2.4. Structural characterization methods

2.4.1. Transmission electron microscopy (TEM)

The transmission electron microscope (TEM) is a very powerful tool for material science. TEM is a microscopy technique in which a beam of electrons is transmitted through an ultra-thin specimen, interacting with the specimen as it passes through it. An image is formed from the interaction of the electrons transmitted through the specimen; the image is magnified and focused onto an imaging device, such as a fluorescent screen, or a layer of photographic film, or is detected by a sensor such as a charge coupled device (CCD) camera. The image detected by the CCD may be displayed in real time on a monitor or a computer.

In TEM, the source of illumination is a beam of electrons of very short wavelength, emitted from a tungsten filament at the top of a cylindrical column of about 2 m high. The whole optical system of the microscope is placed in vacuum. Air must be evacuated from the column to create a vacuum to avoid the collision of electrons with air molecules and hence their scattering. Along the column, at specific intervals magnetic coils are placed. Just as the light is focused by the glass lenses in a light microscope, these magnetic coils in the electron microscope focus the electron beam. The magnetic coils placed at specific intervals in the column acts as an electromagnetic condenser lenses system. The specimen is stained with an electron dense material and is placed in the vacuum. The electron beams pass through the specimen and are scattered by its internal structures. Figure 2.13 shows a schematic TEM set-up. There are four parts for a transmission electron microscope:

- Electron source
- Electromagnetic lens system
- Sample holder
- Imaging system

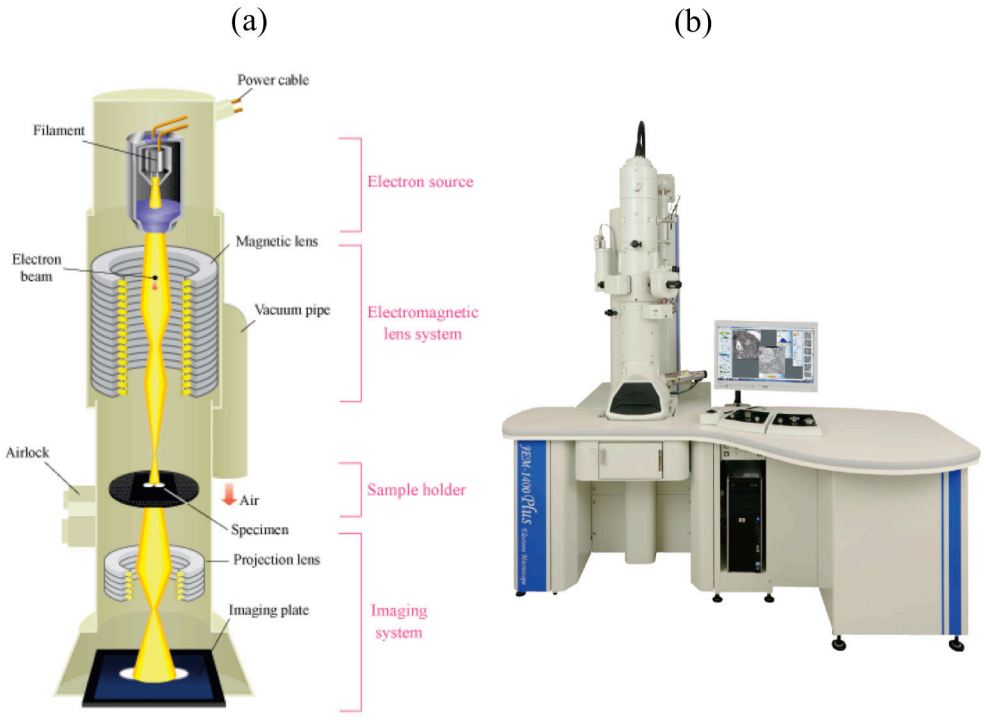

Figure 2.13 *(a) Schematic TEM set-up. (b) Photograph of TEM JEOL Model JEM-1400.*

High-resolution TEM enables to determine the positions of atoms within materials, which has made an indispensable tool for nanotechnologies research and development in many fields, including heterogeneous catalysis and the development of semiconductor devices for photonics and electronics.

In this work, we have used a TEM as pictured in Figure 2.13 (b) located at the Polytechnic Institute of Ho Chi Minh City (Viet Nam).

2.4.2. X-ray diffraction (XRD)

X-ray diffraction (XRD) is a very important experimental technique that has long been used to address all issues related to the crystal structure of solids, including lattice constants and symmetry, identification of unknown materials, orientation of single crystals, preferred orientation of polycrystals, defects, stresses, *etc*. In XRD, a collimated beam of X-rays, with a wavelength ranging typically from 0.7 to 2 Å, is incident on a specimen and is diffracted by the crystalline phases in the specimen according to Bragg's law:

$$n\lambda = 2d\sin\theta$$

where d is the spacing between diffracting planes, θ is the incident angle, n is any integer, and λ is the wavelength of the beam (see Figure 2.14).

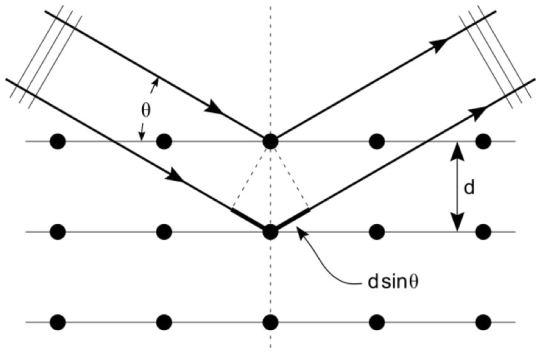

Figure 2.14 *Illustration of Bragg's law: reflection of X-rays from two planes of atoms in a solid.*

The intensity of the diffracted X-rays is measured as a function of the diffraction angle 2θ and the specimen's orientation (see Figure 2.15). This diffraction pattern is used to identify the specimen's crystalline phases and to determine its structural properties. XRD is nondestructive and does not require elaborate sample preparation, which partly explains the wide usage of XRD method in materials characterization.[78]

(a) (b)

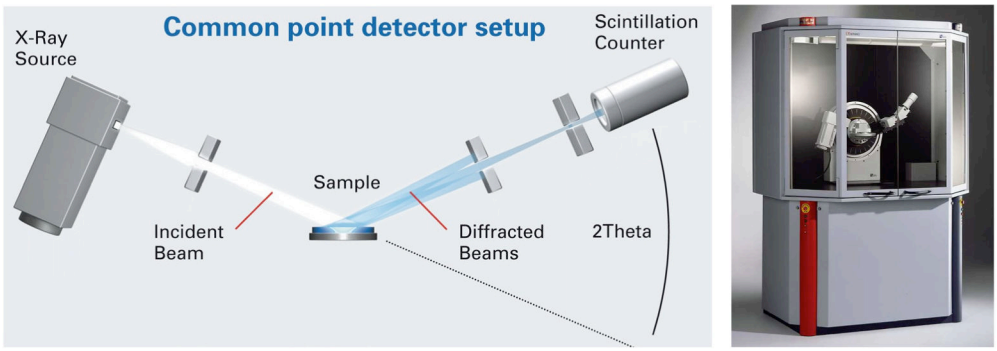

Figure 2.15 *(a) Schematic outline of a XRD (b) Photograph of XRD Bruker D8 Advanced.*

XRD can be used to measure the average spacings between layers or rows of atoms, to determine the orientation of a single crystal or grain, to find the crystal structure of an unknown material and to measure the size, shape and internal stress of small crystalline regions.

In this PhD thesis, we have used the X-ray set-up as pictured in Figure 2.15 at East Paris Institute of Chemistry and Materials Science.

2.5. UV-Vis spectroscopy

Spectroscopy is based on the study of the interaction between radiation and matter. UV-Vis spectroscopy has been widely used for the characterization of nano-materials. This absorption spectroscopy uses electromagnetic radiations between 190 nm to 800 nm and is divided in the ultraviolet (UV, 190-400 nm) and visible (Vis, 400-800 nm) regions.

The basic parts of a spectrophotometer are a light source, a sample holder, a diffraction grating or monochromator to separate the different wavelengths, and a detector (see Figure 2.16). The optical beam is split in two beams before it reaches the sample; one of them is used as sample light beam (Intensity I) and another is a reference light beam (Intensity I_0). The intensities transmitted from sample and reference beams are measured simultaneously by photodetectors. Spectrophotometry is used for both qualitative and quantitative investigations of samples.[129]

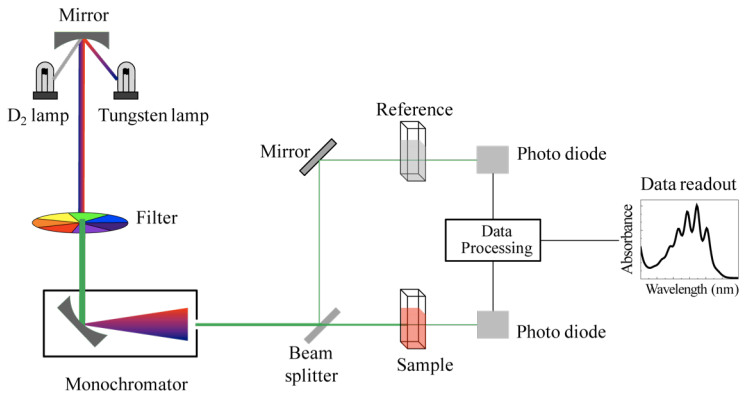

Figure 2.16 *Schematic of UV- visible spectrophotometer.*

A spectrophotometer records the absorption of sample at different wavelengths and gives absorbance (A) versus wavelength (λ), known as a spectrum. The wavelengths of maximum absorption peaks (λ_{max}) can be correlated with the types of bonds in a given molecule and can help, in some cases, to identify some functional groups of a molecule.

This method is most often used in a quantitative way to determine concentrations of an absorbing species in solution. The Beer-Lambert law states that the absorbance of a solution is directly proportional to the concentration of the absorbing species in the solution and the path length. The ratio I / I_0 is known as transmittance T and the logarithm of the inverse ratio I_0 / I is known as the absorbance A. For liquids, these relations are usually written as:

$$A = \log_{10}(I_0 / I) = \varepsilon c L$$

where,

A : the measured absorbance, in Absorbance Units (AU), I_0 is the intensity of the incident light at a given wavelength, I is the transmitted intensity;

ε : molar absorbance or absorption coefficient [dm^3 mol^{-1} cm^{-1}];

c : the concentration of the absorbing species [mol dm^{-3}];

L : the path length through the sample [cm].

The Lambert-Beer law can be limited by chemical or instrumental factors such as deviations in absorptivity coefficients at high concentrations (>0.01M) due to electrostatic interactions between neighbouring molecules; scattering of light due to particules in the sample; fluorescence or phosphorescence of the sample; changes in refractive index at high concentrations; shifts in chemical equilibrium as a function of concentration; non-monochromatic radiation. These deviations can be minimized by using diluted and well-filtered solutions.

We have used a Perkin-Elmer Lambda 950 UV-Vis spectrophotometer available at LPQM.

2.6. Harmonic Light Scattering at 1064 nm

The approach followed here relies on HLS as initially proposed and developed by Terhune and Maker.[6,213] A transverse single mode Nd^{3+}: YAG laser is used as the fundamental source, consisting of 10 MW peak power, 3 ns duration infrared (IR) pulses at 1.064 µm repetition rate 10 Hz). The incident IR intensity can be continuously monitored by a half-wave plate rotated between two crossed Glan polarizers (Figure 2.17). A small part of the incident beam is removed at a low reflection angle by a glass plate and sent onto a highly nonlinear NPP[63] powder used as a reference frequency doubler. The emitted second harmonic signal is detected by a photomultiplier.

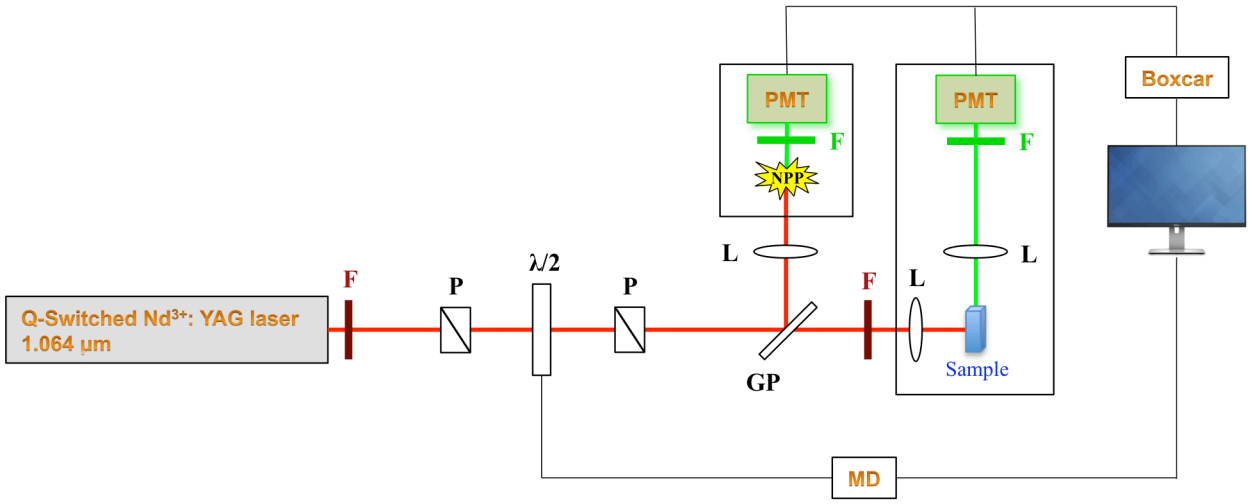

Figure 2.17 *Schematic representation of HLS at 1.064 µm. F: Filter; L: Lens; λ/2: Half wave plate; P: Polarizer; GP: Glass plate; PMT: Photomultiplier tube; MD: Motor driver; and NPP: Reference material.*

The main fundamental beam (vertically polarized) is focused into the sample using an 8 cm focal length converging lens. The sample consists in an adequately designed parallelepipedic spectrophotometric cell presenting four polished windows so as to allow for simultaneous longitudinal illumination and transverse collection of the scattered emission. Collection of the HLS photons at 532 nm is performed in the transverse off-axis 90° direction, using a large (diameter 50 mm) and short focal distance (f = 50 mm) spherical lens in order to focus the light onto the photocathode of a photomultiplier tube. The numerical aperture of the

optical collection system is low so as to avoid the depolarizing contribution of the off-axis beams. The detected reference and scattered harmonic signals, after spectral selection through an interference filter with 5 nm spectral resolution, are then sampled and averaged using a home-made acquisition card and processed by a computer. The variation of the scattered second harmonic intensity from the solution is recorded on the computer as a function of the reference second harmonic signal provided by the NPP powder, which scales like the square of the incoming fundamental intensity. Then $\langle \beta^2 \rangle$ and β (defined as $\sqrt{\langle \beta^2 \rangle}$) values are inferred from the slopes of the resulting lines. Calibrations are made with respect to the pure water solvent.

For $\langle \beta^2 \rangle$ measurements, the variation of the second harmonic intensity scattered from the solvent is recorded on the computer as a function of the reference second harmonic signal provided by the NPP powder, both signals scaling as the square of the incoming fundamental intensity I_ω.

The scattered harmonic signal $I^{2\omega}$ from a solvent is given by:

$$I_S^{2\omega} = g_S f_S N_S \langle \beta_S^2 \rangle I_\omega^2 \tag{2.1}$$

where g_S is a geometry factor, N_S is the number of solvent molecules per unit volume; field f_S is the local factor for the solvent, β_S is the molecular hyperpolarizability of the solvent.

Similarly, the second harmonic signal collected from the reference material (NPP powder) is

$$I_{NPP}^{2\omega} = K_{NPP} I_\omega^2 \tag{2.2}$$

The slopes P_0 of the lines obtained for the solvent by recording the variation of $I^{2\omega}$ as a function of $I_{NNP}^{2\omega}$ (the SHG intensity from a reference NLO material (NPP) sample which is proportional to I_ω^2)

$$P_0 = g_S f_S N_S \frac{\langle \beta_S^2 \rangle}{K_{NPP}} \tag{2.3}$$

In the second step, we change the solvent cell with the cell containing the solution of the molecule to be investigated. By considering that the molecules of solute are completely dissolved in the solvent and that the emission of the scattered second harmonic intensity by the solution is described by an additive model, we have

$$I^{2\omega} = gf\left[N_S\left\langle\beta_S^2\right\rangle + N\left\langle\beta^2\right\rangle\right]I_\omega^2 \tag{2.4}$$

where g is a geometry factor, f is the local field factor for the solution, N_S and N are the number of solvent molecules and analyte molecules per unit volume respectively; β_S and β are the molecular hyperpolarizability of the solvent and nanoparticle, respectively.

The slope of the solution is then given by

$$P = gf\frac{\left[N_S\left\langle\beta_S^2\right\rangle + N\left\langle\beta^2\right\rangle\right]}{K_{NPP}} \tag{2.5}$$

In the hypothesis, where g_S (solvent) ≈ g (solution) (assuming a small difference between the local field factor of solution and that of the pure solvent), the ratio of the two slopes can obtained

$$\frac{P}{P_0} = \frac{\left[N_S\left\langle\beta_S^2\right\rangle + N\left\langle\beta^2\right\rangle\right]}{N_S\left\langle\beta_S^2\right\rangle} \tag{2.6}$$

Therefore,

$$\beta = \beta_S\sqrt{\frac{N_S}{N}\left(\frac{P}{P_0} - 1\right)} \tag{2.7}$$

Knowing the β_S value of the solvent, we deduce the β value of the analyte molecules.[6,7,9,56]

The β value of water has been determined in our laboratory by performing HLS measurements at 1.064 μm on pure water and on carbon tetrachloride used as a reference. As reported by Terhune and Maker[6] we took $\beta_{CCl_4} = 0.265\times10^{-30} esu$, resulting in a $\beta_{H_2O} = 0.055\times10^{-30} esu$. This value has been confirmed by another experiment taking

chloroform as the reference solvent, with $\beta_{CHCl_3} = 0.19 \pm 0.02 \times 10^{-30} esu$. This latter solvent having been widely used in previous HLS studies by S. Brasselet *et al.*[214,215] for hyperpolarizability measurements of standard dyes, β values of these dyes have been found to the quite consistent with those of the literature, then validating the β_{HLS} value of the chloroform reference solvent.

It must be pointed-out that some earlier publications of literature used a β value of 0.56×10^{-30} esu for water. However, this value has a unique and questionable source. In the earliest report of this β value[72] the quote associated to this value (ref.[216]) is the following: "Boutton, C.; Clays, K., Private communication". There is no clear report on the measurement of this β value (method used – HLS or EFISH? – measurement wavelength, absolute or relative NLO measurement). Most subsequent works using this β value are based on this reference, without further experimental check of this value. Now, all authors use β values ranging from 0.06 to 0.08×10^{-30} esu for water, depending on the fundamental wavelength.

As proposed by other authors,[10–14] from these β values, the β values per silver atom, *i.e.* β', have been calculated according to the relation[12,217,218]

$$\beta' = \frac{\beta}{\sqrt{N}} \tag{2.8}$$

where N is the number of atoms per nanoparticle. This relation is valid for a centrosymmetric assembly (e.g. a nanoparticle [217] or a dendrimer [218]) of N individual objects (molecules, or atoms in the present case). It must be pointed-out that this β' value has no real significance for a single atom, but may help to understand the influence of shape and size on the NLO response of different nanoparticles containing similar numbers of metal atoms.

The HLS set-up of LPQM has been used in this work. The laser source is a transverse single mode Nd^{3+}: YAG laser (SAGA from Thales Laser) operating at 10 Hz and delivering 3 ns pulses of a few mJ energy per pulse. PMT's are from Hamamatsu, acquisition is performed using home-made cards and software implemented by Colin Lopez from the Physics Department of ENS Cachan.

2.7. Variable incident polarization in HLS experiments at 1.064 µm

Variable incident polarization has been implemented to identify the dipolar and the multipolar contributions to the hyperpolarizability tensor from a simple analysis of the harmonic scattering depolarization ratio.[214] The HLS set-up has been adapted to allow for polarization dependent measurements as shown in Figure 2.18 below.

The constant incident intensity is monitored by a first half-wave plate and a Glan polarizer, and the fundamental polarization is controlled by the rotation of a second half wave plate. The second harmonic emitted by the NPP powder is used as a reference so as to level off pulse-to-pulse fluctuations.

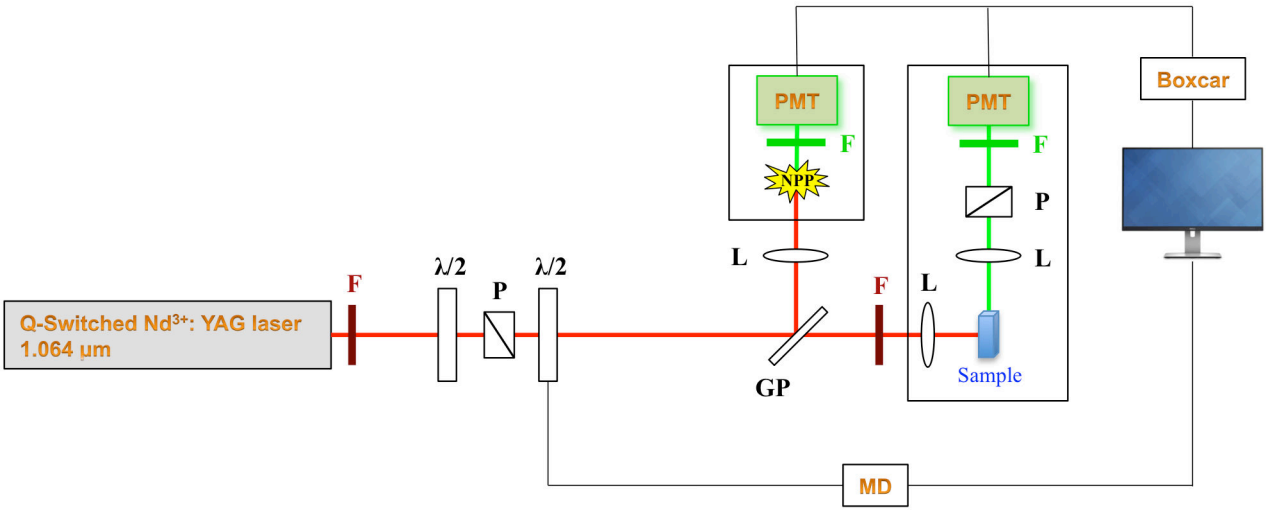

Figure 2.18 *Schematic representation of Variable incident polarization in Harmonic Light Scattering (VIP-HLS) at 1.064 µm. F: Filter; L: Lens; λ/2: Half wave plate; P: Polarizer; GP: Glass plate; PMT: Photomultiplier tube; MD: Motor driver; and NPP: Reference material.*

Different polarization configurations as shown in Figure 2.19 can be used to evaluate the $\langle \beta^2_{IJK} \rangle$ components, which subsequently permit to retrieve the nonlinear anisotropy of the β tensor. In the absence of an analyzer, the overall scattering intensity exhibits a simple oscillatory pattern:

$$I^{2\omega} \propto \left[N_1 \left(\left\langle \beta^2_{1,XXX} \right\rangle + \left\langle \beta^2_{1,ZXX} \right\rangle \right) + N_2 \left(\left\langle \beta^2_{2,XXX} \right\rangle + \left\langle \beta^2_{2,ZXX} \right\rangle \right) \right] \cos^2 \varphi + 2 \left[N_1 \left\langle \beta^2_{1,ZXX} \right\rangle + N_2 \left\langle \beta^2_{2,ZXX} \right\rangle \right] \sin^2 \varphi \qquad (2.9)$$

where the subscript 1 (resp. 2) refers to the solvent (resp. the solute). The fundamental beam propagates along Z and is polarized in the (X-Y) plane, $\phi = 0$ for a fundamental polarization parallel to the vertical X-axis.

A polar plot of $I^{2\omega}$ as a function of ϕ depends on the relative weight of the dipolar and multipolar contributions to the hyperpolarizability tensor of the metallic nanoparticles. As mentioned above, this contribution remains mostly dipolar if the diameter of the particle is much smaller (by a factor of 10 at least) than that the fundamental wavelength.

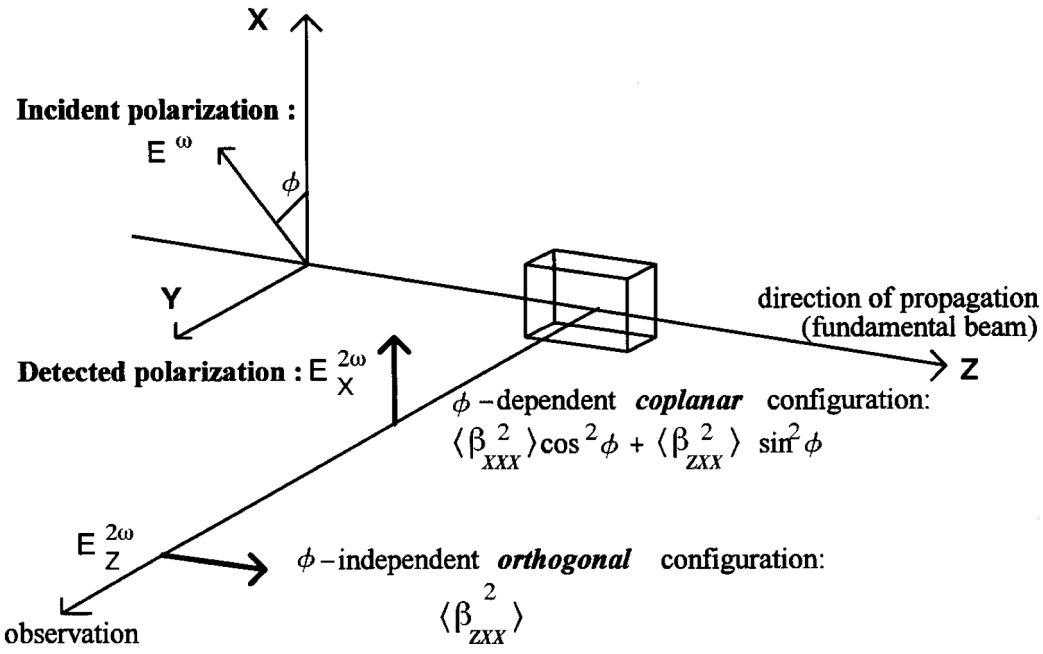

Figure 2.19 *Fundamental incoming beam propagating along Z and polarized in the (X, Y) plane. The observation direction is along Y, and polarization state of SH along X or Z plane.*

An illustration of this phenomenon has been given in in Figure 1.15 above. In the small-particle limit (diameter << $\lambda/2\pi$), the SHG signal vertically-polarized along the X axis is dominated by a dipolar contribution, resulting in a two-lobes polar plot of the second harmonic signal with respect to the pump-polarization angle. The pump-polarization dependence of the 2ω signal changes when increasing the nanoparticle diameter. In the polarization diagrams shown in Figure 1.15 (b) and Figure 1.15 (c), two new lobes arise from

the initial 1-D pattern when the particle diameter increases above 50 nm, resulting in a four-lobe polar plot for particles with a 100 nm diameter and above, typical of a significant multipolar contribution.

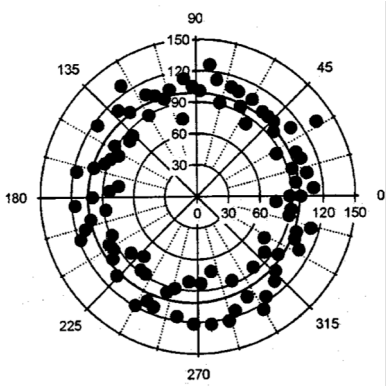

Figure 2.20 *Polar plot of the SH intensity along the Z component, for a 20-nm gold nanoparticle at a 800 nm fundamental wavelength.*[16]

On the contrary, as shown in Figure 2.20, the polar plot for small gold nanospheres for a Z-polarized SH signal is independent of the polarization angle of the pump beam. Some authors[219] have shown that this ϕ-independent plot can change due to interferences between dipolar and octupolar contributions to the SH emission of nanoparticles, leading to polarization-dependent patterns, but this effect is detectable for bigger nanospheres (diameter higher than 100 nm) only. In our work, our particle sizes are significantly below this upper limit.

Chapter 3
Metallic nanospheres: from colloids to dry nanoparticles

3.1. Introduction

Noble metal nanoparticles (NMNPs) such as gold and silver have been the focus of many investigations for potential applications in optoelectronic and biophotonic devices.[220–227] Various approaches to synthesis of NMNPs have been reported such as chemical reduction, UV photolysis, gamma irradiation, metal vapor deposition, laser ablation, sputtering... Among these, chemical reduction is the most extensively investigated synthesis method.

The size and shape of NMNPs affect significantly their physical and chemical properties, especially their linear and nonlinear optical response. Many investigations have been focused on controlling the size and shape of NMNPs, with various synthesis conditions and methods for nanospheres,[228,229] nanorods,[230–235] nanostars,[236,237] nanoflowers[238] and so on.

There exists several reports of SHG from gold and silver nanospheres (AuNSs and AgNSs), possibly the earliest reports for metallic nanoparticles.[9,10,22,23] A large number of data concerning hyperpolarizability values of NMNPs data is currently available, experiments being performed at various fundamental wavelengths λ and for a wide choice of particle sizes. For similar types of metallic nanoparticles, the reported β values may vary by at least one order of magnitude depending on the authors, not only due to different measurements conditions, but also to discrepancies of hyperpolarizability values of the reference solvent (usually water) as discussed in the previous chapter.

In this part we decided to concentrate on small metallic nanospheres made of gold (diameters 3.0; 11.6; 15.8; 17.4; 20.0, 43.0 and 80.0 nm, *i.e.* lower than 0.1.λ) and silver, and to focus on a systematic investigation of the influence of the AuNP surface area on their β values, in comparison with other results previously reported in the literature. Previous reports evidenced a fourth-power dependence of the HLS intensity with respect to nanosphere diameters,[16] but no quantitative hyperpolarizability values have been systematically provided for a large range of surface areas. Here we will explore the effect of surface area on AuNSs with diameters ranging from 3.0 to 80.0 nm, in order to reach the upper as well as the lower limit of validity of the purely dipolar origin of β values. The fundamental wavelength is 1064 nm, significantly higher than that chosen in ref.[16], allows to measure β values with a strong plasmon resonance enhancement at the harmonic frequency. In our case, the accuracy on β values (± 15%) is slightly better than in ref.[16] (± 20%).

We also investigated β values of some AgNSs in solution, and we have also fabricated and characterized dry AgNSs which display interesting nonlinear optical (NLO) responses in the solid state. AgNSs were produced by two methods. Firstly, AgNSs in aqueous solution were synthesized by reduction of silver nitrate with $NaBH_4$ in protective solutions (PVA, PVP). Secondly, powdery-AgNSs were fabricated by thermal decomposition of silver oxalate, this method allowing the fabrication of highly pure AgNSs without requiring the addition of protective or reducing agents. The resulting nanoparticles were characterized by a Kurtz and Perry Powder Test using a set-up similar to Harmonic Light Scattering (HLS).[25]

3.2. Experimental

3.2.1. Materials

Tetrachloroauric (III) acid trihydrate ($HAuCl_4.3H_2O$), ascorbic acid ($C_6H_8O_6$), tri-sodium citrate ($C_6H_5Na_3O_7.2H_2O$), silver nitrate ($AgNO_3$, 99%), sodium borohydride ($NaBH_4$, 99.99%), hexadecyltrimethylammonium bromide (CTAB, $C_{19}H_{42}BrN$ 99%), oxalic acid ($H_2C_2O_4$, 99%), Poly(vinylpyrrolidone) (PVP; 40 000 g mol^{-1}), Poly(vinylalcohol) (PVA; 40 000 g mol^{-1}) and gold nanospheres (size ~ 80.0 nm) are purchased from Sigma-Aldrich. The solutions were prepared using ultra-pure water from a Millipore system (18 MΩ cm^{-1}) throughout the experiment. All aqueous samples are at natural pH = 7.

3.2.2. Synthesis of NMNPs

❖ **Gold colloidal solutions**

The synthesis of AuNS is based on one of these two standard reactions:

$$8AuCl_4^- + 3BH_4^- + 9H_2O \rightarrow 8Au + 3BO_3^{3-} + 32Cl^- + 30H^+$$

(reduction by BH_4^-, for small particles and seeds)

$$2AuCl_4^- + 3C_6H_8O_6 \rightarrow 2Au + 8Cl^- + 3C_6H_6O_6 + 6H^+$$

(reduction by ascorbic acid, for larger particles)

Actually, these reactions are very fast and their equilibrium constants *K* are very large, so the reaction process is complete, eliminating the $AuCl_4^-$ ions after syntheses.

Small-size AuNSs (3.0 nm). A 20 mL aqueous solution containing 1.45×10^{-4} M $HAuCl_4$ and 5×10^{-4} M tri-sodium citrate was prepared. Next, 0.3 mL of 0.01 M $NaBH_4$ solution was quickly added to the solution while stirring. The solution turned pink immediately after adding $NaBH_4$, indicating particle formation.

Medium-size AuNSs (11.6; 15.8; 17.4 and 20.0 nm). In the typical synthesis, different protective agents (PVA, PVP) were dissolved in 20 mL H_2O Millipore under stirring. After the complete dissolution of the protective agent, $HAuCl_4$ 0.029 M was added, the solution being stirred for 5 min. Then, an aqueous solution of ascorbic acid 0.1 M was added into the liquid. The colour of solution slowly changed from white to red.

The seed-mediated growth method is so far the most popular method for the synthesis of colloidal Au large-size nanospheres and nanorods. This technique is implemented according to a two-step procedure.[228–231,239–241]

Seed solution. The first step consists in the preparation of gold spherical nanoparticle seeds. This preparation was performed starting from a 10 mL aqueous solution of CTAB 0.1 M. Then, 0.1 mL $HAuCl_4$ 0.029 M was added under stirring. After that, 0.15 mL $NaBH_4$ 0.01 M was then slowly added. The seed solution was kept for various durations (0.5, 1 h) before being used. This solution was then used as the seeding solution for the growth of the nanorods (see Chapter 4) and large-size nanospheres.

Larger-size AuNSs (43.0 nm). In the second step, 10 mL of growth solution, containing 1.45 $\times 10^{-4}$ M $HAuCl_4$ and 0.025 M CTAB, was mixed with a 0.055 mL of 0.1 M freshly prepared ascorbic acid solution. Next (after 1 h), 0.02 mL of the seed solution was added and stirred. Within 5-10 min, the solution color changed to deep red.

❖ **Silver colloidal solutions**

In the typical synthesis, the different protective agents (PVA, PVP) were dissolved in 20ml H_2O Millipore under stirring. After the complete dissolution of the protective agent, $AgNO_3$ 0.1 M was added, the solution being stirred for 5 min. Then, an aqueous solution of $NaBH_4$ 0.1 M was added into the liquid. The colour of solution immediately changed from white to yellow (lemon chrome). By changing several parameters like the type and concentration of protective agent and the ratio of silver nitrate to $NaBH_4$, we can control the particle size and morphology in these solutions. Therefore, a systematic study of the influence of synthesis conditions on particle size and concentration has been preliminary undertaken. We have performed this study using PVA on one hand, PVP on another hand. The volume of Millipore water in all experiments was 20ml, and the concentration of $AgNO_3$ was fixed at 0.1 M. As TEM characterization could not be performed on all samples, the evolution of particle size and concentration was qualitatively evaluated by UV-visible spectroscopy.

The protective agent PVA

Table 3.1 and Figure 3.1 report the synthesis conditions and UV-visible data for AgNSs capped with PVA.

Table 3.1 *UV-Visible data for silver colloidal solutions with protective agent PVA.*

Sample	PVA (mg)	$AgNO_3$ 0.1 M (ml)	$NaBH_4$ 0.1 M (ml)	n_{AgNO_3} / n_{NaBH_4}	Wavelength λ_{max} (nm)	Absorbance
AgPVA 1.1	20	0.1	0.1	1	**394**	**1.37**
AgPVA 1.2	20	0.1	0.2	1/2	**395**	**1.60**
AgPVA 1.3	20	0.1	0.3	1/3	**398**	**1.74**
AgPVA 1.4	20	0.1	0.4	1/4	**400**	**1.59**
AgPVA 1.5	20	0.1	0.5	1/5	**398**	**1.55**
AgPVA 1.6	20	0.1	1	1/10	**395**	**1.48**

AgPVA 2.1	10	0.1	0.2	1/2	**390**	**1.31**
AgPVA 2.2	20	0.1	0.2	1/2	**395**	**1.60**
AgPVA 2.3	30	0.1	0.2	1/2	**400**	**1.82**
AgPVA 2.4	40	0.1	0.2	1/2	**400**	**2.01**
AgPVA 2.5	50	0.1	0.2	1/2	**400**	**1.93**
AgPVA 2.6	100	0.1	0.2	1/2	**406**	**1.82**

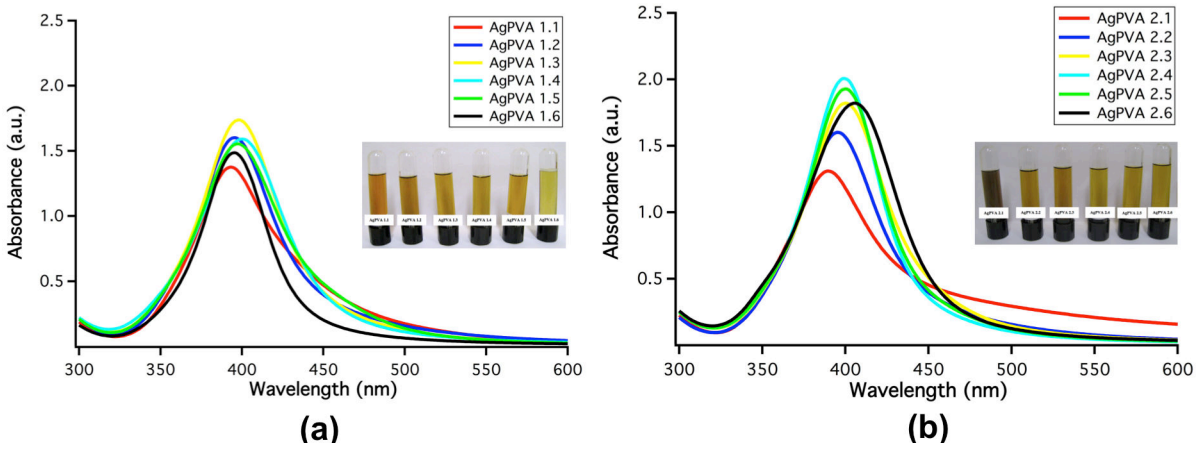

Figure 3.1 *UV-Vis Absorption spectra of synthesized AgNSs with the protective agent PVA: (a) Different concentrations of $NaBH_4$ 0.1M (0.1; 0.2; 0.3; 0.4; 0.5; 1 ml); (b) Various amount of protective agent PVA (10; 20; 30; 40; 50 and 100 mg).*

In Figure 3.1 (a), the peak intensity increases from 1.37 to 1.74 when increasing the concentration of $NaBH_4$ by adding 0.1 to 0.3 ml of a 0.1 M $NaBH_4$ solution to the reacting medium, showing that the number of nanoparticle increases. The size of silver particles also increases, as can be seen from the red shift of the peak maximum (from 394 to 398 nm), but this change remains quite modest.

By further increasing the $NaBH_4$ amount (by adding 0.3 to 1 ml), the peak intensity decreases from 1.74 to 1.48. When the number of nanoparticles increases too much, nanoparticles easily agglomerate together, then decreasing the total number of nanoparticles.

The ratio n_{AgNO_3} / n_{NaBH_4} = 1/2 will be used to study the effect of the quantity of the protective agent PVA on the number and size of nanoparticles.

In Figure 3.1(b), the peak intensity increases from 1.31 to 2.01 corresponding to the increase of the amount of protective agent PVA (from 10 to 40 mg), resulting in an increase of the number of nanoparticles. The size of AgNSs increases as inferred from the red shift of the position of the peak maximum (from 390 to 400 nm).

When further increasing the amount of protective agent PVA (from 40 to 100 mg), the peak intensity decreases from 2.01 to 1.82. A possible interpretation could be related to the fact that the PVA polymer chains on the surface of nanoparticles will coil together and collapse on the surface. Therefore, nanoparticles easily agglomerate together, then increasing the particle size and reducing the number of nanoparticles.

The best results (sample AgPVA 2.2) were identified for the ratio $n_{AgNO_3}/n_{NaBH_4} = 1/2$ and for 20 mg of protective agent PVA.

The protective agent PVP

AgNSs syntheses were also performed using various concentrations of $NaBH_4$ and of the protective agent PVP. Results are shown in Table 3.2 and Figure 3.2.

Table 3.2 *Synthesis conditions and UV-Visible results for silver colloidal solutions with protective agent PVP.*

Sample	PVP (mg)	$AgNO_3$ 0.1 M (ml)	$NaBH_4$ 0.1 M (ml)	n_{AgNO_3}/n_{NaBH_4}	Wavelength λ_{max} (nm)	Absorbance
AgPVP 1.1	20	0.1	0.1	1	**398**	**1.50**
AgPVP 1.2	20	0.1	0.2	1/2	**399**	**1.65**
AgPVP 1.3	20	0.1	0.3	1/3	**399**	**1.44**
AgPVP 1.4	20	0.1	0.4	1/4	**398**	**1.37**
AgPVP 1.5	20	0.1	0.5	1/5	**397**	**1.24**
AgPVP 1.6	20	0.1	1	1/10	**417**	**0.84**
AgPVP 2.1	10	0.1	0.2	1/2	**396**	**1.64**
AgPVP 2.2	20	0.1	0.2	1/2	**399**	**1.65**
AgPVP 2.3	30	0.1	0.2	1/2	**400**	**1.75**
AgPVP 2.4	40	0.1	0.2	1/2	**400**	**1.67**
AgPVP 2.5	50	0.1	0.2	1/2	**401**	**1.65**
AgPVP 2.6	100	0.1	0.2	1/2	**399**	**1.59**

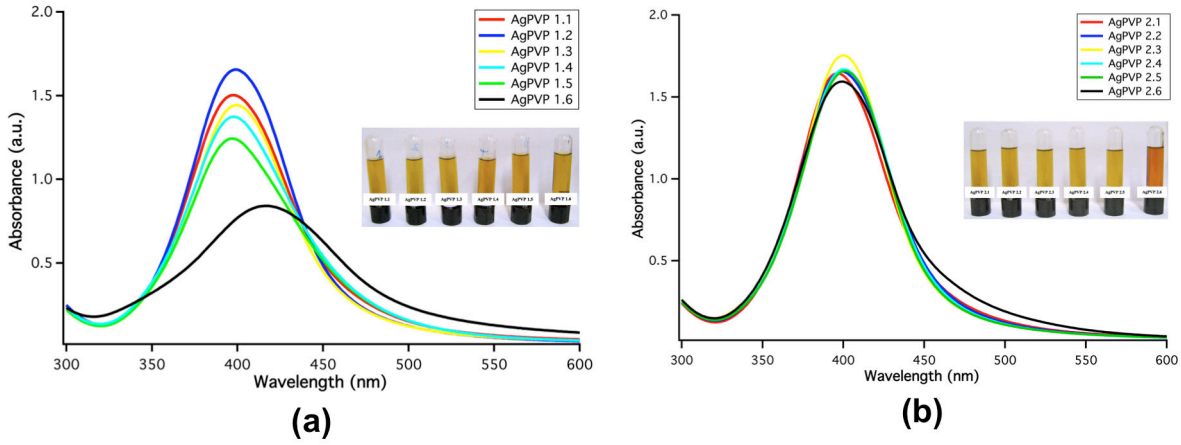

Figure 3.2 *UV-Vis Absorption spectra of synthesized AgNSs with the protective agent PVP: (a) Different quantities of $NaBH_4$ 0.1M (0.1; 0.2; 0.3; 0.4; 0.5; 1 ml); (b)Various amounts of protective agent PVP (10; 20; 30; 40; 50 and 100 mg).*

In Figure 3.2, the best results (sample AgPVP 2.3) were found for a ratio $n_{AgNO_3}/n_{NaBH_4} = 1/2$ and for 30 mg of protective agent PVP.

In the same reaction conditions, the size of AgNSs (with protective PVA) was always smaller than AgNSs (with protective PVP), $\lambda_{max}(PVA) < \lambda_{max}(PVP)$. It means that PVA plays a better protective role than PVP.

❖ **Powdery-AgNSs**

The synthesis of AgNSs is made in two steps: precursor synthesis and thermal decomposition of the precursor. The reactions are:

$$2AgNO_3 + H_2C_2O_4 \rightarrow Ag_2C_2O_{4(s)} + 2HNO_3 \qquad Ag_2C_2O_{4(s)} \xrightarrow{200°C} 2Ag_{(s)} + 2CO_{2(g)}$$

Preparation of silver oxalate precursor. Silver oxalate was synthesized by the precipitation method. The white-formed precipitate was filtered, washed with distilled water, dried in an air oven for 1 h and stored in a dark bottle.

Fabrication of powdery-AgNSs. Powdery-AgNSs was produced by thermal decomposition of silver oxalate. The temperature of calcination is 200 °C during 1 hour.

3.3. Results and Discussion

3.3.1. UV-Vis spectroscopic of metallic colloidal solution

❖ **Gold nanospheres**

In order to optically characterize the AuNSs solutions, their UV−Vis absorption spectra were recorded. These spectra are given in Table 3.3 and Figure 3.3.

Table 3.3 *UV-Vis maximum absorption wavelengths λ for AuNSs*

Sample	λ (nm)	Diameter (nm)
AuNS 1	505	3.0 ± 0.5
AuNS 2	522	11.6 ± 1.0
AuNS 3	524	15.8 ± 1.1
AuNS 4	525	17.4 ± 1.5
AuNS 5	527	20.0 ± 1.2
AuNS 6	530	43.0 ± 2.5
AuNS 7	550	80.0 ± 3.0

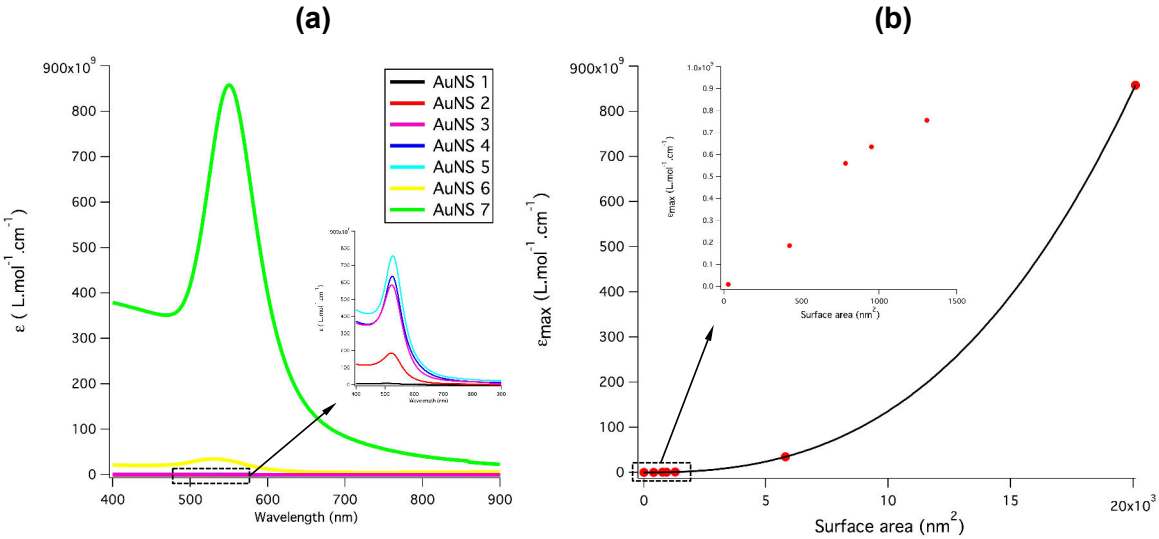

Figure 3.3 *Molar absorptivity (ε) spectra of AuNSs solutions. (a) The insert shows magnified spectra for small nanoparticle's. (b) Plot of ε_{max} (as measured at λ) as a function of the surface area of nanoparticle's. Insert: magnification for small particles.*

It can be easily inferred from the red shift of the position of the peak maxima (from 505 to 550 nm) that the size of AuNSs increases (from 3.0 to 80.0 nm) in Figure 3.3. The role of the surface area is exemplified in Figure 3.3 (b), the molar extinction coefficient at the peak maximum, ε_{max}, displaying a quasi linear dependence with surface area in the case of small particles, with a faster growth rate for the largest ones

❖ **Silver nanospheres**

As UV-Vis spectra have already been used to study the synthesis of AgNSs in solution, we summarize below spectroscopic data for PVA- and PVP-capped nanoparticles using the optimized fabrication conditions in Table 3.4 and Figure 3.4.

Table 3.4 *Silver colloidal solutions: optimized synthesis process*

Sample	PVA (mg)	PVP (mg)	$AgNO_3$ 0.1 M (mL)	$NaBH_4$ 0.1 M (mL)	n_{AgNO_3} / n_{NaBH_4}	Wavelength λ_{max} (nm)	Absorbance
AgPVA	20		0.1	0.2	1/2	395	1.60
AgPVP		30	0.1	0.2	1/2	400	1.75

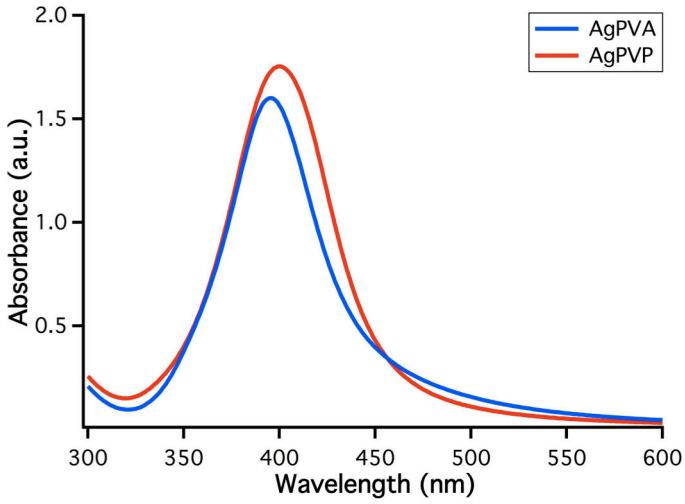

Figure 3.4 *UV-Vis Absorption spectra of AgNSs synthesized in the optimized conditions*

3.3.2. Powdery-AgNSs : samples and XRD spectra

The synthesis of AgNSs, made in two steps as mentioned above, resulted in silver oxalate powder (Figure 3.5) and, after thermal treatment, to the solid-state AgNSs sample (Figure 3.6).

Figure 3.5 *Silver Oxalate sample.*

Figure 3.6 *Powdery-AgNSs sample.*

The XRD pattern confirmed the formation of face-centered-cubic (fcc) Ag nanocrystals at 2θ values of 38.2°, 44.4°, 64.6° and 77.6° representing the (111), (002), (022) and (113) planes of the fcc structure as shown in Figure 3.7. All the peaks are well matched with the standard sample.

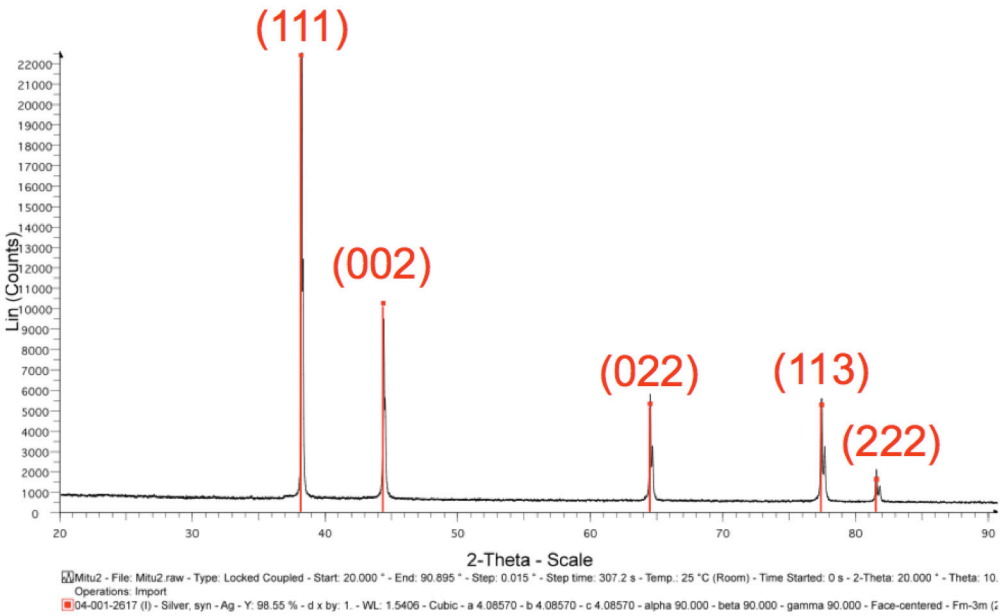

Figure 3.7 *XRD pattern of AgNPs.*

3.3.3. TEM analysis

TEM is the best tool to investigate the morphology and size distribution of nanoscale objects. Samples for TEM were prepared by dropping a metallic NPs colloidal solution onto a carbon-coated Cu grid, followed by slow evaporation of solvent at room temperature.

❖ **Gold nanospheres**

Figure 3.8 shows TEM images of different average diameters (AuNSs), which are consistent with the results of the analysis of UV-Vis (Table 3.3 and Figure 3.3). The particles sizes are obtained by measuring and averaging diameters for about 100 particles.

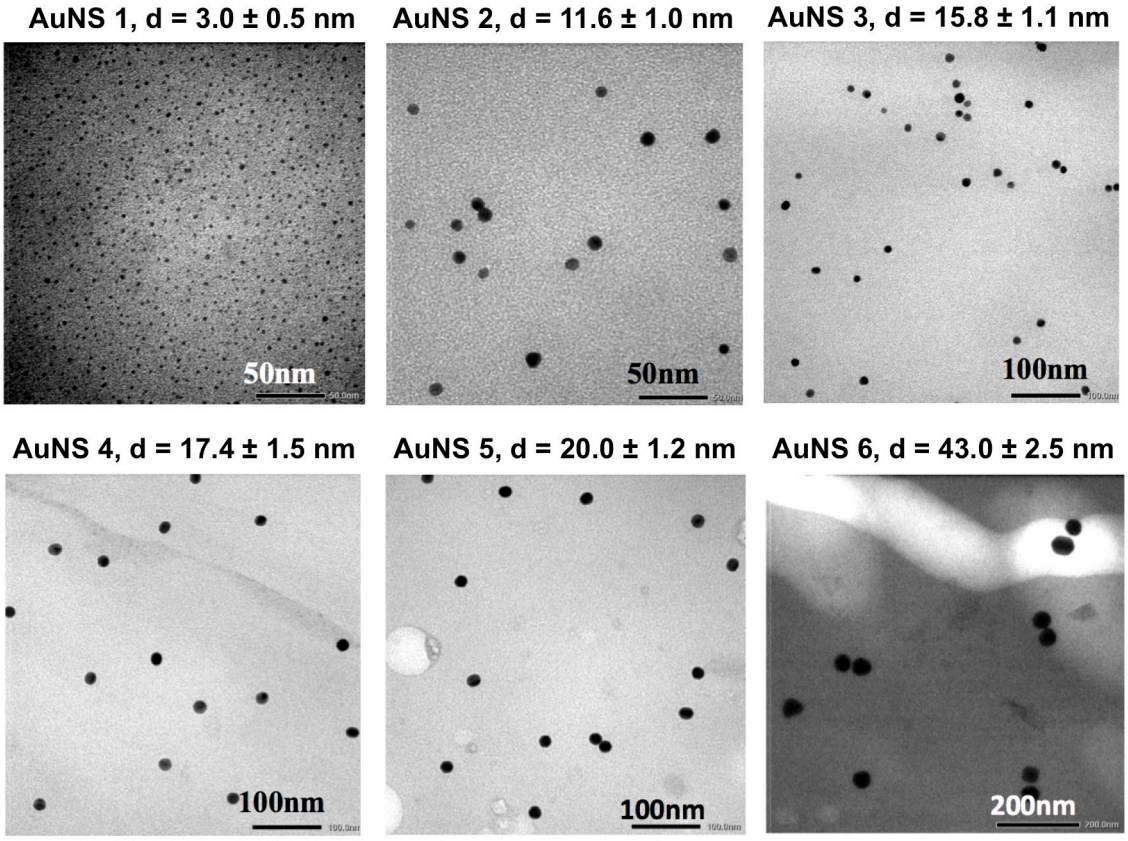

Figure 3.8 *TEM images and average size of AuNSs. d is diameter of nanospheres.*

❖ **Silver nanospheres**

Figure 3.9 shows TEM images of AgNSs with PVA (2.9(a)) and PVP (2.9(b)) capping and of the "dry" powdery AgNSs obtained via thermal decomposition (2.9(c)). The diameter of the particles is obtained by measuring and averaging diameters for about 100 particles.

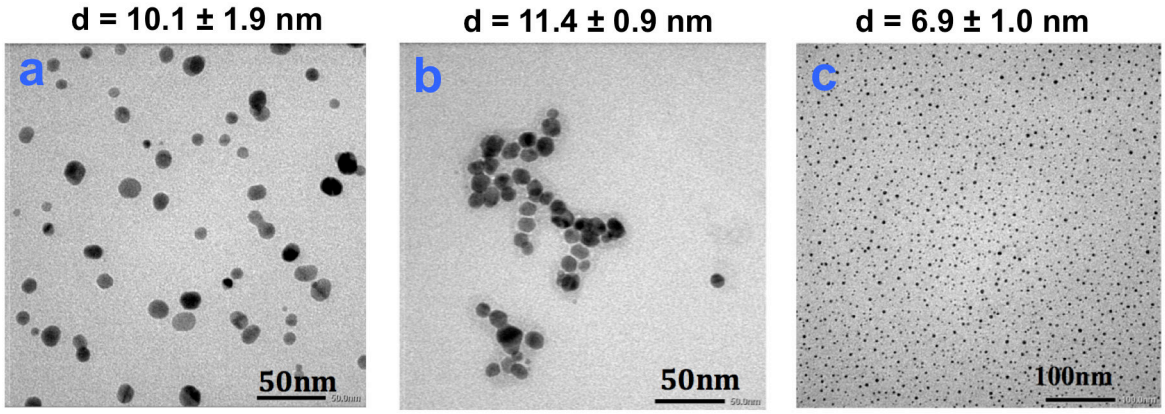

Figure 3.9 *TEM image of AgNSs: (a) AgPVA, (b) AgPVP and (c) Powdery-AgNSs. d is diameter of nanospheres.*

❖ **The stability of AgNSs**

Silver nanoparticles are usually considered as less stable than AuNPs, as they are more sensitive to oxidization by atmospheric oxygen. It is therefore important to verify that the PVA and PVP capping agents chosen in our synthetic approach are liable to stabilize these nano-objects for a long period (weeks or months).

The stability of the silver colloidal solutions can be easily checked using its peak absorbance in the UV-Vis spectrum. Results are shown in Table 3.5.

Table 3.5 *The stability of the silver colloidal solutions*

Sample	Time	Wavelength λ_{max} (nm)	Absorbance
AgPVA	0	**395**	**1.60**
AgPVA	1 week	**396**	**1.59**
AgPVA	2 weeks	**396**	**1.59**
AgPVA	4 weeks	**396**	**1.55**
AgPVA	6 months	**396**	**1.44**
AgPVP	0	**400**	**1.75**
AgPVP	1 week	**400**	**1.67**
AgPVP	2 weeks	**400**	**1.64**
AgPVP	4 weeks	**400**	**1.57**
AgPVP	6 months	**400**	**1.45**

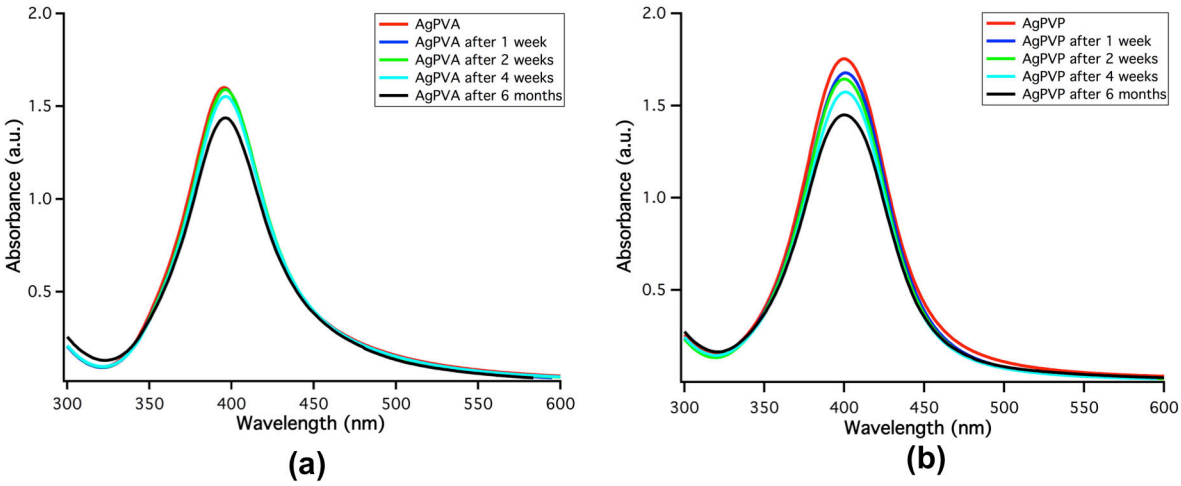

Figure 3.10 *UV-Vis Absorption spectra of synthesized AgNSs after 1, 2, 4 weeks and 6 months (a) AgPVA, (b) AgPVP*

In Figure 3.10, AgNSs (with PVA, (a)) showed more stability in the first 4 weeks compared with AgNSs (with PVP, (b)). After 6 months, the peak intensity decreases from 1.60 to 1.44 (with PVA) and from 1.75 to 1.45 (with PVP) resulting in a decrease of the number of nanoparticle. The constancy of AgNSs size as inferred from unchanged of the position of the peak maxima. This observation is consistent with the TEM analysis of sample AgPVA after 6 months in Figure 3.11.

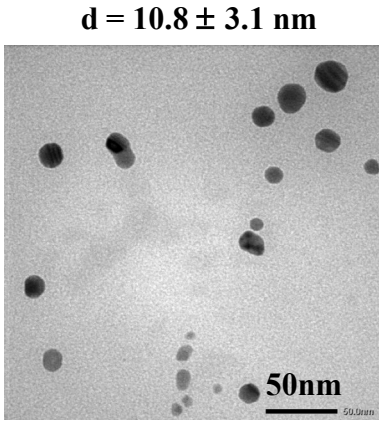

Figure 3.11 *TEM image and size distribution histogram of AgPVA after 6 months*

This systematic investigation of synthesis processes of colloidal AgNSs has therefore resulted in the elaboration of highly stable silver nanoparticles in water solution for several months. This achievement demonstrates that using AgNPs for practical applications is a realistic choice by using adequate synthesis conditions and protective agents.

3.3.4. NLO properties of metal nanospheres

❖ Gold nanospheres

In HLS measurements, different concentrations were used for each kind of particle. As β values are independent on particle concentration, aggregation effects can be ruled-out. As the concentration of the reducing agent used for the reaction was always higher than the minimal reducing agent concentrations required to achieve a total reaction, the reduction of Au^{+III} species to atomic Au^0 is complete, and thereby only gold nanoparticles were formed. This situation is the same for AuNRs synthesized in Chapter 4. The β and β' values are calculated by using eqn (2.7) and (2.8). All values are presented in Table 3.6.

Table 3.6 *The first hyperpolarizability of Au per atom (β') and per particle (β). The relative experimental error on β is ± 15%, mainly due to the uncertainly from HLS measurements in water, the signal/noise ratio for the SHG signal being much lower in this case than for AuNSs solutions.*

Sample	Diameter (nm)	Surface area (nm^2)	Volume (nm^3)	N_{Au} per particle	Particle conc.	β per particle (β) (10^{-26}) esu	β per atom (β') (10^{-30}) esu	β_R (10^{-20}) esu
AuNS 1	3.0 ± 0.5	30	15	800	8.80E-08	0.4	130	1
AuNS 2	11.6 ± 1.0	420	820	48000	3.04E-09	3.4	160	0.56
AuNS 3	15.8 ± 1.1	780	2100	120000	9.06E-10	6.5	190	0.57
AuNS 4	17.4 ± 1.5	950	2800	160000	9.02E-10	8.3	210	0.61
AuNS 5	20.0 ± 1.2	1300	4200	240000	5.94E-10	13	270	0.72
AuNS 6	43.0 ± 2.5	5800	42000	2400000	4.01E-11	58	370	0.69
AuNS 7*	80.0 ± 3.0	20100	270000	16000000	1.28E-12	260	660	0.9

* Purchased from Sigma-Aldrich

The increasing β and β' value for AuNSs (from 0.4 to 260 $\times 10^{-26}$ esu and from 130 to 660 $\times 10^{-30}$ esu, respectively) corresponds to the rise in nanoparticle diameter from 3.0 to 80.0 nm. The β values of AuNSs are consistent with those reported by Galletto *et al.*[13] who published values ranging from 0.6 to 16.6 $\times 10^{-26}$ esu for a particle diameter range of 4.9-22.0 nm, but at the same fundamental wavelength, after corrections of β value of water.

When further comparing our β and β' values to the results obtained by K. Das *et al.*[12] and El Harfouch *et al.*[242] (800 nm, 150 fs; 784 nm, 150 fs; respectively), for particles with the same size (~20 nm), our results (13.0 $\times 10^{-26}$ esu) are significantly higher than the values obtained by these authors (3.8 $\times 10^{-26}$ esu; 2.7 $\times 10^{-26}$ esu; respectively). It must be pointed-out that our HLS measurements are performed in a strongly resonant regime, the second harmonic wavelength at 532 nm being very close to that of the AuNSs plasmon resonance. On the contrary, measurements reported in ref.[12,242], performed around 800 nm, are much less resonant, the second harmonic wavelength at 400 nm being significantly different from that of the gold plasmon resonance, resulting in smaller β values.

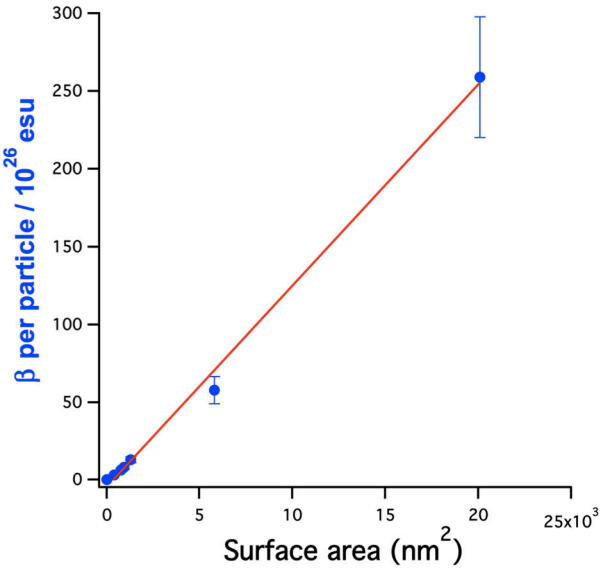

Figure 3.12 *HLS values of the first hyperpolarizability (β) per Au particle in water solution as a function of the surface area of AuNSs. The red line is a least-square linear fit of β with respect to surface area.*

In Figure 3.12, these results emphasize the strong dependence of the first hyperpolarisability of AuNSs on the surface area of nanosphere. A linear dependence of β per particle with respect to the surface area of AuNSs is observed, with a remarkable correlation coefficient (0.996). This confirm that these high β values and their linear increase with particle surface area arise from surface defects of gold nanospheres, leading to centrosymmetry breaking and resulting in a dipolar-type NLO response, as discussed in ref.[243]. In this case, the HLS intensity is expected to scale with the fourth power with particle diameter, as confirmed by our results on Figure 3.12.

It is interesting to go further in hyperpolarizability data analysis by inferring from experimental HLS results a "reduced hyperpolarizability" β_R, which brings corrections from surface effects and plasmonic local field effects at the fundamental and harmonic frequencies. to experimental β values. The β_R expression is valid only in a purely dipolar, local regime, and is defined as follow:[10]

$$\beta_R = \frac{\beta}{k^2 S f(2\omega)\left(f(\omega)\right)^2} \tag{3.1}$$

where β is the hyperpolarizability of the nanoparticle as measured by HLS, k is the wave vector of the fundamental wave, S is the surface area of the nanoparticle, $f(\omega)$ and $f(2\omega)$ are the local field factors at the fundamental (ω) and harmonic (2ω) frequencies. The product k^2S accounts for the expected surface dependence of the quadratic hyperpolarizability in the case of a purely dipolar electric response of metallic nanoparticles. In the case of spherical nanoparticles, we can use a simple expression of these local field factors:

$$f(\omega, 2\omega) = \left|\varepsilon(\omega, 2\omega) + 2\varepsilon_s\right|^{-1} \tag{3.2}$$

where ε and ε_s are the dielectric constants of the metal and of the solvent (water), respectively. This expression is valid for particles having a small diameter as compared to the incident wavelength. We have checked that for even 80 nm nanospheres, the non-dipolar contribution to the local field factors remains negligible, according to Equations (1) and (2) of ref.[243]. Dielectric constant values of gold nanoparticles are assimilated to the values of bulk gold, an assumption which is expected to be valid for particle diameters higher than 2 nm. These ε values are inferred from the data table published by Johnson and Christy[244]. Calculated β_R

values are reported in Table 3.6. These data illustrate the limit of our approximations at the two extreme values of the diameter range. Whereas β_R remains almost constant (considering the relative experimental errors on β values, around ±10%) for most nanospheres (NS2 to NS6), for the smallest value (3 nm), β_R is significantly larger. This depart for the average β_R values is most probably related to the fact that for very small particles, taking bulk values for AuNP dielectric constants is not more valid (reduced electronic conductivity for nano-objects with a small number of metal atoms). On the other extremity, the increased β_R value can reflect the emergence of non-dipolar effects in larger AuNSs.

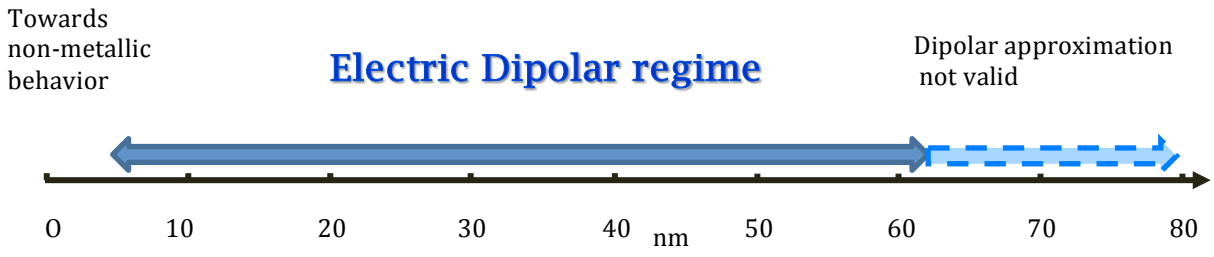

Figure 3.13 *Representation of the validity domain of the electric dipolar regime for the quadratic NLO properties of AuNSs at 1.06 µm.*

Figure 3.13 summarizes the limit of validity of the electric dipolar regime of the β values of spherical gold at 1.06 µm. This validity domain can change for other values of the fundamental wavelength.

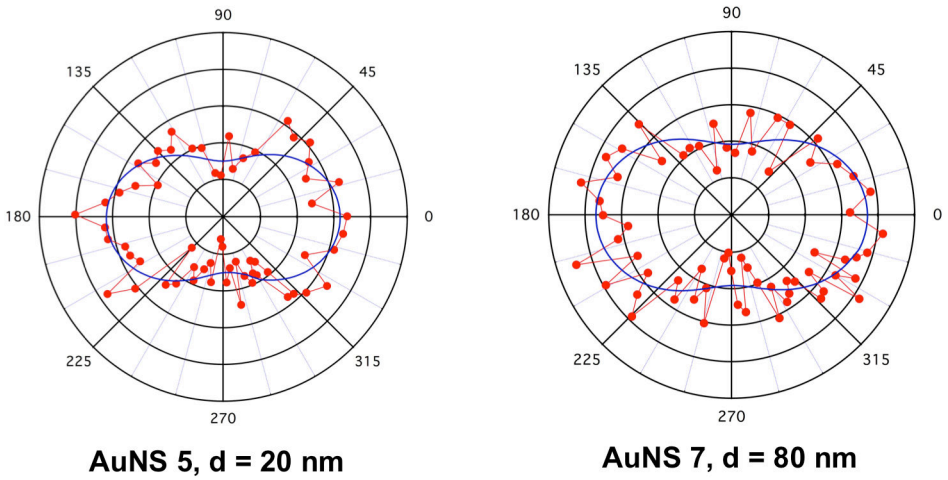

Figure 3.14 *Polar plot of the polarization resolved HRS intensity as a function of the input polarization recorded for AuNSs with different diameters at 1064 nm.*

However, the pattern of the polar plot for a vertical polarization analysis at 2ω for AuNSs with 20 nm and 80 nm diameters (Figure 3.14) is the signature of an electric dipolar response, confirming that the HLS signal from the small metallic nanoparticles is of pure electric dipole origin.

❖ **Silver nanospheres**

Freshly prepared solutions of AgNSs were characterized by HLS at 1064 nm for the determination of their first order hyperpolarizability, on the basis of a known β value of the water used as a reference. All values are presented in Table 3.7.

The size of AgNSs being almost unchanged, the β' value of Ag atom for AgNSs with PVA (89×10^{-30} esu) is found to be the same as for AgNSs with PVP (85×10^{-30} esu). It means that the nature of the protective agents (PVA, PVP) does not affect the first hyperpolarizability (β') in AgNSs.

Both of these β' values at 1064 nm are smaller than the value obtained [5600 ($\pm$1100) $\times$ 10^{-30} esu] for polymer stabilized 20 nm AgNSs in aqueous solution by Johnson *et al.*[23] at 820 nm using 80 fs pulses. This strong difference can be explained by several factors. First, β_{H_2O} value used in our experiments is 0.055×10^{-30} esu while β_{H_2O} used by Johnson *et al.* is 0.56×10^{-30} esu. As a consequence, β' values reported by Johnson should be renormalized according to our work β_{H_2O} value, resulting in $\beta' = 560 \times 10^{-30}$ esu. Second, HLS measurements made by Johnson are performed in a strongly two-photon resonant regime, the second harmonic wavelength at 410 nm being identical to that of the AgNSs plasmon resonance. On the contrary, our measurements, performed at 1064 nm, are much less resonant, the SH wavelength at 532 nm being significantly different from that of the silver plasmon resonance, resulting in smaller β values.

Table 3.7 *The first hyperpolarizability (β) of Ag per atom and per particle. The relative experimental error on β is ± 15%, mainly due to the uncertainly from HLS measurements in water, the signal/noise ratio for the SHG signal being much lower in this case than for AgNSs solutions.*

Sample	Diameter (nm)	Volume (nm^3)	N_{Ag} per particle	Particle Concentration ($M.L^{-1}$)	β per particle (β) (10^{-26}) esu	β per Ag atom (β') (10^{-30}) esu
AgPVA	10.1	540	31000	4.0E-9	1.6	89
AgPVP	11.4	780	45000	2.8E-9	1.8	85

When further comparing our β values (nanoparticle size of 10 nm) to the results obtained by El. Harfouch *et al.*[242] at 784 nm with 180 fs pulses (Table 3.8), in particles with the same size, our β_{10nm} value (with PVA, 1.6 x 10^{-26} esu) is slightly greater than El. Harfouch's β_{10nm} value (citrate capped AgNSs, 1.0 x 10^{-25} esu) after normalization with $\beta_{H_2O} = 0.055 \times 10^{-30} esu$.

But in comparably, we have shown that the first hyperpolarizability of a metal nanoparticle depends on many factors, e.g., size of the particle, dielectric constant of the solvent, and particularly the wavelength of the incident light, which is of great importance due to resonance effect.

Table 3.8 *Comparison between the previously observed β values of Ag per particle/atom and our AgNSs sample, normalized using* $\beta_{H_2O} = 0.055 \times 10^{-30} esu$ *as reference.*

Sample	Laser	Diameter (nm)	β_{H_2O}	β per particle (β) (10^{-26}) esu	β per atom (β') (10^{-30}) esu
Ag [Our sample] Nanospheres	1064nm; 9ns; 10Hz	10.1	0.055×10^{-30}	1.6	89
Ag[23] Nanospheres	820nm; 80fs; 82MHz	20	0.055×10^{-30}	27.7	560
Ag[242] Nanospheres	784nm; 180fs; 76MHz	10	0.055×10^{-30}	1.0	57

❖ **Powdery-AgNSs**

The effective second-order susceptibility d_{eff} at 1064 nm has been evaluated by a Kurtz and Perry SHG powder test, KDP being used as a reference. From this study we show for the first time that powdery-AgNSs are excellent nonlinear scatterers ($d_{eff}^{AgNPs} = 0.28 pmV^{-1}$, close to that of KDP), not only in solution as demonstrated from HLS experiments, but also in the solid state, as evidenced by the clearly visible green light emitted when powdery-AgNSs are irradiated at 1064 nm (see Figure 3.15). In view of the small size of powdery-AgNSs, the second harmonic signal is dominated by an electric dipole contribution arising from small deviations of the particle shape from that of a perfect sphere.

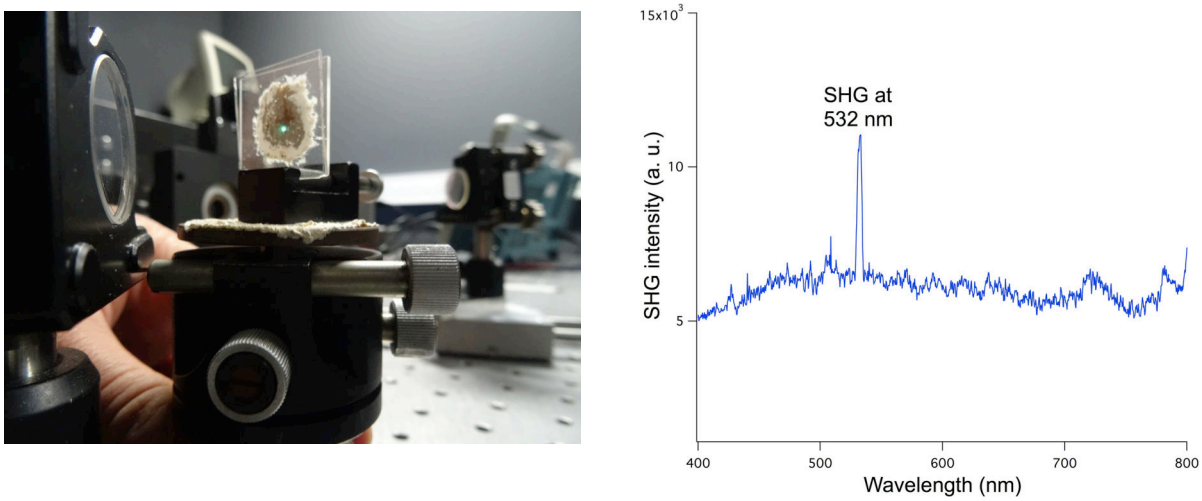

Figure 3.15 *(left) Visible second harmonic emission from powdery-AgNSs irradiated at 1064 nm. (right) Spectrum of light emission from AgNSs powder illuminated by a pulsed laser emitting at 1064 nm.*

The visible signal emitted by powdery-AgNSs is made of 2 contributions: a broadband background corresponding to the luminescence signal frequently emitted by metallic targets under laser illumination, and a very narrow peak at 532 nm, confirming the presence of a SHG signal from powdery-AgNSs.

3.4. Conclusion

We have achieved the synthesis and characterization of metallic Au and Ag nanospheres with different diameters, various protective agents and different reduction and growth methods such as the seed-mediated technique. We demonstrated that the first hyperpolarizability (β) linearly depends on the surface area of AuNSs. The calculation of a "reduced" β_R value taking into account local field factors and surface effects showed a remarkable constant value for most AuNSs, confirming the electric dipolar NLO response, and slightly departing from this behaviour for very small and large particles as expected from the theory. Comparison of hyperpolarizability values of Au and Ag NS is consistent with the data from the literature, and evidence better NLO performances of AuNSs over those of AgNSs at 1.06 μm due to strong plasmon resonance effects for gold NPs at this wavelength.

AgNSs powder has been successfully prepared by using thermal decomposition method. The XRD pattern confirmed the formation of face-centered-cubic Ag nanocrystals, the size of the particles being around 6.9 nm. The AgNSs powder shows a surprisingly strong quadratic NLO response, close to that of KDP. Silver colloidal solutions have been successfully prepared by using a reducing agent. The UV-Vis spectra of AgNSs in aqueous solution showed specific absorption peaks. AgNSs display exceptionally strong β values, which are independent on the nature of the protective agent (PVA, PVP).

Chapter 4
Nonlinear optical properties of metallic nanorods

4.1. Introduction

Gold nanorods exhibit unique and tunable localized surface plasmon resonance (LSPR) derived optical properties in the ultraviolet-visible-near infrared (UV-Vis-NIR) region. The high stability, low biological toxicity, bright color, and versatility of gold nanorods have inspired an explosion of research interest in their properties and applications (which include roles in catalysis, data storage, and biomedicine). However, the absorption spectra of such particles belongs mainly to the near-infrared (NIR) range. Replacing gold by silver for nanorods fabrication and applications may offer wider possibilities in terms of spectral coverage in the red- NIR domain.

However, the exploration of nonlinear optical (NLO) properties of metallic nanorods has been limited to gold nanoparticles, and has been mainly focused on hyperpolarizability measurements of a limited choice of samples. A more systematic investigation has been conducted on the influence of gold nanorod aspect ratio of their β properties,[9] but this study was limited to nanoparticles with similar surface areas.

In Chapter 3, the evidence of a strong influence of surface area of the β values of spherical nanoparticles urges us to investigate this effect also in the case of metallic nanorods. If we want to investigate nanorods exhibiting non only different aspect ratios (ARs), but also

various surface areas, we should be able to determine which effect, aspect ratio or surface area, dominates their quadratic nonlinear behaviour.

For these reasons, we will explore in this Chapter the NLO properties of gold and silver nanorods (AuNRs and AgNRs, for the first time for AgNRs), and perform a systematic investigation of surface area effects on their β values. The comparison of NLO properties of AuNRs and AgNRs is also of great interest in order to qualify AgNRs as suitable labels, alternative to AuNRs, for chemical and biological applications.

Colloidal solutions of AuNRs and AgNRs with different aspect ratios have been synthesized (1.47; 1.63 and 2.30 for gold, 5.0; 6.3; 7.5; 8.2 and 9.7 for silver). The first hyperpolarizability β values of these metallic NRs have been measured by HLS at 1064 nm. Moreover, by studying AuNRs with different surface areas, we will evidence the predominance of these surface effects over shape factors, leading us to revisit previous studies on the NLO properties of these nanorods.[9]

4.2. Synthesis of metallic nanorods

❖ **Gold nanorods**

0.1 mL $HAuCl_4$ 0.029 M and 0.075 mL $AgNO_3$ 0.01 M were added to a 10 mL aqueous solution of CTAB 0.025 M, the growth solution changed to bright yellow. Then, 0.055 mL ascorbic acid 0.1M was added and the growth solution became colorless. At that time, 12 µl (0.5 h, 1 h) and 24 µl (1 h) of the seed solution (as mentioned in the Chapter 3) were added quickly to the growth solution. The colour of growth solution immediately changed from white to dark blue. The solution contained respectively 1.47; 1.63 and 2.30 AR nanorods.

❖ **Silver nanorods**

Silver nitrate ($AgNO_3$, 99%), sodium borohydride ($NaBH_4$, 99.99%), tri-sodium citrate (TSC, $C_6H_5Na_3O_7.2H_2O$), polyvinylpyrrolidone (PVP; 40 000 g mol^{-1}) and hydrogen peroxide (H_2O_2, 30 wt%) are purchased from Sigma-Aldrich. The solutions were prepared using ultra-pure water from a Millipore system (18 MΩ cm^{-1}) throughout the experiment. All aqueous samples are at natural pH = 7.

AgNRs were prepared by a one-pot seedless growth method. In the typical synthesis, a 20 mL volume of an aqueous solution containing 1.0×10^{-4} M PVP and 5×10^{-3} M TSC was prepared in a 20 mL flask. To this solution, different volumes of $AgNO_3$ 0.032 M and 60 µL H_2O_2 were added under stirring. Immediately, aqueous $NaBH_4$ (0.15 mL, 0.1M) was rapidly added while the solution was stirred vigorously. The colourless solution changed into yellowish instantly. When further stirring for 20 minutes, the yellowish solution turned to violet-red, violet, blue-violet and blue. The growth process can be completed within ~40 min. Depending on the volumes of $AgNO_3$ (2.0; 1.75; 1.5; 1.25 and 1.0 mL), the obtained AgNRs show different average values of aspect ratios (5.0; 6.3; 7.5; 8.2 and 9.7, respectively). The volumes of $AgNO_3$ decrease when the concentration of TSC is unchanged. It means that n_{TSC} / n_{AgNO_3} increases. This is the cause for the increased value of ARs as clearly explained in ref.[245].

Contrary to elaboration methods of gold nanorods where ARs are controlled by the presence of silver ions, no external compound is required to monitor the AgNRs AR, which appears to be controlled only by the concentration in Ag^+ ions in the reaction medium.

The concentration of the reducing agent used for the reaction was always higher than the minimal reducing agent concentrations required to achieve a total reaction. It means that reduction of Ag species to atomic Ag^0 is complete, and thereby only AgNRs were formed.

4.3. Characterization on nanorods

4.3.1. UV-Vis spectra

It has been known that the number, spectral range, and intensity of NMNPs LSPR peaks strongly depend on various factors, such as particle size and shape, aggregate morphology, ligand, dielectric property and refractive index of the surrounding medium.[142] In the case of nanorods, while the transverse band is almost insensitive to nanorod morphology, the position of the longitudinal band highly depends on the aspect ratio (AR, *i.e.* length divided by width) of the nanorods and can be shifted towards the near-infrared region and beyond with increasing AR: the higher the AR, the higher the longitudinal LSPR wavelength.[80,129]

In order to optically characterize the AuNRs and AgNRs solutions, their UV−Vis absorption spectra were recorded. These spectra are given in Table 4.1 and Figure 4.1 for AuNRs.

Table 4.1 *UV-Vis maximum absorption wavelengths λ_1 and λ_2 of the AuNRs solutions. L is the length and W the diameter of the rods.*

Sample	λ_1 (nm)	λ_2 (nm)	Length (nm)	Width (nm)	Aspect ratio (length/width)
AuNR 1	549	634	20.6 ± 2.1	14.0 ± 1.3	1.47 ± 0.34
AuNR 2	543	637	20.4 ± 2.5	12.5 ± 1.2	1.63 ± 0.36
AuNR 3	539	639	20.4 ± 2.0	8.9 ± 0.9	2.30 ± 0.46

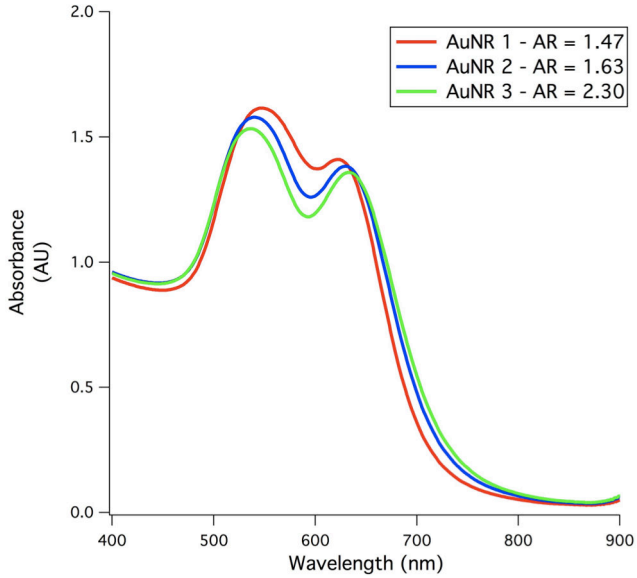

Figure 4.1 *UV-Vis absorption spectra of the AuNRs solutions.*

The expected two distinct LSPR are clearly observed from 1: one (λ_1) is associated with a transverse LSPR mode and the other one (λ_2) associated with a longitudinal LSPR mode. While the transverse band is insensitive to the size of the nanorods, the longitudinal band is significantly red shifted when increasing the aspect ratio AR.[9,230,231]

For silver nanorods, spectral data are displayed on Table 4.2 and Figure 4.2 below:

Table 4.2 *UV-Vis maximum absorption wavelength λ_1 and λ_2 of the AgNRs solutions.*

Sample	λ_1 (nm)	λ_2 (nm)	Length (nm)	Width (nm)	Aspect ratio (length/width)
AgNR 1	423	545	20.1 ± 3.0	4.0 ± 0.9	5.0 ± 1.9
AgNR 2	439	585	25.7 ± 4.9	4.1 ± 0.5	6.3 ± 2.0
AgNR 3	442	614	31.4 ± 6.5	4.2 ± 0.7	7.5 ± 2.8
AgNR 4	452	675	36.0 ± 4.4	4.4 ± 0.8	8.2 ± 2.5
AgNR 5	458	716	49.6 ± 8.7	5.1 ± 1.0	9.7 ± 3.6

As expected, the UV-visible spectra of each nanorod solution exhibit two absorption bands of different intensity, corresponding to the longitudinal and transversal localized surface plasmon resonance (LSPR) modes, named as "longitudinal band" (λ_1) and "transverse band" (λ_2). This red shift of the position of the longitudinal band (from 545 to 716 nm) is clearly observed when increasing the AR of AgNRs (from 5.0 to 9.7) in Figure 4.2.

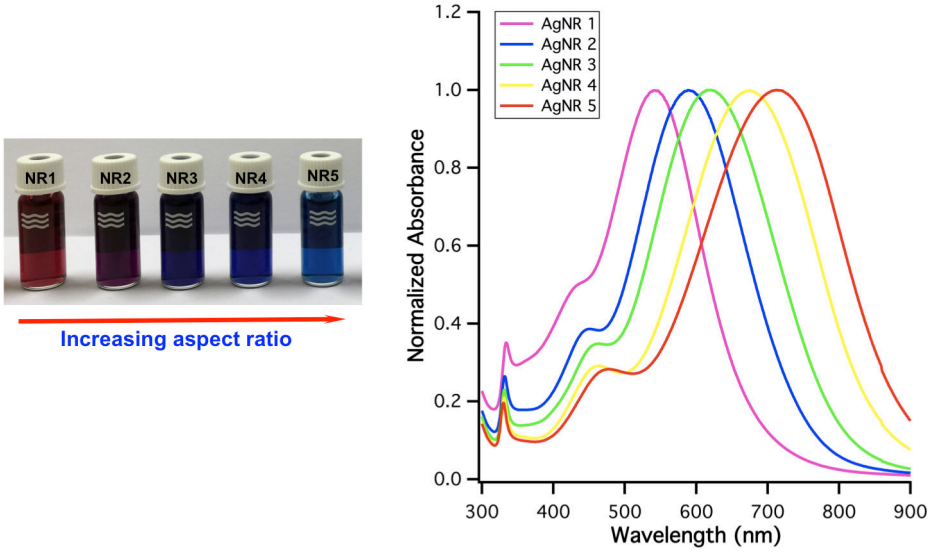

Figure 4.2 *UV-Vis absorption spectra of AgNRs solutions with various ARs (right). The average ARs are 5.0 ± 1.9; 6.3 ± 2.0; 7.5 ± 2.8; 8.2 ± 2.5 and 9.7 ± 3.6 for (AgNR1-AgNR5), respectively. The photograph shows aqueous solutions containing AgNRs (left) with increasing AR.*

4.3.2. TEM analysis

Figure 4.3 shows TEM images of different AR (AuNRs), which are consistent with the results of the analysis of UV-Vis reported in Table 4.1 and Figure 4.1. The average particles sizes are obtained by measuring and averaging diameters for about 100 particles.

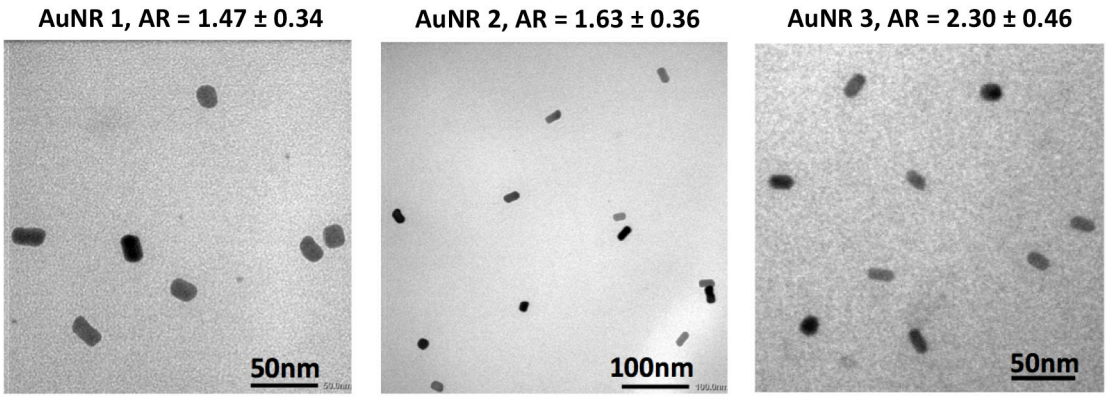

Figure 4.3 *TEM images of AuNRs with different ARs.*

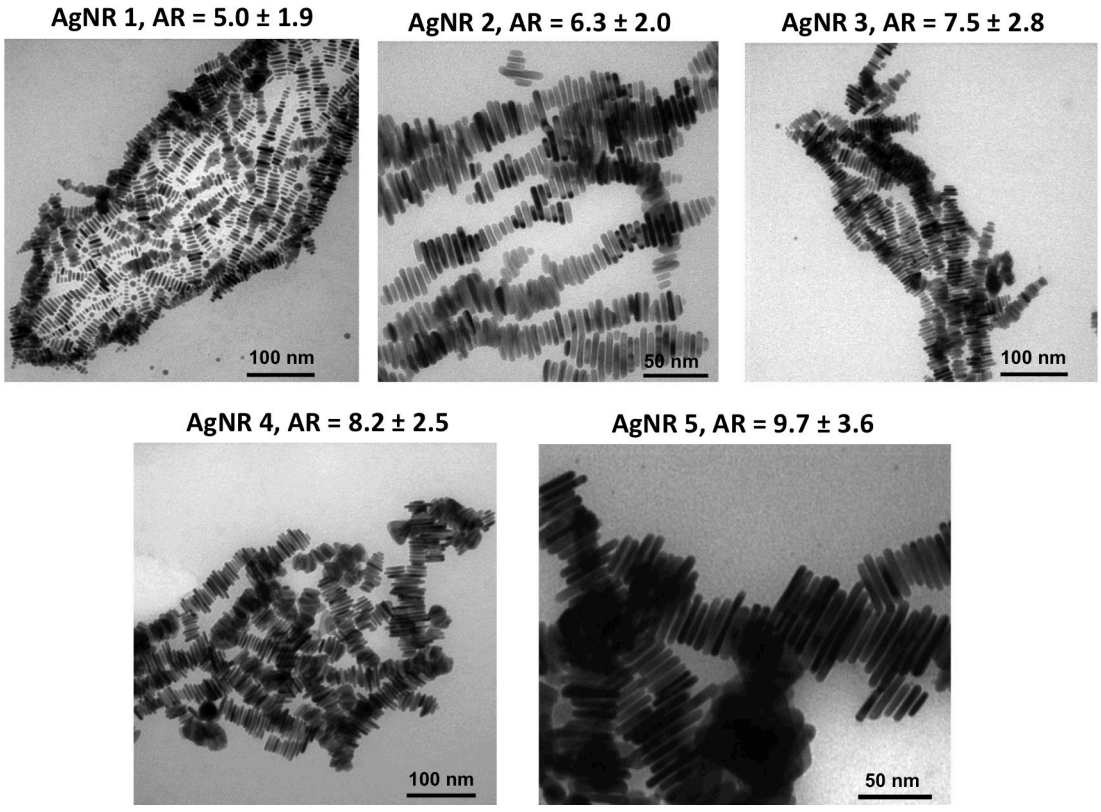

Figure 4.4 *Representative TEM images of AgNRs with variable AR.*

For AgNRs, it should be noted that the TEM image is obtained directly from the original product. No size selection or any other purification process has been applied. Figure 4.4 shows TEM images of AgNRs obtained from a one-pot seedless growth process and indicates the average AR of nanorods obtained by measuring and averaging dimensions for about 100 particles. TEM characterization confirms that the morphological yield of AgNRs is high, which is in good agreement with UV-Vis spectrum.

4.3.3. NLO properties of metallic nanorods

❖ Gold nanorods

The increasing β and β' value for AuNSs (from 0.4 to 260 $\times$ 10^{-26} esu and from 130 to 660 $\times$ 10^{-30} esu, respectively) corresponds to the rise in nanoparticle diameter from 3.0 to 80.0 nm. The β values of AuNSs are consistent with those reported by Galletto *et al.*[13] who published values ranging from 0.6 to 16.6 $\times$ 10^{-26} esu for a particle diameter range of 4.9-22.0 nm, but at the same fundamental wavelength, after corrections of β value of water (see in Chapter 3). For AuNRs, the β and β' values are calculated by using eqn (2.7) and (2.8). All values are presented in Table 4.3.

Table 4.3 *The first hyperpolarizability of Au per atom (β') and per particle (β) for AuNRs. L is the length and W the diameter of the rods. The relative experimental error on β is ± 15%, mainly due to the uncertainly from HLS measurements in water.*

Sample	Diameter (nm)	Surface area (nm^2)	Volume (nm^3)	N_{Au} per particle	Particle conc.	β per particle (β) (10^{-26}) esu	β per atom (β') (10^{-30}) esu
AuNS 5	20.0 ± 1.2 / AR = 1.0	1300	4200	240000	5.94E-10	13	270
AuNR 1	20.6 ± 2.1 (L) - 14.0 ± 1.3 (W) AR = 1.47 ± 0.34	1200	3200	190000	3.11E-09	6.6	150
AuNR 2	20.4 ± 2.5 (L) - 12.5 ± 1.2 (W) AR = 1.63 ± 0.36	1050	2500	150000	1.99E-09	4.7	120
AuNR 3	20.4 ± 2.0 (L) - 8.9 ± 0.9 (W) AR = 2.30 ± 0.46	700	1300	73000	3.96E-09	2.9	110

* Purchased from Sigma-Aldrich

A significant increase of β per atom and particle with the increase in the AR of AuNRs has been previously reported.[9] This result was obtained only when AuNRs displayed the same volume and surface. Here, we report an opposite behavior, β decreasing when increasing AR.

In this work, the length (~20 nm) of AuNRs is kept constant, whereas the radius decreases when increasing AR (see Figure 4.3). When AR increases from 1.0 to 2.3, a significant decrease of β (from 13.0 to 2.9 × 10^{-26} esu) and β' values (from 270 to 110 × 10^{-30} esu) is observed. However, in our work, the AuNR surface strongly decreases when increasing AR's. Therefore, the role of the AuNR surface overcomes the influence of AR observed in ref.[9] for particles having the same surface only.

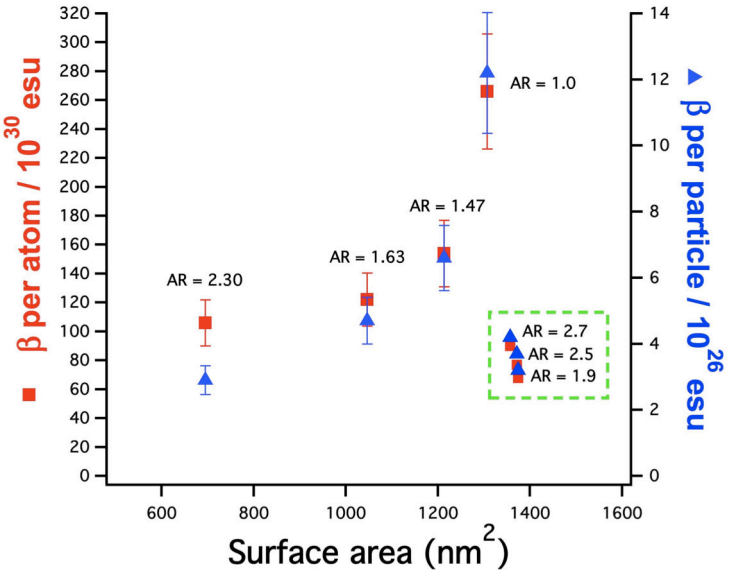

Figure 4.5 *HLS values of the first hyperpolarizability (β) per Au atom (red squares) and per Au particle (blue triangles) in water solution as a function of the surface area of AuNRs. For comparison, data on AuNRs reported in ref.*[9] *are presented in the dotted border rectangle.*

A confirmation of this hypothesis can be found by comparing, for the same variation ΔAR of AR, the hyperpolarizability changes $\Delta\beta$' found in this work to those obtained by Anu Singh *et al.*[9]. For ΔAR = 0.8, the change in β' ($\Delta\beta' = -48 \times 10^{-30}$ esu) is significantly higher (and of an opposite sign) than the values obtained in ref.[9] ($\Delta\beta' = +22 \times 10^{-30}$ esu). Ref.[9] results are obtained when the AuNRs have the same surface area while the surface of our AuNRs strongly changes.

In addition in the present work, for almost the same variation of surface area ΔS for AuNRs (ΔS = 500 nm^2 between AuNR1 and AuNR3) and AuNSs (ΔS = 530 nm^2 between NS4 and NS2), $\Delta\beta' = 50 \times 10^{-30}$ esu observed for AuNSs is comparable to $\Delta\beta' = 40 \times 10^{-30}$

esu observed for AuNRs. This change is much higher that the increase of $\Delta\beta'$ (+ 22 × 10^{-30} esu) reported in ref.[9] for NR having the same surface. This result confirms the major influence of surface area on the value of the first hyperpolarizability of nanoparticles, which dominates the contribution of ΔAR.

The pattern of the polar plot for a vertical polarization analysis at 2ω corresponds to the expected response of an electric dipole, confirming that the HLS signal from the small metallic nanoparticles is of pure electric dipole origin. There were no clear differences between different ARs values (see in Figure 4.6).

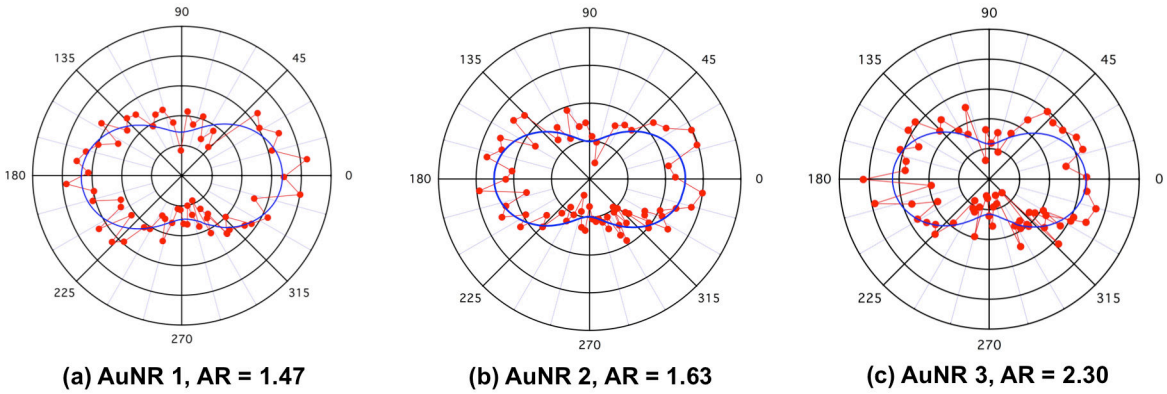

Figure 4.6 *Polar plot of the polarization resolved HRS intensity as a function of the input polarization recorded for AuNRs with different ARs at 1064 nm.*

❖ Silver nanorods

The β and β' values of AgNRs are presented in Table 4.4. Figure 4.7 shows the dependence of nanoparticle β values with nanoparticle surface area, the continuous black line resulting from a linear fit with a remarkable correlation coefficient of 0.999 for β per Ag nanoparticle, for AgNRs only. The dashed violet line includes two AgNSs in the linear fit, resulting in a correlation coefficient of 0.997 for β per Ag nanoparticle, encompassing AgNRs and two AgNSs. This latter correlation coefficient remains very close to that obtained with NRs only. Figure 4.7 confirms the high NLO performances of AgNRs for different surface areas and emphasizes the strictly linear dependence of the first hyperpolarisability β of silver particles

on the surface area of nanorods, indicating a local, dipolar-type response arising from surface effects, as proposed for gold nanospheres and nanorods.[15]

Table 4.4 *The first hyperpolarizability of Ag per atom (β') and per particle (β). The relative experimental error on β is ± 15%, mainly due to the uncertainly from HLS measurements in water, the signal/noise ratio for the SHG signal being much lower in this case than for AgNR solutions.*

Sample	AR (length/width)	Volume (nm^3)	N_{Ag} per particle ($\times 10^3$)	Particle conc.	β per particle (β) ($\times 10^{-26}$) esu	β per atom (β') ($\times 10^{-30}$) esu	Surface area (nm^2)
AgNR 1	5.0 ± 1.9	250	15	2.14E-08	1.4	116	280
AgNR 2	6.3 ± 2.0	340	20	1.39E-08	1.9	136	360
AgNR 3	7.5 ± 2.8	440	26	9.32E-09	2.4	150	440
AgNR 4	8.2 ± 2.5	550	32	6.18E-09	2.8	158	530
AgNR 5	9.7 ± 3.6	1010	60	2.67E-09	4.5	182	840

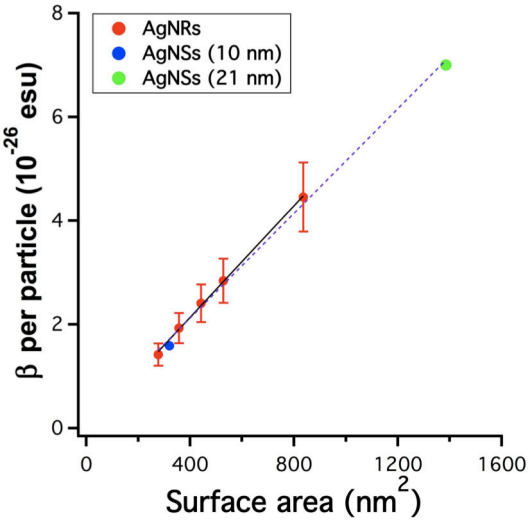

Figure 4.7 *HLS values of the first hyperpolarizability (β) per Ag particle (red disks) in water solution as a function of the surface area of AgNRs. For comparison, HLS values of the first hyperpolarizability (β) of silver nanospheres (AgNSs, blue and green disk for a particle diameter of ~10 nm*[18] *and ~21 nm*[246]*, respectively) in water solution are included.*

In Figure 4.7, the surface area dependence of AgNRs β values are consistent with those of Ag nanospheres (AgNSs) reported in our previous chapter[18] and by Clays *et al.*[246] who published values of 1.6 and 7.0×10^{-26} esu for particle diameters of ~10 nm and ~21 nm, respectively, at the same fundamental wavelength, after corrections of β_{H_2O} value (0.055 instead of 0.56×10^{-30} esu).

When further comparing our β values of AgNRs to the results obtained for gold nanorods (AuNRs)[19], for particles with similar surface areas, those of AgNRs (from 2.8 to 7.0×10^{-26} esu with surface areas ranging from 530 to 1390 nm^2) are nearly equal to those of AuNRs (from 2.9 to 6.6×10^{-26} esu with surface areas ranging from 700 to 1200 nm^2).

As already mentioned, Anu Singh *et al.*[9] pointed out a significant increase of β per atom and particle with the increase in the AR of AuNRs with the same surface area. However, in present work, it is observed, as for AuNRs, that surface area is the dominant parameter in the evolution of β and β' of metallic nanorods (including AR=1).

4.3.4. Nanorod stability

Most potential medical applications of nanorods require particle and suspension stability over a few days or a few weeks. Particle stability refers to maintaining the plasmonic properties of the particles until they are used. This, for metallic NRs, requires to maintain their shape, avoiding the evolution toward lower aspect ratio geometries.

As nanospheres have the smallest surface area per unit volume of any geometry, they provide an efficient way to minimize their surface free energy. For this reason, metallic nanorods can display poor stability in solution, and tend to reorganize towards spherical geometries.[247] Therefore, it is important to check nanorod stability in water solutions in order to validate their use for practical applications, for example in medicine. In the above-quoted reference, nanorods are more stable when capped with polymeric chains rather than with tension-active molecules.

For this reason, we have tested the stability of the silver colloidal solutions can be easily checked by recording their UV-Vis spectra. Results are shown in Figure 4.8.

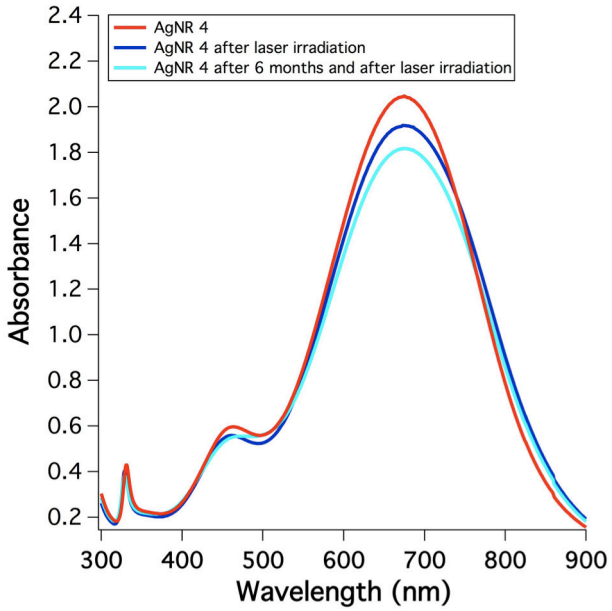

Figure 4.8 *UV-Vis absorption spectra of AgNR 4. Red: spectrum recorded just after AgNR synthesis. Dark blue: spectrum recorded after nanosecond laser irradiation at 1.06 µm (10 minutes) a few days after synthesis. Pale blue: spectrum of the same (laser irradiated) sample recorded after a 6 months storage.*

In Figure 4.8, the maximal peak intensity decreases of 6% and 11% after irradiation with the laser and a further 6 months storage, respectively. The position of λ_1 and λ_2 is almost unchanged only the absorbance is slightly modified. It means that silver colloidal solutions are relatively stable in shape and size, probably due to PVP protection.

4.4. Conclusion

We have achieved the synthesis and characterization of AuNRs and AgNRs with different AR, which were controlled by varying the protective agent, the reductive agent, by using the seed-mediated method and by using a rapid one-pot seedless growth method. Metallic nanoparticles display exceptionally strong β values, for the first time in the case of AgNRs. We demonstrated that the first hyperpolarizability (β) linearly depends on the surface area of metal nanorods, both for AuNRs and AgNRs. This surface effect dominates over the effect of

aspect ratio which has been explored before[9] for a set of AuNRs with similar surface areas. Last but not least, the polymer capping chose for AgNR synthesis results in a good stability of these particles over several months, then confirming their potential to be used for biological applications.

Chapter 5
High second-order nonlinear response of platinum nanoflowers: the role of surface corrugation

5.1. Introduction

Platinum nanoparticle-(PtNPs)-based catalysts are vital to fuel cells, sensors, petroleum and automotive industries, and to optoelectronic and biophotonic devices, due to their high catalytic activity and stability.[105–122] As for other metallic nano-objects, their optical properties exhibit a strong dependence on the nanoparticle morphology. Many investigations have been focused on controlling the shape and size of PtNPs.[210,248–254] Up to now, no significant β values of PtNPs have been reported yet. The plasmon resonance of Pt being located in the UV range ($\lambda \leq 200$ nm), authors did not evidence significant β values in PtNPs during their investigations by HLS measurements of various metallic nanoparticles.[23]

In this chapter, platinum nanoflowers (PtNFs) were elaborated using the seed-mediated growth technique applied to monodisperse platinum nanoparticles (~3.0 nm) synthesized by the chemical reduction method. The X-ray diffraction pattern confirmed the formation of face-centered-cubic platinum nanocrystals. We report the HLS properties of PtNFs for six different diameters (~7.0; 8.0; 10.0; 14.0; 20.0 and 31.0 nm). From these HLS data we infer, for the first time, the evidence of a strong quadratic nonlinear response for PtNFs. These very high hyperpolarizability β values of PtNFs are assigned mainly to highly corrugated surfaces for nanoparticles with irregular shapes.

5.2. Materials and methods

5.2.1. Materials

Hexachloroplatinic acid ($H_2PtCl_6.6H_2O$), ascorbic acid ($C_6H_8O_6$) and tri-sodium citrate (TSC, $C_6H_5Na_3O_7.2H_2O$) were purchased from Sigma-Aldrich. The solutions were prepared using ultra-pure water from a Millipore system (18 MΩ cm-1) throughout the experiment. All aqueous samples are at a neutral pH = 7.

5.2.2. Synthesis of PtNFs

Principle. Pt nanoparticle synthesis is based on the standard reactions.

$$PtCl_6^{2-} + 2C_6H_8O_6 \xrightarrow{100^{\circ}C} Pt + 6Cl^- + 2C_6H_6O_6 + 4H^+$$

(reduction by ascorbic acid)

Preparation of 3.0 nm seed. The first step consists in the preparation of platinum spherical nanoparticle seeds. This preparation was performed starting from a 20 mL aqueous solution of TSC 5×10^{-3} M. Then, 0.2 mL of H_2PtCl_6 0.019 M was added under stirring. After that, 0.1 mL of 0.1 M ascorbic acid was then slowly added and heated to 100 °C. The colour of solution changed to pale brown. Vigorous stirring of the seed solution was continued for 1 h at 25 °C before being used. The average particle diameter was 3.0 nm. This solution was then used as the seeding solution for the growth of PtNFs.

Preparation of 7.0; 8.0; 10.0; 14.0 and 20.0 nm PtNFs. In the second step, 20 mL of growth solution, containing 1.9×10^{-4} M H_2PtCl_6 and 5×10^{-3} M TSC, was mixed with 0.1 mL of a 0.1 M freshly prepared ascorbic acid solution. Next, the seed solution of 3.0 nm PtNPs was added and heated to 100 °C. Depending on the volume of the added seed solution, the obtained PtNFs show different sizes. With seed solution volumes of 1.0; 0.8; 0.6; 0.4 and 0.2 mL, the resulting solution contained PtNFs with average diameters of 7.0; 8.0; 10.0; 14.0 and 20.0 nm, respectively.

Preparation of 31.0 nm PtNFs. The PtNFs solution containing 7.0 nm diameter particles was used as the seed solution in the third step. 20 mL of the growth solution, containing 1.9×10^{-4} M H_2PtCl_6 and 5×10^{-3} M TSC, was mixed with a 0.1 mL of a 0.1 M freshly prepared ascorbic acid solution. Next, 0.2 mL of the seed solution was added and heated to

100 °C. The average particle diameter measured from the transmission electron micrograph was 31.0 nm.

5.2.3. Characterization of nanoparticles

The UV-Vis absorption spectrum of the obtained solution was recorded by UV-Vis spectroscopy (Lambda 950) (Figure 5.1). X-ray diffraction (XRD) spectra of the PtNFs were characterized by using a D8 Advanced Bragg X Ray powder diffraction with Cu Kα radiation at room temperature (Figure 5.2). The particles diameters were determined by TEM using a JEOL Model JEM-1400 at 100 kV (Figure 5.3). SHG measurements of PtNFs are performed by HLS at 1.064 µm from a Q- switched Nd^{3+}: YAG nanosecond laser (SAGA from Thales Laser) at a 10 Hz repetition rate.

5.3. Results and Discussion

5.3.1. UV-Vis spectra, XRD and TEM analysis

The nanoflowers synthesis reactions are very fast in mild heating (100 °C) conditions in the presence of a strong reducing agent such as ascorbic acid. The H_2PtCl_6 aqueous solution is pale yellow and shows a peak at 259 nm in its UV-Vis spectrum as shown in Figure 5.1.

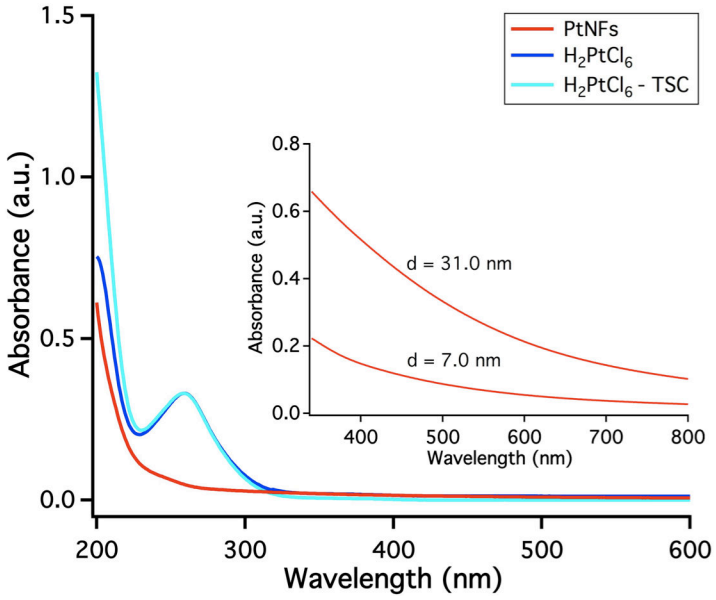

Figure 5.1 *UV-Visible-absorption spectra of the PtNFs solution, H_2PtCl_6 and H_2PtCl_6-TSC, $C_{Pt} = 1.6 \times 10^{-5}$ M. Insert: Visible absorption spectra of two solutions of PtNFs of different diameters, $C_{Pt} = 1.92 \times 10^{-4}$ M.*

On the other hand, H_2PtCl_6 in TSC solution shows the same peak at 259 nm, characteristic of the $[PtCl_6]^{2-}$ complex. The color of the solution becomes brown yellow and finally becomes pale brown when adding ascorbic acid. This pale brown color at a 1.92×10^{-4} M concentration is due to the very broad absorption band related to the Pt plasmonic resonance, this band extending far away from its maximum within the visible range (see insert in Figure 5.1). The $[PtCl_6]^{2-}$ peak at 259 nm in the UV-Vis spectrum disappears, suggesting that most of $[PtCl_6]^{2-}$ ions are reduced, so the reaction process is almost complete.[252,255]

The XRD of PtNFs obtained by reduction by ascorbic acid exhibits diffraction peaks at 2θ between 40 and 85° as shown in Figure 5.2. These XRD data confirmed the formation of face-centered-cubic (fcc, a = 3.92 Å) Pt nanocrystals at 2θ values of 40°; 46,5°, 68° and 81° representing the (111), (200), (220) and (311) planes of the fcc structure.

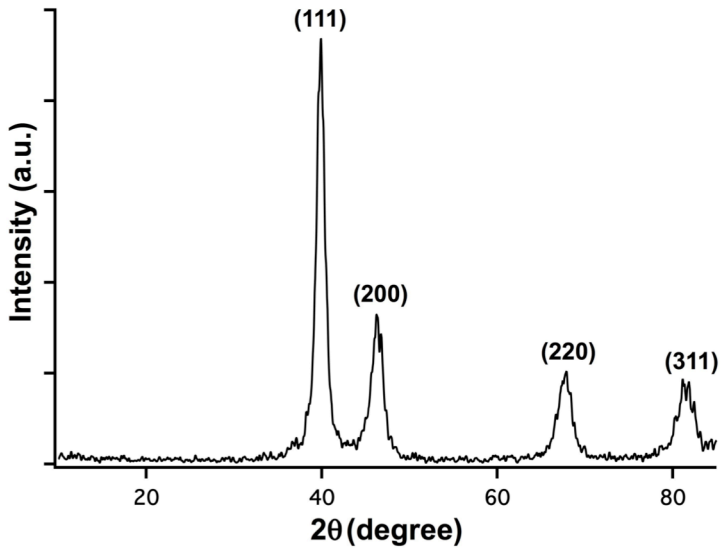

Figure 5.2 *XRD pattern of the PtNFs.*

The size and shape of particles were determined with TEM imaging. Samples for TEM were prepared by dropping a platinum colloidal solution onto a carbon-coated Cu grid, followed by slow evaporation of solvent at room temperature. Figure 5.3 shows TEM images of PtNFs and indicates the average diameter of the particles obtained by measuring and averaging diameters for about 100 particles. Higher resolution insets clearly confirm that most of PtNP's are "nanoflowers".

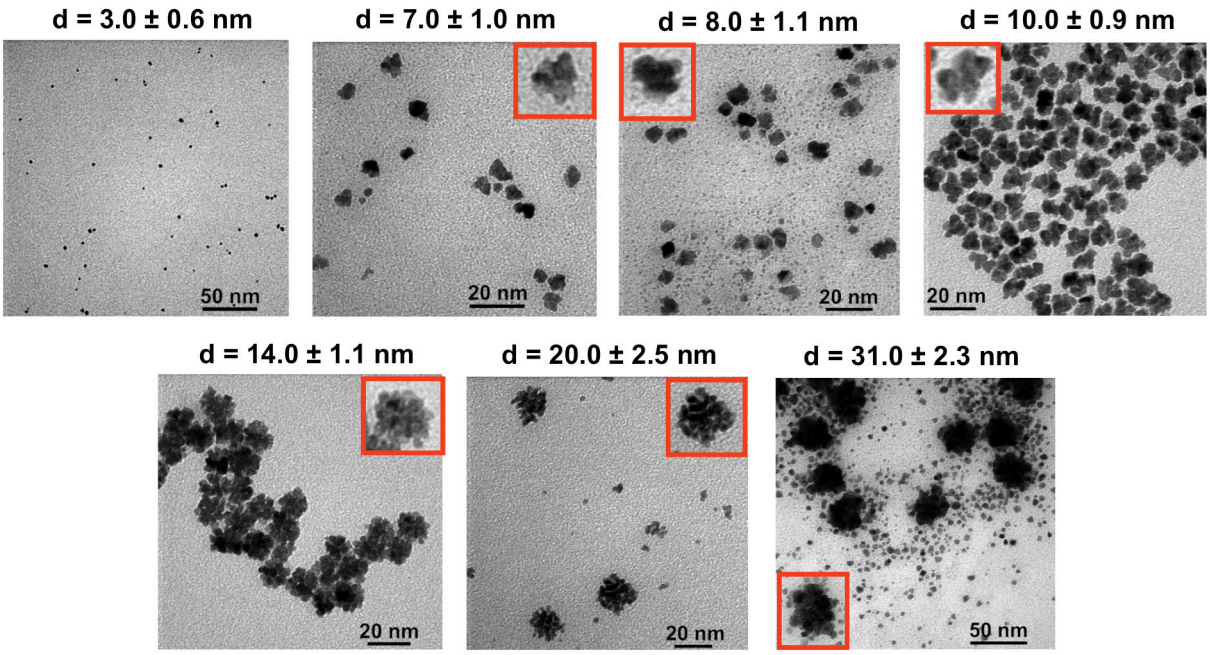

Figure 5.3 *TEM images of PtNFs with various sizes. The diameter d of nanoflowers is determined by averaging diameter values of 100 particles.*

5.3.2. NLO properties of PtNFs

We have checked that the HLS signal arises only from a SHG process and not from broadband visible emission from laser-induced damage on PtNFs (see below). As the plasmonic resonance wavelength is very far away from fundamental and harmonic laser wavelengths, no fluorescence signal (one- or two-photons) is observed for PtNFs.

Figure 5.4 shows the SH intensity observed for pure water and for a PtNFs solution plotted with respect to the SH intensity collected from a NPP (N-4-nitrophenyl-prolinol)[63] powder (frequency doubler) at a 1064 nm fundamental wavelength.[9] The linear variation of this HLS signal with respect to $I_{NNP}^{2\omega}$ precludes any contribution from laser-induced damage on PtNFs, this latter phenomenon being characterized by a clear depart from this expected linear behavior beyond a given $I_{NNP}^{2\omega}$ value (threshold phenomenon). The value of the slope P displays a linear dependence with nanoparticle concentration (Figure 5.5), as expected from eqn (2.6).

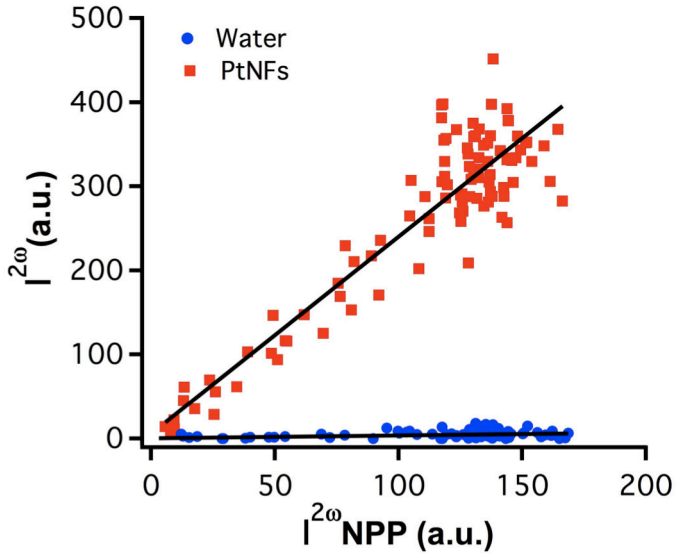

Figure 5.4 *Comparison between the SH intensity recorded from pure water (blue disks) and from 3.5 × 10^{-10} M PtNFs solution (red squares) with respect to the SH intensity collected from the NPP powder at 1064 nm fundamental wavelength.*

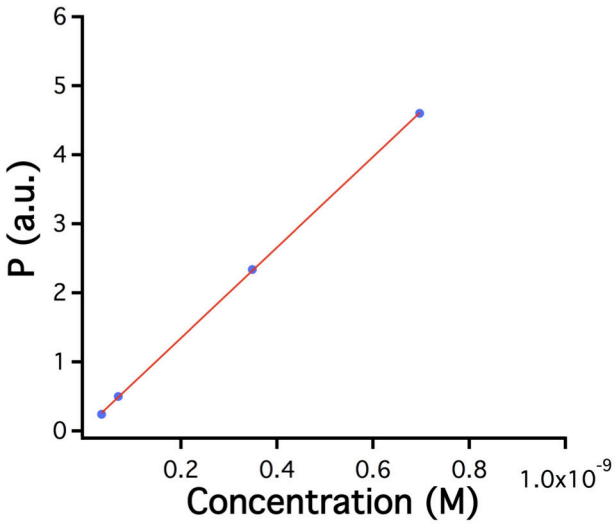

Figure 5.5 *The slope of the HLS intensity of nanoparticle recorded from PtNFs solutions (20nm) with different nanoparticle concentrations. The straight lines results from a linear fit with a remarkable correlation coefficient (0.999).*

Table 5.1 *First hyperpolarizability (β) values of Pt per atom and per particle. The relative experimental error on β is ± 15%, mainly due to the uncertainly from HLS measurements in water, the signal/noise ratio for the SHG signal being much lower in this case than for PtNFs solutions.*

Sample	Diameter (nm)	Volume (nm^3)	N_{Pt} per particle ($\times 10^3$)	Particle concentration	β per particle (β) ($\times 10^{-26}$ esu)	β per Pt atom (β') ($\times 10^{-30}$ esu)	Surface area (nm^2)
PtNF 1	7.0	180	12	1.63E-08	2.8	260	150
PtNF 2	8.0	270	18	1.09E-08	3.8	280	200
PtNF 3	10.0	520	34	5.60E-09	5.7	310	310
PtNF 4	14.0	1400	95	2.04E-09	11.3	370	620
PtNF 5	20.0	4200	280	3.48E-10	23.5	450	1300
PtNF 6	31.0	15600	1026	3.12E-11	61.0	600	3000

Remarkably high β values of PtNFs are measured and presented in Table 5.1. When comparing β values of PtNFs to the results of gold nanospheres (AuNSs) obtained by Galletto *et al.*[13], for particles with the same diameter range (4.9-22.0 nm), our results for PtNFs (from 2.8 to 23.5 $\times 10^{-26}$ esu) are higher than the values of AuNSs obtained in the literature (from 0.6 to 16.6 $\times 10^{-26}$ esu). While β values are actually measured per nanoparticle, for comparison between PtNFs of various sizes, it is interesting to study the β' values (hyperpolarizability per Pt atom) which are given by eqn (2.8).

The β values per particle increase with the surface area of PtNFs (from 2.8 to 61.0 $\times 10^{-26}$ esu), β' increasing with nanoflower diameter (from 260 to 600 $\times 10^{-30}$ esu), in a 7.0 to 31.0 nm diameter range. In Figure 5.6a, these results emphasize the strong dependence of the first hyperpolarisability (β) of the platinum colloids on the average surface area of nanoflower. A linear dependence of β per particle with respect to the surface area of PtNFs is observed, indicating a local, dipolar-type response arising from surface effects, as proposed in previous papers.[15]

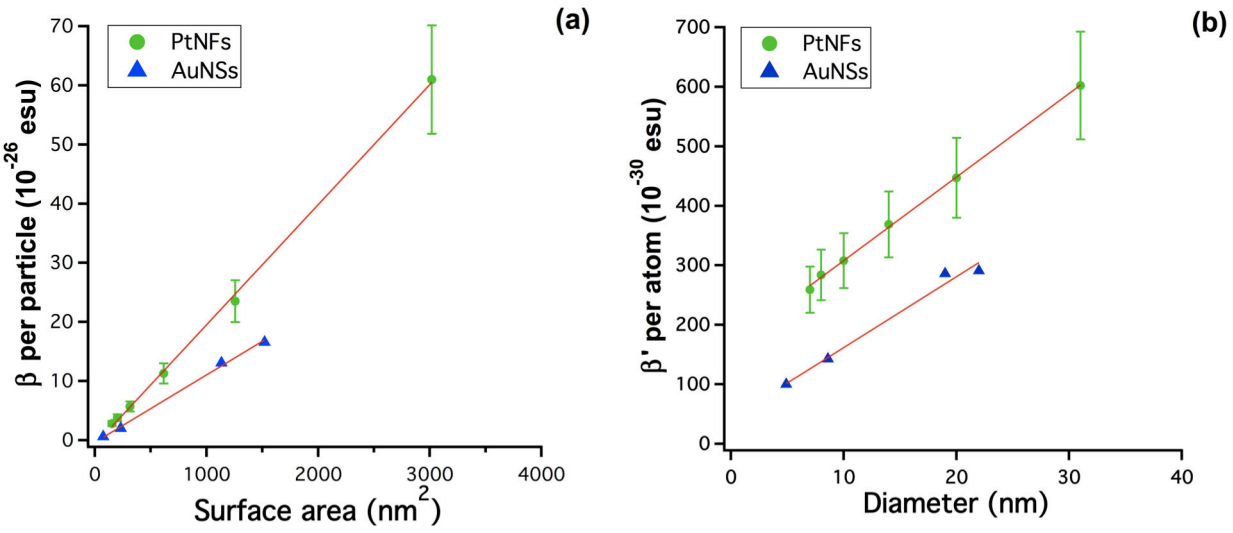

Figure 5.6 *(a) HLS values of the first hyperpolarizability (β) per Pt particle (green disks, this work) and per Au particle*[13] *(blue triangles) in water solution as a function of the surface area of nanoparticles. (b) HLS values of the first hyperpolarizability (β') per Pt atom (green disks, this work) and per Au particle*[13] *(blue triangles) in water solution as a function of the diameter of nanoparticles. The straight lines results from a linear fit with a remarkable correlation coefficient (0.999 for β per Pt particle and 0.999 for β' per Pt atom). The β and β' values from Galletto's work*[13] *have been recalculated according to the procedure described in the text.*

This linear behavior is similar to that found for the recalculated *β and β'* values inferred from data by Galletto *et al.*[13] in AuNSs, using their reported *β* values per nanoparticle corrected (i) from correct β_{H_2O} values (0.055 instead of 0.56×10^{-30} esu)[9] and (ii) using eqn (2.8) (see Figure 5.6 and Table 5.2).

Table 5.2 *The recalculated β and β' values inferred from data by Galletto et al.*[13] *in AuNSs using their reported β values per nanoparticle corrected (i) from correct* β_{H2O} *values (0.055 instead of 0.56 × 10*$^{-30}$ *esu)*[9] *and (ii) using eqn (2.8).*

Gold colloid	Diameter (nm)	β per particle (β) ($\times 10^{-26}$ esu)	β per Au atom (β') ($\times 10^{-30}$ esu)	Surface area (nm^2)
a	4.9	0.6	100	80
b	8.6	2.0	143	230
c	19.0	13.1	286	1130
d	22.0	16.6	291	1520

The dipolar character of the β values of our PtNFs is confirmed by the polarization-resolved HRS intensity observed for 20 nm diameter PtNFs. Upon rotation (0-360°) of the incident fundamental polarization, the HLS response is analyzed vertically (Figure 5.7 (a)) and horizontally (Figure 5.7 (b)). The pattern of the polar plot for a vertical polarization analysis at 2ω corresponds to the expected response of an electric dipole, confirming that the HLS signal from the small metallic nanoparticles is of pure electric dipole origin.

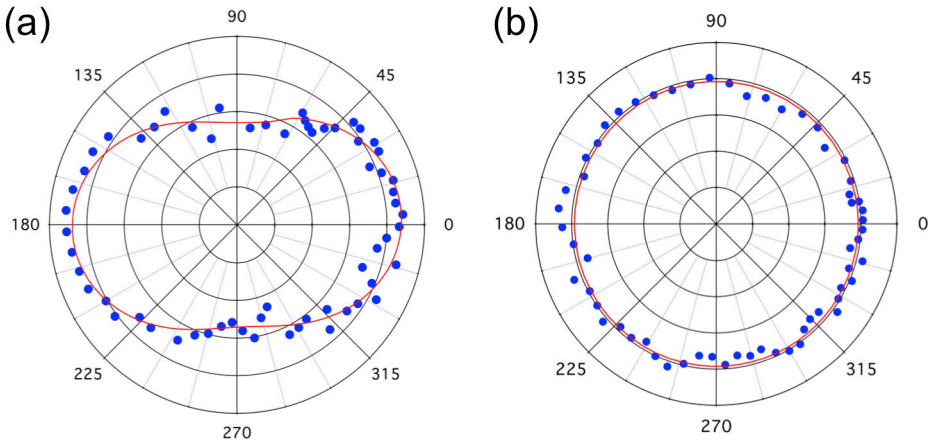

Figure 5.7 *Polar plot of the input polarization angle dependence of the output-HRS intensity from 20nm diameter PtNFs at 1064nm. (a) Verticality polarized SH scattered light and (b) horizontally polarized SH scattered light.*

It has been shown that the first hyperpolarizability of a metal nanoparticle depends on many factors, e.g., the size of the particle, the dielectric constant of the solvent, and particularly the wavelength of the incident light, which is of great importance due to resonance effect. The nature of the metal is also very important and it is interesting to compare β and β' values for NPs with the same diameter and experimental conditions, for different metals. Figure 5.6 (a) and Figure 5.6 (b) demonstrate the higher NLO performances of PtNFs for different surface areas (Figure 5.6 (a)) and particle diameters (Figure 5.6 (b)) as compared to AuNSs. It is interesting to extend this comparison to other noble metal NSs. Here we compare, for particles of the same size (~10, 20 nm), β and β' values of Pt, Au and Ag. For PtNFs, β and β' values are higher than those of Ag and Au NSs. This comparison is presented in Table 5.3.

Table 5.3 *Comparison between previously observed β values of Ag, Au and Pt NFs (this work) per particle/atom at 1064nm.*

Metal [Ref.]	Ag[18]	Ag[23]	Au[13]	Au[13]	Pt	Pt
Diameter (nm)	10	20	8.6	22	10	20
Number of atoms per NPs ($\times 10^3$)	32	248	20	330	34	280
β per particle (β) ($\times 10^{-26}$ esu)	1.58	7.0	2.0	16.6	5.7	23.5
β per atom (β') ($\times 10^{-30}$ esu)	90	135	143	291	310	450

We have calculated the HLS intensities expected at 1064nm from the Agarwal-Jha theory[70] applied to Au, Ag and Pt nanospheres, using the optical constants provided by Palik[256], in order to confirm the prediction made by Johnson *et al.*[23] at 820 nm.

According to the Agarwal-Jha theory, the second harmonic power radiated from a spherical metal-dielectric interface with one- and two photon plasmon resonance can be expressed as follows:[23]

$$S = 192\pi^2 c\left|E(\omega)\right|^4\left(\frac{2\omega R}{c}\right)^6 \times\left\{\left|\frac{e\left[\varepsilon(2\omega)-1\right]/8\pi m\omega^2}{\left[\varepsilon(\omega)+2\right]\left[\varepsilon(2\omega)+2\right]}\right|^2+\frac{36}{5}\left|\frac{e\left[\varepsilon(\omega)-1\right]/8\pi m\omega^2}{\left[\varepsilon(\omega)+2\right]^2\left[2\varepsilon(2\omega)+2\right]}\right|^2\right\}$$

where *e* and *m* are the electron charge and effective mass, *E(ω)* is the field at the fundamental frequency, *R* is the sphere radius, *c* is the velocity of light, *e(ω)* is the relative dielectric constant (defined as $\varepsilon_m / \varepsilon_S$) at incident radiation freq*uency (ω),* and *ε(2ω)* is the corresponding quantity at *2ω, ε_m* is the dielectric constant of the metal nanoparticle, and ε_s is the dielectric constant of the dielectric surrounding medium. Strong enhancement of the HRS signal is expected, therefore, at incident wavelengths coincident with the dipole plasmon absorption maximum. Additionally, the term containing the factor $[\varepsilon(2\omega)+2]^{-2}$ indicates strong HRS enhancement at an incident wavelength that is double the dipole plasmon absorption wavelength. For wavelengths close to 820 nm, the dipole resonance would be dominant for Ag, with respect to Au at 1064 nm; Au is more resonant than Ag.

Our calculations confirm Johnson's results at 820 nm, (Ag more resonant than Au) and show that at 1064nm, the ratio of HLS intensities (per atom) between Pt and Au nanospheres is 0.32. Similarly the ratio between Pt and Ag intensities is 0.59. These ratios are higher than those calculated at 820 nm, but the superiority of experimental β values at 1064 nm for PtNFs with respect to those of Ag and Au NS does not fit these calculated results. Most probably the NLO response of PtNFs does not arise mainly from surface plasmon resonance effects, but from specific surface features. In fact, a careful examination of TEM pictures shows that PtNFs are not perfectly spherical, and display a highly corrugated surface. Therefore, the much higher β values reported for PtNFs are induced by surface corrugation with a limited influence of plasmon resonance. This remark is consistent with the results obtained by K. Das *et al.*[12], this study showing that the β values of low-symmetry, irregularly shaped AuNPs is twice higher than those of centrosymmetric shaped Au nanosphere with a smooth surface. This predominance of corrugation effects seems to be confirmed by the lack of any SHG signal from PtNPs reported in ref.[23,124], these centrosymmetric particles showing smooth surfaces that did not allow for a significant HLS emission contrary to the present work.

5.4. Conclusion

Our work reports the synthesis and characterization of PtNFs with different sizes, controlled by using the seed-mediated method. We have shown for the first time that PtNFs display exceptionally strong first hyperpolarisabilities. These values of PtNFs are found higher than those of gold and silver nanoparticles for particles within the same diameter range. We

demonstrated that the first hyperpolarizability (β and β') linearly depends on the surface area and particles diameter of PtNFs, respectively. Particle surface corrugation and shape irregularities seem to be the dominant factor governing these exceptionally high β values. Further studies are currently in progress to gain a better control of PtNPs shape and smoothness in order to provide a more quantitative interpretation of these high nonlinearities.

Chapter 6
Quadratic nonlinearities of gold nanoprisms in solution

6.1. Introduction

In the previous chapter we have already shown that the linear and nonlinear optical response of gold nanoparticles are largely determined by their composition, size and shape.[219,257] The synthesis of gold nanoparticles with a tight control on their size and shape has been realized with various synthesis conditions and methods leading to nanoprisms,[258–271] nanospheres,[223,224] nanorods,[230–235] nanostars,[236,237] and so on. Among these, nanoprisms or triangular nanoplates display a wide range of geometrically tunable optical features. In particular, the corner sharpness of polygonal nanoparticles significantly influences their optical and electronic properties.[136,272]

The quadratic nonlinear optical (NLO) response of triangular metallic nano-objects has been recently investigated by polarized second-harmonic confocal microscopy in the femtosecond regime.[155] In this pioneering work, focused on NLO investigation of individual nano-objects, strong chiroptical effects from 2D chiral arrangements of gold nanoprisms (AuNPrs) have been evidenced by second harmonic generation (SHG) and further confirmed by numerical simulations. The triangular motif of the investigated nanostructures provides efficient dipole-allowed SHG due to lack of inversion symmetry, as well as sharp corners prone to large local field enhancements.

In this chapter we will focus on the determination of the β hyperpolarizability values of nanoprisms in water solution, using the Harmonic Light Scattering[6,213] (HLS) technique.

The objective of this work is to evidence a strong quadratic nonlinear response for AuNPrs, in connection with their acentric 3-fold symmetry. We explore both the effect of surface area, and the influence of corner sharpness on β values of AuNPrs. These AuNPrs are synthesized in aqueous solution by a rapid one-pot seedless growth process.[259,260,268] Compared to traditional seeded-growth protocols, the seedless method has several advantages, such as rapidity, high reproducibility and high-yield. The resulting AuNPrs are characterized by UV–Vis absorption spectroscopy, transmission electron microscopy (TEM) and HLS.

6.2. Materials and methods

6.2.1. Materials

Tetrachloroauric(III) acid trihydrate ($HAuCl_4.3H_2O$), L-Ascorbic acid ($C_6H_8O_6$, 99%), hexadecyltrimethylammonium chloride (CTAC, 98%), sodium hydroxide (NaOH, ≥ 98%) and potassium iodide (KI, 99%) were purchased from Sigma-Aldrich. The solutions were prepared using ultra-pure water from a Millipore system (18 MΩ cm^{-1}) throughout the experiment. All aqueous samples are at natural pH = 7.

6.2.2. Synthesis of AuNPrs with sharp and smooth corners

AuNPrs were prepared by a seedless growth method. In the typical synthesis, a 10 mL volume of aqueous solution containing CTAC and 7.5×10^{-5} M KI was prepared in a 20 mL flask. To this solution, 0.1 mL $HAuCl_4$ 0.029 M and 29 µL NaOH 0.1 M ($HAuCl_4$: NaOH = 1:1) was added, the solution being stirred for 5 min. Then, 50 µL ascorbic acid 0.1 M was injected into the solution with moderate shaking. The colour of solution changed immediately from yellowish to colourless. Finally, 20 µL NaOH 0.1 M was added and quickly shaken for 2s. No further stirring or agitation was done during crystal growth. The colourless solution turned to red, purple and blue. The growth process can be completed within ~10 min. In the spectra of AuNPr solutions, the 220 nm absorption band characteristic of the original Au(III) solution used for nanoparticle synthesis has disappeared, meaning that the reduction of Au(III) species to atomic Au^0 is complete, and that only gold nanoparticles are formed. Depending on the concentration of CTAC (7.5; 1.0; 1.25; 1.5; 1.75 and 2.0×10^{-3} M), the obtained AuNPrs show different edge length (47.5; 56.6; 66.1; 78.1; 95.4 and 112.3 nm, respectively).

AuNPrs with smoother corners have also been synthesized by gently stirring the solution during crystal growth, instead of keeping it static during the growing process.

6.2.3. Characterization of nanoparticles

UV-Vis absorption spectra of the obtained solutions were recorded by a Lambda 950 spectrometer. Particle sizes were determined by TEM using a JEOL Model JEM-1400 at 100 kV.

6.2.4. Simulation using FDTD method

Finite-difference time-domain (FDTD) numerical calculations based on the version 8.15 of Luminal package were used to simulate the plasmonic properties of AuNPrs[259,260], with the override mesh cell dimensions of $1 \times 1 \times 2$ nm^3. The dimensions of equilateral AuNPrs were 56, 78 and 112 nm in edge length and 25 nm in thickness. The complex dielectric constants of gold were taken from data in Johnson and Christy.[244] An overall simulation region of $1 \times 1 \times 1$ μm^3 was chosen. The wavelength of the total-field scattered-field (TFSF) source used in the simulation ranged from 300 to 1100 nm. The light from the TFSF source was set to be propagating along the z-axis and perpendicular to the triangular plane (Figure 6.3) while the electric field was set parallel to that plane (Figure 6.3). Power monitors in the total field region were used to determine the absorption cross-section. CTAC layers were ignored and the background refractive index was set as 1.33, corresponding to that of the water solvent.

6.3. Results and Discussion

In order to optically characterize the AuPrs solutions, UV−Vis absorption spectra were recorded. These spectra are given in Table 6.1 and Figure 6.1 for sharp-vortex nanoprisms.

The spectral position of the in-plane surface plasmon resonance is highly sensitive to the edge length and the aspect ratio, defined as the ratio between the edge length and the thickness of nano-prisms. In Figure 6.1, the in-plane surface plasmon resonance peak at λ_{max} experiences a red shift (from 627 to 684 nm) when increasing the AuNPr edge length (from 47.5 to 112.3nm).

Table 6.1 *UV-Vis maximum absorption wavelength λ_{max} of AuNPrs solution.*

Sample	λ_{max} (nm)	Edge length (nm)
AuNPr 1	627	47.5 ± 3.2
AuNPr 2	642	56.6 ± 1.5
AuNPr 3	649	66.1 ± 3.5
AuNPr 4	660	78.1 ± 4.1
AuNPr 5	674	95.4 ± 5.8
AuNPr 6	684	112.3 ± 6.4

Nanoprisms also exhibit a weak shoulder between 550 nm and 610 nm, corresponding mostly to the out-of-plane plasmonic mode, with a possible small contribution from the in-plane quadrupolar mode for the largest edge lengths.[272] The characteristic band of spherical Au nanoparticles at 530 nm is much weaker than the two previous ones, suggesting that triangular nanostructures are synthesized with a high morphological yield (*i.e.* high production rate of AuNPr with respect to particles showing other shapes (spheres, rods, *etc.*)),[259] as confirmed by TEM characterization.

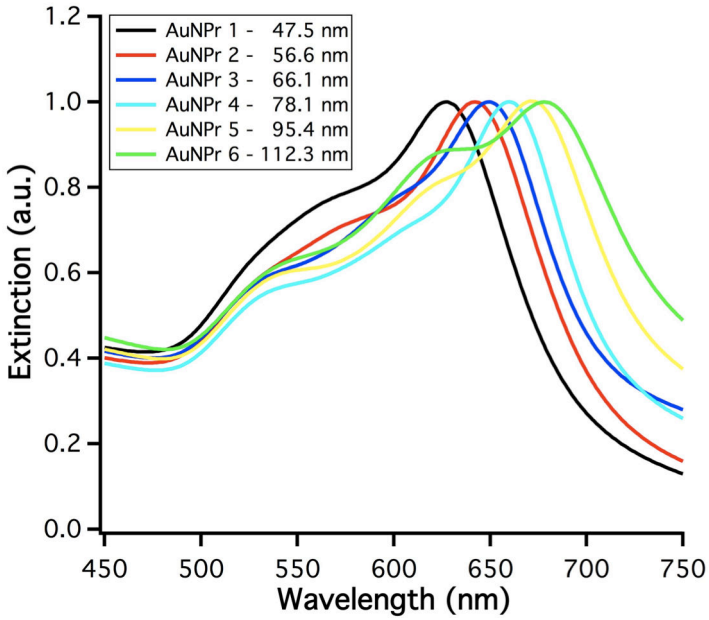

Figure 6.1 *UV-Vis absorption spectra of the AuNPrs solutions of different edge lengths.*

The maximum absorption wavelength (λ_{max}) increases linearly with edge length for particles of the same thickness (Figure 6.2), as already reported in a different context.[272] This linear dependence shows a remarkable correlation coefficient (0.98). Based on the calculation results of Kevin *et al.*[272], the average thicknesses of AuNPrs were guessed to be about 25 nm. This value agrees fully with our TEM characterization and the simulation data for the absorption of AuNPrs by the finite-difference time-domain (FDTD) method.

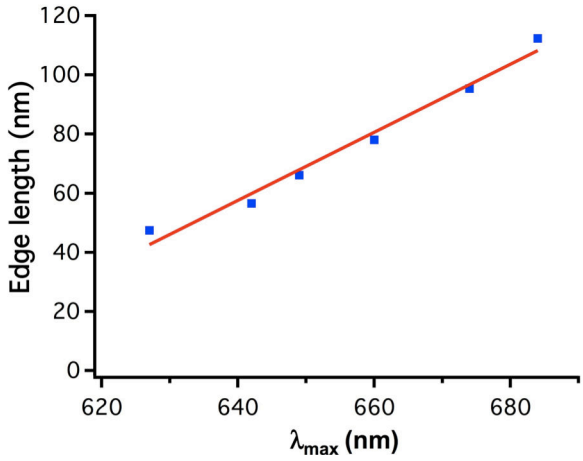

Figure 6.2 *Linear correlation between the average edge length of AuNPrs and the peak wavelength for maximal extinction (λ_{max}).*

As shown in Figure 6.3, we have carried out FDTD simulations, where edge length (set as 56, 78 and 112 nm) and thickness (set as 25 nm) of AuNPrs, are consistent with the experimental results showing an absorption peak at 642, 660 and 684 nm, respectively. The calculated UV-visible spectrum displayed in Figure 6.3 (c) shows a λ_{max} value close to the experimental one, even if the theoretical spectrum is significantly narrower, due to the strictly monodisperse character of the particle size assumed in the calculations. This agreement confirms that the thickness of nanoprisms is the same whatever the edge length can be.

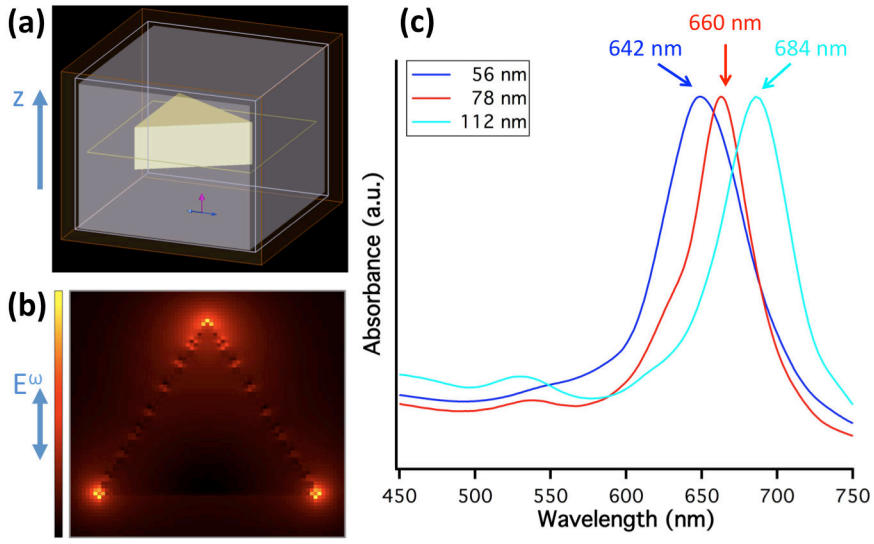

Figure 6.3 *(a) Shape of the domain used to model AuNPrs. (b) Electric field distribution of AuNPrs with an incident wavelength of 642 nm. (c) Absorption spectrum of AuNPrs simulated by FDTD. The thickness of AuNPrs is 25 nm and the edge length has been set as 56, 78, 112 and 25 nm, respectively.*

The size and the shape of particles were determined from TEM imaging (see Figure 6.4, Figure 6.5 and Figure 6.6). Samples for TEM were prepared by dropping a gold colloidal solution onto a carbon-coated Cu grid, followed by slow evaporation of the solvent at room temperature. TEM images of AuNPrs provide the average edge length obtained by measuring and averaging edge lengths for about 100 particles.

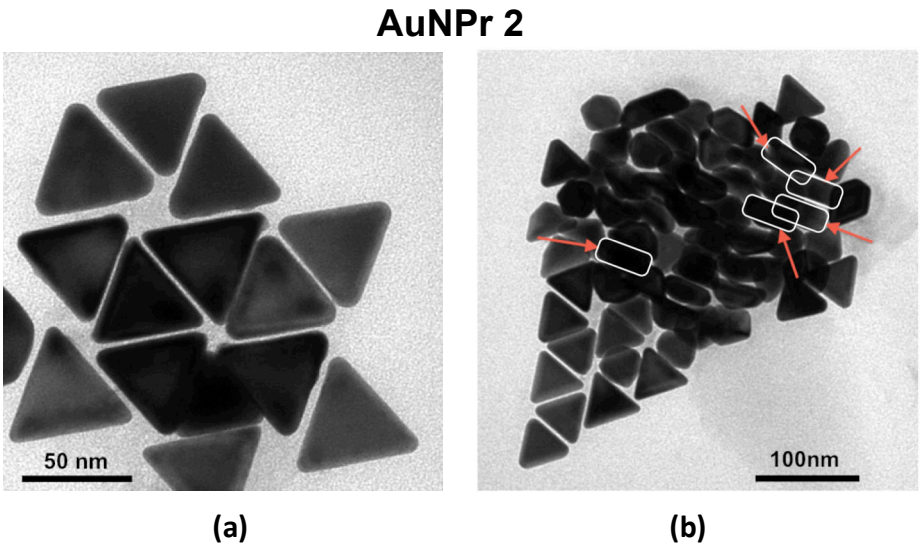

Figure 6.4 *Representative TEM image of AuNPrs (a) with an average edge length of 56.6 ± 1.5 nm and (b) organized according to different orientations, then allowing for the*

determination of prims thickness. The red arrows indicate a selection of vertically oriented AuNPrs.

Figure 6.4 (a) shows AuNPrs with an average edge length of 56.6 ± 1.5 nm, the analysis of vertically oriented nanoprisms in Figure 6.4 (b) results in an average thickness of ~25 nm. This TEM result is in satisfactory agreement with simulation data based on calculations by Kevin *et al.*[272] and their comparison with spectroscopic results. The same average thickness of 25 nm was used to determine the volume of all AuNPrs.

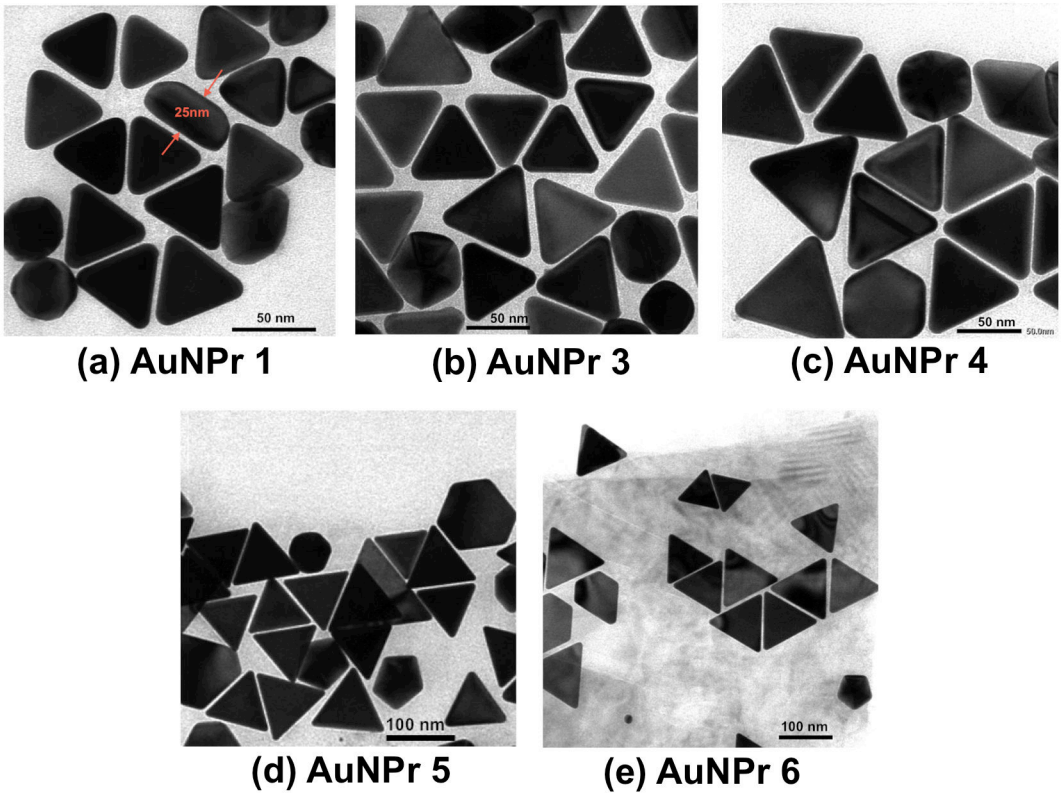

Figure 6.5 *TEM images of AuNPrs with tunable edge length. The average edge length of each sample is (a) 47.5 ± 3.2 nm; (b) 66.1 ± 3.5 nm; (c) 78.1 ± 4.1 nm; (d) 95.4 ± 5.8 nm and (e) 112.3 ± 6.4 nm.*

It should be noted that the TEM images were obtained directly from the original product, with no previous size selection or purification process. As shown in Figure 6.5, monodispersed AuNPrs with sharp tips and various edge lengths have been successfully prepared. From TEM characterization, it is found that the morphological yield of AuNPrs is high (more than 80%), which is in good agreement with UV-Vis spectra.

TEM images have also been obtained for particles displaying smoother corners, as shown in Figure 6.6 below.

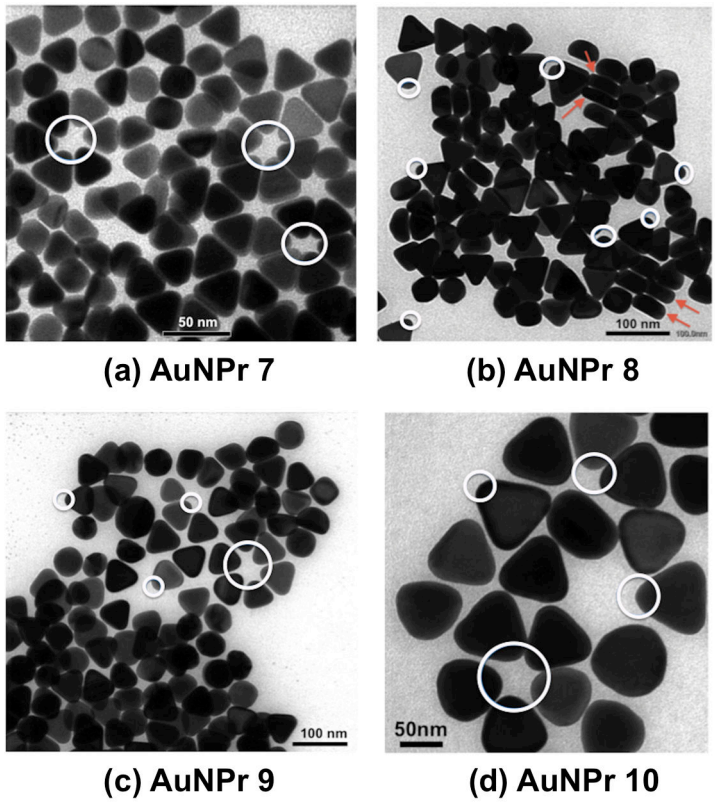

Figure 6.6 *TEM image of AuNPrs with smoother corners. The average edge length of each sample is (a) 30.3 ± 2.2 nm; (b) 52.5 ± 2.9 nm; (c) 68.7 ± 3.4 nm and (d) 80.4 ± 4.8 nm. The red arrows indicate vertically oriented AuNPrs. The white circles emphasize the diminished sharpness of nano-prism corners.*

Particle concentration is calculated from the known concentration of the initial gold solution, and from the average volume of nanoprisms. The β and β' values are calculated by using eqn (2.7) and (2.8). All values are presented in Table 6.2.

The increasing β and β' values for AuNPrs (from 177 to 759 x 10^{-26} esu per particle and from 1470 to 2670 x 10^{-30} esu per atom, respectively) correspond to a rise in the nanoprism edge length from 47.5 to 112.3nm. A linear dependence of β per particle with respect to the surface area of AuNPrs is observed (Figure 6.7 (a)), with a remarkable correlation coefficient

(0.996), indicating a local, dipolar-type response arising from surface effects.[15] When comparing β values per nanoprism to the results obtained in our previous work for Au nanospheres,[19] both AuNPrs and Au nanospheres show a linear dependence of their β values with respect with their surface area, but with a higher slope for AuNPrs, as could be expected from non-centrosymmetric nanostructures.

Table 6.2 *The first hyperpolarizability of Au per atom (β') and per particle (β). The relative experimental error on β is ± 15%, mainly due to the uncertainly from HLS measurements in water, the signal/noise ratio for the SHG signal being much lower in this case than for AuNPrs solutions.*

Sample	Edge length (nm)	Volume (nm^3)	N_{Au} per particle ($\times 10^3$)	Particle concentration	β per particle (β) ($\times 10^{-26}$ esu)	β per atom (β') ($\times 10^{-30}$ esu)	Surface area (nm^2)
AuNPr 1	47.5 ± 3.2	24400	1440	6.78E-12	177	1470	5520
AuNPr 2	56.6 ± 1.5	34700	2050	4.78E-12	246	1720	7020
AuNPr 3	66.1 ± 3.5	47300	2800	3.50E-12	311	1860	8740
AuNPr 4	78.1 ± 4.1	66000	3910	1.25E-12	421	2130	11140
AuNPr 5	95.4 ± 5.8	98500	5830	8.41E-13	611	2530	15040
AuNPr 6	112.3 ± 6.4	136500	8080	6.07E-13	759	2670	19340

The linear dependence of β' with edge length can be explained as follows. As shown here, β depends linearly on the surface area, according to the formulae below:

$$\beta \ \alpha \ S = \frac{\sqrt{3}}{2} l^2 + 3.l.d \tag{6.1}$$

$$\beta' = \frac{\beta}{\sqrt{N}} \ \alpha \ \frac{S}{\sqrt{V}} = \frac{\frac{\sqrt{3}}{2} l^2 + 3.l.d}{\sqrt{\frac{\sqrt{3}}{4}.l^2.d}} = \frac{\frac{\sqrt{3}}{2} l + 3d}{\sqrt{\frac{\sqrt{3}}{4} d}} \tag{6.2}$$

$$\Rightarrow \beta' \ \alpha \ A\frac{l}{\sqrt{d}} + B\sqrt{d} \tag{6.3}$$

where S, V, l and d are respectively the surface area, volume, edge length and thickness of nanoprism.

From eqn (6.3) above, we can conclude that β' depends on l and d. As d is the same for all nanoprisms, β' depends only on l. As expected from eqn (6.3), a linear dependence of β' per atom with respect to the edge length of AuNPrs is observed (see Figure 6.7 (b)), with a remarkable correlation coefficient (0.981).

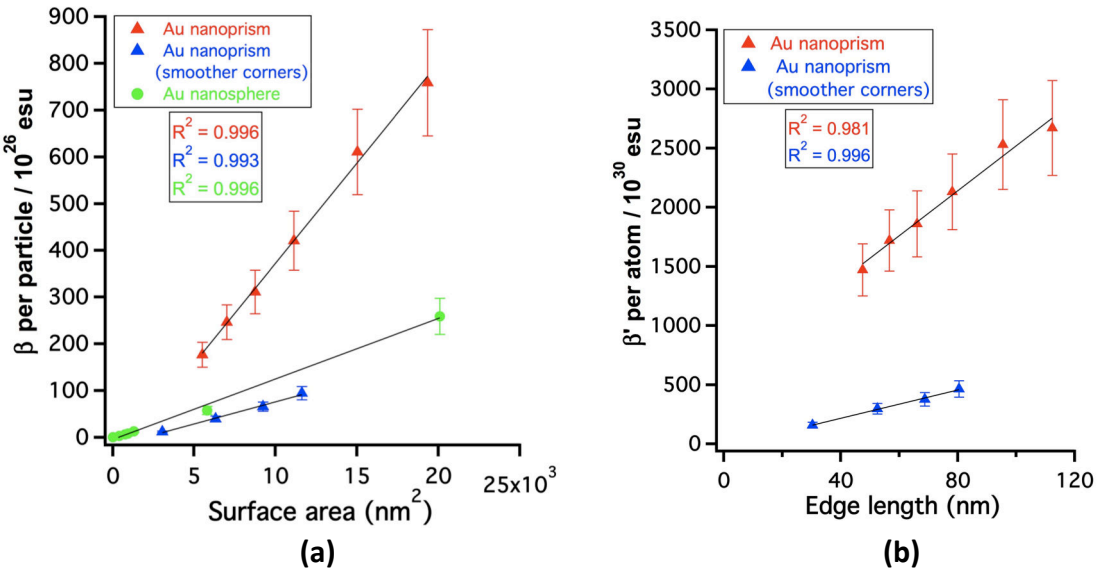

Figure 6.7 *(a) HLS values of the first hyperpolarizability (β) per AuNPr (red and blue triangles) and per Au nanosphere (green disks[19]) in water solution as a function of the surface area of nanoparticles. (b) HLS values of the first hyperpolarizability (β') per Au atom in water solution as a function of the average edge length of AuNPrs. The black line is the least-square linear fit of β (resp. β') with respect to surface area (resp. edge length).*

It can be pointed-out that these experimental β (or β') values are not corrected from resonance effects of β at ω and 2ω. When increasing the edge length l of AuNPr, the red-shift of λ_{max} implies that the contribution of the 2ω - resonance to β value decreases, whereas that of the ω - resonance increases. If we use a simple two level dispersion model for β,[273]

$$\beta = \frac{\beta_0}{\left(1-\left(\frac{\lambda_{max}}{\lambda}\right)^2\right)\left(1-\left(\frac{2\lambda_{max}}{\lambda}\right)^2\right)} \quad (6.4)$$

where β_0 is so-called "static", dispersion-free hyperpolarizability, we find that the change of the exaltation factor due to ω (or λ) and 2ω (or $\lambda/2$) resonance does not vary strongly with l values (from 3.94 for l = 47.5 to 2.63 for l = 112.3). In Figure 6.8, a new plot of β_0 with respect of surface area shows a linear behaviour with a remarkable correlation coefficient (0.997). Therefore, taking into account resonance effects does not change the conclusion of our work.

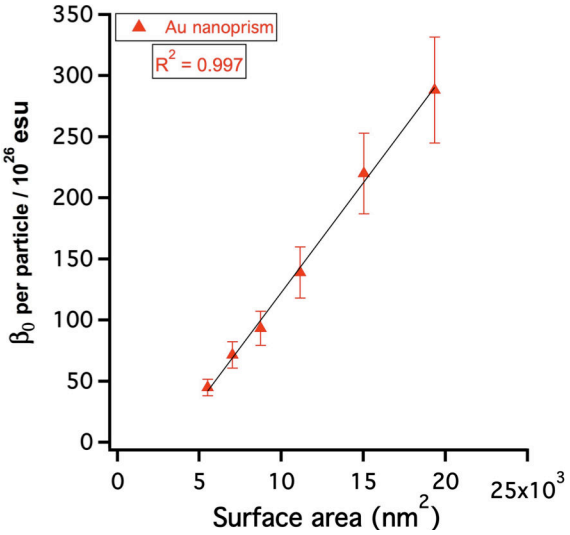

Figure 6.8 *HLS values of the static first hyperpolarizability (β_0) per AuNPr (red triangles) in water solution as a function of the surface area of nanoparticles. The black line is the least-square linear fit of β_0 with respect to surface area.*

It must be pointed-out that β and β' values for AuNPrs with smooth corners are much smaller that for sharp corner AuNPrs (see Table 6.3). The comparison of hyperpolarizability values for nanospheres on the one hand and for AuNPrs with smoother corners on the other hand does not evidence a significant difference between non-centrosymmetric "smooth" nanoprisms and centrosymmetric nanospheres. This behavior shows that the sharpness of the corners dominates the SHG emission process over centrosymmetry breaking for small

nanoparticles. This seems consistent with the unexpectedly high β values of platinum nanoflowers reported in ref.[20]: the nonlinear response from these particles made of a metal that does not display any plasmonic resonance in the visible range has been assigned to the high roughness of the particle surface, when displaying several sharp tips.

Table 6.3 *The first hyperpolarizability of Au per atom (β') and per particle (β) for AuNPrs with smooth corners. The relative experimental error on β is ± 15%, mainly due to the uncertainly from HLS measurements in water, the signal/noise ratio for the SHG signal being much lower in this case than for AuNPrs solutions.*

Sample	Edge length (nm)	Volume (nm^3)	N_{Au} per particle ($\times 10^3$)	Particle concentration	β per particle (β) ($\times 10^{-26}$ esu)	β per atom (β') ($\times 10^{-30}$ esu)	Surface area (nm^2)
AuNPr 7	30.3 ± 2.2	9940	590	1.67E-11	12	158	3070
AuNPr 8	52.5 ± 2.9	29840	1770	5.55E-12	40	297	6320
AuNPr 9	68.7 ± 3.4	51090	3020	3.24E-12	66	377	9240
AuNPr 10	80.4 ± 4.8	69980	4140	1.18E-12	95	465	11630

6.4. Conclusion

In summary, AuNPrs with tailored edge lengths and controllable corner smoothness have been prepared using a rapid seedless growth process. To the best of our knowledge, we report for the first time hyperpolarizability measurements for colloidal AuNPrs using HLS at 1064 nm, resulting in high β values for particles with sharp corners, with a linear dependence with respect to their surface area. This large increase of β values as compared to those of nanospheres or nanorods of similar surface areas seems to originate from sharp tip effects rather that from centrosymmetry breaking, as non-centrosymmetric AuNPrs with smoother corners do not display hyperpolarizability values significantly higher than those of centrosymmetric particles. These results shed a new light on SHG properties of small metallic nanoparticles in solution. Further studies to be carried-out by confocal SHG microscopy on single nanoparticles should provide more information about their quadratic NLO behaviour.

Conclusions and Perspectives

This thesis has been focused on the synthesis and investigation of nonlinear optical (NLO) properties of noble metal nanoparticles (NMNPs) of various sizes and shapes such as powdery-silver nanospheres, gold and silver nanospheres (AuNSs and AgNSs); towards more specific geometries such as gold and silver nanorods (AuNRs and AgNRs), platinum nanoflowers (PtNFs) and gold nanotriangles or nanoprisms (AuNPrs). The second harmonic generation (SHG) technique named Harmonic Light Scattering (HLS) used for the detection of second-order nonlinear optical responses of NMNPs was presented. The first hyperpolarizability β values of NMNPs at 1064 have been measured. The important conclusion of this thesis is summarized below:

- The synthesis of colloidal AuNSs with different size, *i.e.* AuNSs (diameters 3.0; 11.6; 15.8; 17.4; 20.0 and 43 nm), which were controlled by varying the protective agent, the reductive agent and by using the seed-mediated method. Colloidal AgNSs (diameters ~10.0 nm) were produced by a simple and quick chemical reduction method using different protective agents (PVA, PVP). For metallic nanospheres, we found that their β values are governed by a purely local, dipolar contribution, as confirmed by their surface area dependence. The hyperpolarizability values of AuNSs are higher than those of AgNSs at 1.06 μm due to strong plasmon resonance effects for gold nanoparticles at this wavelength. These values are consistent with the data from the previous literature. Additionally, AgNSs proved to be strong nonlinear scatterers, independent on the nature of the stabilizing agents.

  Powdery-AgNSs (diameters ~7.0 nm) have been synthesized by thermal decomposition of silver oxalate. The powder shows excellent nonlinear emission, as

confirmed by SHG green light visible with naked eye ($d_{eff}^{AgNPs} = 0.28 pmV^{-1}$, close to that of KDP), not only in solution but also in the solid state.

- Colloidal solutions of AuNRs with difference aspect ratios (1.47; 1.63 and 2.30) were prepared by using the seed-mediated method. Specially, silver nanorods (AgNRs) were homogenously synthesized by a one-step growth method with tunable aspect ratio (5.0; 6.3; 7.5; 8.2 and 9.7). It has been demonstrated that this fabrication method would be a reliable and promising fabrication method appropriated to application purposes due to the simple and inexpensive synthesis technique and high qualification in reproducibility. We report, for the first time, the evidence of a strong quadratic nonlinear response for AgNRs. The first hyperpolarizability β values show the strong dependence on the average surface area of nanorods, both for AuNRs and AgNRs. As an important consequence of these surface effects, we have revisited the previously reported aspect ratio dependence of β values for AuNRs, and evidenced the predominant influence of nanoparticle area over aspect ratio considerations.

- PtNFs were elaborated in aqueous solution using the seed-mediated growth method for six different diameters (~7.0; 8.0; 10.0; 14.0; 20.0 and 31.0 nm). We have shown for the first time that PtNFs display exceptionally strong first hyperpolarisabilities. Particle surface corrugation and shape irregularities are responsible for these exceptionally high β values of PtNFs.

- The synthesis and NLO characterization of AuNPrs with controllable localized surface plasmon resonance were reported. Colloidal solutions of AuNPrs with various edge lengths, ranging from 47.5 to 112.3 nm, have been fabricated by an original, one-step and seedless synthesis method. From HLS experiments, for the first time, we demonstrate that hyperpolarizability (β) values of AuNPrs display not only a linear dependence with respect to the surface area, but are also sensitive to the sharpness of the triangle vertices. AuNPrs with smoother corners do not display hyperpolarizability values significantly higher than those of AuNSs, which clearly demonstrate once again the strong dependence of hyperpolarizabilities on the sharp tip of nanoprisms.

It is expected that the noble metal nanoparticles reported in this thesis would have potential applications for nonlinear optical devices. So it would be interesting to study the nonlinear optical properties of a photonic structure containing active nanoparticles reported in this thesis for device applications. Specially, the powdery- AgNSs would have many potential applications for antimicrobial technology. Further more, the NMNPs reported in this thesis can be produced in large scale in low preparation cost.

Further studies are currently in progress towards higher surface areas of NMNPs in order to explore NMNP nonlinearities beyond the dipolar behaviour; additionally, polarization-resolved HRS measurements can be considered. The new, simple, low cost and facile methods are being developed for the preparation of NMNPs with more special geometries such as nanostars, nanocubes, nanorice, *etc.* Anisotropic features in nonspherical nanoparticles make them ideal candidates for enhanced chemical, catalytic, and local field related applications. Looking further to future potential applications, one can expect that the NMNPs of controlled morphologies will find applications as in vivo force sensors; morphological seeds for aligned block copolymer/ inorganic nanocomposites with anisotropic properties; smart catalysts (for fuel cells, waste treatment, bioprocessing, *etc.*); enhancers in photovoltaics and other energy conversion devices; better therapeutic and imaging agents; probes for single-molecule sensing of drugs, toxins, and environmental pollutants; and key components in energy transport and novel opto-electronic devices. NMNPs, with their red shifted LSPR to the near-infrared, where absorption, scattering, and fluorescence from endogenous biological chromophores are minimal, appear to be attractive for biological and medical application, as NLO probes, drug carriers and tumorous cell killer via hyperthermia.

Bibliography

1. Franken, P. A., Hill, A. E., Peters, C. W. & Weinreich, G. Generation of Optical Harmonics. *Phys. Rev. Lett.* **7,** 118–119 (1961).
2. Maiman, T. H. Stimulated Optical Radiation in Ruby. *Nature* **187,** 493–494 (1960).
3. Boyd, R. W. *Nonlinear Optics*. (Academic Press, 1992).
4. Zyss, J. *Molecular Nonlinear Optics: Materials, Physics, and Devices*. (Academic Press, 1994).
5. Zyss, J. & Ledoux, I. Nonlinear optics in multipolar media: theory and experiments. *Chem. Rev.* **94,** 77–105 (1994).
6. Terhune, R. W., Maker, P. D. & Savage, C. M. Measurements of Nonlinear Light Scattering. *Phys. Rev. Lett.* **14,** 681–684 (1965).
7. Clays, K. & Persoons, A. Hyper-Rayleigh scattering in solution. *Phys. Rev. Lett.* **66,** 2980–2983 (1991).
8. Novoa, N. *et al.* Four-coordinate nickel(II) and copper(II) complex based ONO tridentate Schiff base ligands: synthesis, molecular structure, electrochemical, linear and nonlinear properties, and computational study. *Dalton Trans.* **44,** 18019–18037 (2015).
9. Singh, A., Lehoux, A., Remita, H., Zyss, J. & Ledoux-Rak, I. Second Harmonic Response of Gold Nanorods: A Strong Enhancement with the Aspect Ratio. *J. Phys. Chem. Lett.* **4,** 3958–3961 (2013).
10. El Harfouch, Y. *et al.* Hyper-Rayleigh Scattering from Gold Nanorods. *J. Phys. Chem. C* **118,** 609–616 (2014).
11. Hubert, C. *et al.* Role of surface plasmon in second harmonic generation from gold nanorods. *Appl. Phys. Lett.* **90,** 181105 (2007).
12. Das, K. *et al.* Hyper-Rayleigh scattering from gold nanoparticles: Effect of size and shape. *Spectrochim. Acta. A. Mol. Biomol. Spectrosc.* **128,** 398–402 (2014).
13. Galletto, P., Brevet, P. F., Girault, H. H., Antoine, R. & Broyer, M. Size dependence of the surface plasmon enhanced second harmonic response of gold colloids: towards a new calibration method. *Chem. Commun.* 581–582 (1999).
14. Nappa, J. *et al.* Hyper-Rayleigh scattering of gold nanorods and their relationship with linear assemblies of gold nanospheres. *Faraday Discuss.* **125,** 145 (2004).
15. Russier-Antoine, I., Benichou, E., Bachelier, G., Jonin, C. & Brevet, P. F. Multipolar contributions of the second harmonic generation from silver and gold nanoparticles. *J. Phys. Chem. C* **111,** 9044–9048 (2007).
16. Nappa, J. *et al.* Electric dipole origin of the second harmonic generation of small metallic particles. *Phys. Rev. B* **71,** 165407 (2005).
17. El Harfouch, Y. *et al.* Effect of a thioalkane capping layer on the first hyperpolarizabilities of gold and silver nanoparticles. *J. Phys. Condens. Matter* **24,** 124104 (2012).
18. Ngo, H. M. & Ledoux-Rak, I. Second harmonic generation from silver nanoparticles in aqueous solution with different protective agents. in *Proc. SPIE 9171* **9171,** 91710Y–91710Y–6 (2014).

19. Ngo, H. M., Nguyen, P. P. & Ledoux-Rak, I. Optimization of second harmonic generation of gold nanospheres and nanorods in aqueous solution: the dominant role of surface area. *Phys. Chem. Chem. Phys.* **18,** 3352–3356 (2016).
20. Ngo, H. M., Lai, N. D. & Ledoux-Rak, I. High second-order nonlinear response of platinum nanoflowers: the role of surface corrugation. *Nanoscale* **8,** 3489–3495 (2016).
21. Jais, P. M., von Bilderling, C. & Bragas, A. V. Plasmon-enhanced second harmonic generation in semiconductor quantum dots close to metal nanoparticles. *Pap. Phys.* **3,** (2011).
22. Johnson, C. K. & Soper, S. A. Nonlinear surface-enhanced spectroscopy of silver colloids and pyridine: hyper-Raman and second-harmonic scattering. *J. Phys. Chem.* **93,** 7281–7285 (1989).
23. Johnson, R. C., Li, J., Hupp, J. T. & Schatz, G. C. Hyper-Rayleigh scattering studies of silver, copper, and platinum nanoparticle suspensions. *Chem. Phys. Lett.* **356,** 534–540 (2002).
24. Shaviv, E. & Banin, U. Synergistic Effects on Second Harmonic Generation of Hybrid CdSe−Au Nanoparticles. *ACS Nano* **4,** 1529–1538 (2010).
25. Kurtz, S. K. & Perry, T. T. A Powder Technique for the Evaluation of Nonlinear Optical Materials. *J. Appl. Phys.* **39,** 3798–3813 (1968).
26. Chemla, D. S. & Zyss, J. *Nonlinear Optical Properties of Organic Molecules and Crystals*. (Academic Press, 1987).
27. Nalwa, H. S. & Miyata, S. *Nonlinear Optics of Organic Molecules and Polymers*. (CRC Press, 1996).
28. de la Torre, G., Vázquez, P., Agulló-López, F. & Torres, T. Role of Structural Factors in the Nonlinear Optical Properties of Phthalocyanines and Related Compounds. *Chem. Rev.* **104,** 3723–3750 (2004).
29. Ostroverkhova, O. & Moerner, W. E. Organic Photorefractives: Mechanisms, Materials, and Applications. *Chem. Rev.* **104,** 3267–3314 (2004).
30. Eisenthal, K. B. Second Harmonic Spectroscopy of Aqueous Nano- and Microparticle Interfaces. *Chem. Rev.* **106,** 1462–1477 (2006).
31. Asselberghs, I., Clays, K., Persoons, A., Ward, M. D. & McCleverty, J. Switching of molecular second-order polarisability in solution. *J. Mater. Chem.* **14,** 2831–2839 (2004).
32. Coe, B. J. Switchable Nonlinear Optical Metallochromophores with Pyridinium Electron Acceptor Groups. *Acc. Chem. Res.* **39,** 383–393 (2006).
33. Bruce, D. W., O'Hare, D. & Walton, R. I. *Molecular Materials*. (John Wiley & Sons, 2011).
34. Ledoux, I., Zyss, J., Siegel, J. S., Brienne, J. & Lehn, J.-M. Second-harmonic generation from non-dipolar non-centrosymmetric aromatic charge-transfer molecules. *Chem. Phys. Lett.* **172,** 440–444 (1990).
35. Zyss, J. Molecular engineering implications of rotational invariance in quadratic nonlinear optics: From dipolar to octupolar molecules and materials. *J. Chem. Phys.* **98,** 6583–6599 (1993).
36. Dewey Jr, C. F., Cook Jr, W. R., Hodgson, R. T. & Wynne, J. J. Frequency doubling in $KB_5O_8{\cdot}4H_2O$ and $NH_4B_5O_8{\cdot}4H_2O$ to 217.3 nm. *Appl. Phys. Lett.* **26,** 714–716 (1975).
37. Packiya raj, M., Ravi Kumar, S. M., Srineevasan, R. & Ravisankar, R. Synthesis, growth, and structural, optical, mechanical, electrical properties of a new inorganic nonlinear optical crystal: Sodium manganese tetrachloride (SMTC). *J. Taibah Univ. Sci.* (2015).
38. Giordmaine, J. A. & Miller, R. C. Tunable Coherent Parametric Oscillation in $LiNbO_3$ at Optical Frequencies. *Phys. Rev. Lett.* **14,** 973–976 (1965).
39. Uematsu, Y. Nonlinear Optical Properties of $KNbO_3$-Single Crystal in the Orthorhombic Phase. *Jpn. J. Appl. Phys.* **13,** 1362–1368 (1974).
40. Maker, P. D., Terhune, R. W., Nisenoff, M. & Savage, C. M. Effects of Dispersion and Focusing on the Production of Optical Harmonics. *Phys. Rev. Lett.* **8,** 21–22 (1962).
41. Edelstein, D. C., Wachman, E. S. & Tang, C. L. Broadly tunable high repetition rate femtosecond optical parametric oscillator. *Appl. Phys. Lett.* **54,** 1728–1730 (1989).

42. Klein, M. B., Dunning, G. J., Valley, G. C., Lind, R. C. & O'Meara, T. R. Imaging threshold detector using a phase-conjugate resonator in $BaTiO_3$. *Opt. Lett.* **11,** 575 (1986).
43. Ryasnyansky, A. *et al.* Nonlinear optical absorption of ZnO doped with copper nanoparticles in the picosecond and nanosecond pulse laser field. *Appl. Opt.* **44,** 2839 (2005).
44. Chen, C. *et al.* New nonlinear-optical crystal: LiB_3O_3. *J. Opt. Soc. Am. B* **6,** 616 (1989).
45. Chen, C. *et al.* Design and synthesis of an ultraviolet-transparent nonlinear optical crystal $Sr_2Be_2B_2O_7$. *Nature* **373,** 322–324 (1995).
46. Hellwig, H., Liebertz, J. & Bohatý, L. Exceptional large nonlinear optical coefficients in the monoclinic bismuth borate BiB3O6 (BIBO). *Solid State Commun.* **109,** 249–251 (1998).
47. Druon, F. *et al.* Efficient, tunable, zero-line diode-pumped, continuous-wave Yb3+:$Ca_4LnO(BO_3)_3$ (Ln = Gd, Y) lasers at room temperature and application to miniature lasers. *J. Opt. Soc. Am. B* **17,** 18 (2000).
48. Xue, D., Betzler, K., Hesse, H. & Lammers, D. Nonlinear optical properties of borate crystals. *Solid State Commun.* **114,** 21–25 (2000).
49. Auerhammer, J. M. & Eliel, E. R. Frequency doubling of mid-infrared radiation in gallium selenide. *Opt. Lett.* **21,** 773 (1996).
50. Colvin, V. L., Schlamp, M. C. & Alivisatos, A. P. Light-emitting diodes made from cadmium selenide nanocrystals and a semiconducting polymer. *Nature* **370,** 354–357 (1994).
51. Munn, R. W. & Ironside, C. N. *Principles and Applications of Nonlinear Optical Materials*. (Springer Netherlands, 1993).
52. Feng, X. *et al.* Growth and highly efficient third harmonic generation of ammonium dihydrogen phosphate crystals. *RSC Adv.* **6,** 33983–33989 (2016).
53. Rentzepis, P. M. & Pao, Y.-H. Laser-induced optical second harmonic generation in organic crystals. *Appl. Phys. Lett.* **5,** 156–158 (1964).
54. Heilmeier, G. H., Ockman, N., Braunstein, R. & Kramer, D. A. Relationship between optical second harmonic generation and the electro-optic effect in the molecular crystal hexamine. *Appl. Phys. Lett.* **5,** 229–230 (1964).
55. Gott, J. R. Effect of molecular structure on optical second-harmonic generation from organic crystals. *J. Phys. B At. Mol. Phys.* **4,** 116 (1971).
56. Singh, A. *Nonlinear optical properties of nanostructures, photochromic and lanthanide complexes in solution*. (Cachan, Ecole normale supérieure, 2012).
57. Blair, H. S. & Boyd, N. L. The Effect of the Substrate on the Isomerization of Model Disperse Dyes based on Stilbene. *J. Soc. Dye. Colour.* **92,** 14–16 (1976).
58. Ledoux, I. & Zyss, J. Influence of the molecular environment in solution measurements of the Second-order optical susceptibility for urea and derivatives. *Chem. Phys.* **73,** 203–213 (1982).
59. Cassidy, C., Halbout, J. M., Donaldson, W. & Tang, C. L. Nonlinear optical properties of urea. *Opt. Commun.* **29,** 243–246 (1979).
60. Oudar, J. L. & Chemla, D. S. Hyperpolarizabilities of the nitroanilines and their relations to the excited state dipole moment. *J. Chem. Phys.* **66,** 2664–2668 (1977).
61. Zyss, J., Chemla, D. S. & Nicoud, J. F. Demonstration of efficient nonlinear optical crystals with vanishing molecular dipole moment: Second-harmonic generation in 3-methyl-4-nitropyridine-1-oxide. *J. Chem. Phys.* **74,** 4800–4811 (1981).
62. Joffre, M., Yaron, D., Silbey, R. J. & Zyss, J. Second order optical nonlinearity in octupolar aromatic systems. *J. Chem. Phys.* **97,** 5607–5615 (1992).
63. Zyss, J., Nicoud, J. F. & Coquillay, M. Chirality and hydrogen bonding in molecular crystals for phasematched secondharmonic generation: N(4nitrophenyl)(L)prolinol (NPP). *J Chem Phys* **81,** 4160–4167 (1984).

64. Marder, S. R., Perry, J. W. & Schaefer, W. P. Synthesis of Organic Salts with Large Second-Order Optical Nonlinearities. *Science* **245,** 626–628 (1989).
65. Le Bozec, H. *et al.* Molecular engineering of octupolar tris(bipyridyl) metal complexes. *Synth. Met.* **124,** 185–189 (2001).
66. Powell, C. E. & Humphrey, M. G. Nonlinear optical properties of transition metal acetylides and their derivatives. *Coord. Chem. Rev.* **248,** 725–756 (2004).
67. Berge, B., Wicker, A., Lajzerowicz, J. & Legrand, J. F. Second-Harmonic Generation of Light and Evidence of Phase Matching in Thin Films of P(VDF-TrFE) Copolymers. *EPL Europhys. Lett.* **9,** 657 (1989).
68. Marder, S. R., Stucky, G. D. & Sohn, J. E. *Materials for Nonlinear Optics: Chemical Perspectives*. (American Chemical Society, 1991).
69. Simon, H. J., Mitchell, D. E. & Watson, J. G. Optical Second-Harmonic Generation with Surface Plasmons in Silver Films. *Phys. Rev. Lett.* **33,** 1531–1534 (1974).
70. Agarwal, G. S. & Jha, S. S. Theory of second harmonic generation at a metal surface with surface plasmon excitation. *Solid State Commun.* **41,** 499–501 (1982).
71. Hua, X. M. & Gersten, J. I. Theory of second-harmonic generation by small metal spheres. *Phys. Rev. B* **33,** 3756–3764 (1986).
72. Vance, F. W., Lemon, B. I. & Hupp, J. T. Enormous Hyper-Rayleigh Scattering from Nanocrystalline Gold Particle Suspensions. *J. Phys. Chem. B* **102,** 10091–10093 (1998).
73. Staedler, D. *et al.* Harmonic Nanocrystals for Biolabeling: A Survey of Optical Properties and Biocompatibility. *ACS Nano* **6,** 2542–2549 (2012).
74. Dadap, J. I., Shan, J., Eisenthal, K. B. & Heinz, T. F. Second-Harmonic Rayleigh Scattering from a Sphere of Centrosymmetric Material. *Phys. Rev. Lett.* **83,** 4045–4048 (1999).
75. Dadap, J. I., Shan, J. & Heinz, T. F. Theory of optical second-harmonic generation from a sphere of centrosymmetric material: small-particle limit. *J. Opt. Soc. Am. B* **21,** 1328 (2004).
76. Butet, J., Brevet, P.-F. & Martin, O. J. F. Optical Second Harmonic Generation in Plasmonic Nanostructures: From Fundamental Principles to Advanced Applications. *ACS Nano* **9,** 10545–10562 (2015).
77. Louis, C. & Pluchery, O. *Gold nanoparticles for physics, chemistry and biology*. (Imperial College Press ; Distributed by World Scientific Pub. Co, 2012).
78. Cao, G. & Wang, Y. *Nanostructures and Nanomaterials: Synthesis, Properties, and Applications*. (World Scientific Publishing Company, 2011).
79. Alex, S. & Tiwari, A. Functionalized Gold Nanoparticles: Synthesis, Properties and Applications—A Review. *J. Nanosci. Nanotechnol.* **15,** 1869–1894 (2015).
80. Murphy, C. J. *et al.* Anisotropic Metal Nanoparticles: Synthesis, Assembly, and Optical Applications. *J. Phys. Chem. B* **109,** 13857–13870 (2005).
81. Burda, C., Chen, X., Narayanan, R. & El-Sayed, M. A. Chemistry and Properties of Nanocrystals of Different Shapes. *Chem. Rev.* **105,** 1025–1102 (2005).
82. Sau, T. K., Rogach, A. L., Jäckel, F., Klar, T. A. & Feldmann, J. Properties and Applications of Colloidal Nonspherical Noble Metal Nanoparticles. *Adv. Mater.* **22,** 1805–1825 (2010).
83. Talapin, D. V., Lee, J.-S., Kovalenko, M. V. & Shevchenko, E. V. Prospects of Colloidal Nanocrystals for Electronic and Optoelectronic Applications. *Chem. Rev.* **110,** 389–458 (2010).
84. Cuenya, B. R. Synthesis and catalytic properties of metal nanoparticles: Size, shape, support, composition, and oxidation state effects. *Thin Solid Films* **518,** 3127–3150 (2010).
85. Daniel, M.-C. & Astruc, D. Gold nanoparticles: assembly, supramolecular chemistry, quantum-size-related properties, and applications toward biology, catalysis, and nanotechnology. *Chem. Rev.* **104,** 293–346 (2004).

86. Eustis, S. & El-Sayed, M. A. Why gold nanoparticles are more precious than pretty gold: Noble metal surface plasmon resonance and its enhancement of the radiative and nonradiative properties of nanocrystals of different shapes. *Chem. Soc. Rev.* **35,** 209–217 (2006).
87. Sardar, R., Funston, A. M., Mulvaney, P. & Murray, R. W. Gold Nanoparticles: Past, Present, and Future. *Langmuir* **25,** 13840–13851 (2009).
88. Zhou, J., Ralston, J., Sedev, R. & Beattie, D. A. Functionalized gold nanoparticles: synthesis, structure and colloid stability. *J. Colloid Interface Sci.* **331,** 251–262 (2009).
89. Rosi, N. L. & Mirkin, C. A. Nanostructures in biodiagnostics. *Chem. Rev.* **105,** 1547–1562 (2005).
90. Giljohann, D. A. *et al.* Gold nanoparticles for biology and medicine. *Angew. Chem. Int. Ed Engl.* **49,** 3280–3294 (2010).
91. Saha, K., Agasti, S. S., Kim, C., Li, X. & Rotello, V. M. Gold Nanoparticles in Chemical and Biological Sensing. *Chem. Rev.* **112,** 2739–2779 (2012).
92. Boisselier, E. & Astruc, D. Gold nanoparticles in nanomedicine: preparations, imaging, diagnostics, therapies and toxicity. *Chem. Soc. Rev.* **38,** 1759–1782 (2009).
93. Anker, J. N. *et al.* Biosensing with plasmonic nanosensors. *Nat. Mater.* **7,** 442–453 (2008).
94. Sperling, R. A., Gil, P. R., Zhang, F., Zanella, M. & Parak, W. J. Biological applications of gold nanoparticles. *Chem. Soc. Rev.* **37,** 1896–1908 (2008).
95. Hunt, L. B. The true story of Purple of Cassius. *Gold Bull.* **9,** 134–139 (1976).
96. Horikoshi, S. & Serpone, N. in *Microwaves in Nanoparticle Synthesis* (eds. Horikoshi, S. & Serpone, N.) 1–24 (Wiley, 2013).
97. Jin, R. *et al.* Photoinduced Conversion of Silver Nanospheres to Nanoprisms. *Science* **294,** 1901–1903 (2001).
98. Faraday, M. The Bakerian Lecture: Experimental Relations of Gold (and Other Metals) to Light. *Philos. Trans. R. Soc. Lond.* **147,** 145–181 (1857).
99. Graham, T. Liquid Diffusion Applied to Analysis. *Philos. Trans. R. Soc. Lond.* **151,** 183–224 (1861).
100. Vajtai, R. *Springer Handbook of Nanomaterials*. (Springer Berlin Heidelberg, 2013).
101. Mie, G. Beiträge zur Optik trüber Medien, speziell kolloidaler Metallösungen. *Ann. Phys.* **330,** 377–445 (1908).
102. Russell, A. D. & Hugo, W. B. Antimicrobial activity and action of silver. *Prog. Med. Chem.* **31,** 351–370 (1994).
103. Lea, M. C. Allotropic forms of silver. *Am. J. Sci.* **s3-37,** 476–491 (1889).
104. Frens, D. G. & Overbeek, J. T. G. Carey Lea's colloidal silver. *Kolloid-Z. Z. Für Polym.* **233,** 922–929 (1969).
105. San, B. H. *et al.* Combining Protein-Shelled Platinum Nanoparticles with Graphene to Build a Bionanohybrid Capacitor. *ACS Nano* **8,** 12120–12129 (2014).
106. Hong, J. W. *et al.* Controlled Synthesis of Pd–Pt Alloy Hollow Nanostructures with Enhanced Catalytic Activities for Oxygen Reduction. *ACS Nano* **6,** 2410–2419 (2012).
107. Wickman, B., Seidel, Y. E., Jusys, Z., Kasemo, B. & Behm, R. J. Fabrication of Pt/Ru Nanoparticle Pair Arrays with Controlled Separation and their Electrocatalytic Properties. *ACS Nano* **5,** 2547–2558 (2011).
108. Yang, W., Ma, Y., Tang, J. & Yang, X. 'Green synthesis' of monodisperse Pt nanoparticles and their catalytic properties. *Colloids Surf. Physicochem. Eng. Asp.* **302,** 628–633 (2007).
109. Venu, R., Ramulu, T. S., Anandakumar, S., Rani, V. S. & Kim, C. G. Bio-directed synthesis of platinum nanoparticles using aqueous honey solutions and their catalytic applications. *Colloids Surf. Physicochem. Eng. Asp.* **384,** 733–738 (2011).
110. Rigsby, M. A. *et al.* Experiment and Theory of Fuel Cell Catalysis: Methanol and Formic Acid Decomposition on Nanoparticle Pt/Ru. *J. Phys. Chem. C* **112,** 15595–15601 (2008).

111. Kang, Y. *et al.* Highly Active Pt_3Pb and Core–Shell Pt_3Pb–Pt Electrocatalysts for Formic Acid Oxidation. *ACS Nano* **6,** 2818–2825 (2012).
112. Zhai, D. *et al.* Highly Sensitive Glucose Sensor Based on Pt Nanoparticle/Polyaniline Hydrogel Heterostructures. *ACS Nano* **7,** 3540–3546 (2013).
113. Lu, J., Do, I., Drzal, L. T., Worden, R. M. & Lee, I. Nanometal-Decorated Exfoliated Graphite Nanoplatelet Based Glucose Biosensors with High Sensitivity and Fast Response. *ACS Nano* **2,** 1825–1832 (2008).
114. Kye, J. *et al.* Platinum Monolayer Electrocatalyst on Gold Nanostructures on Silicon for Photoelectrochemical Hydrogen Evolution. *ACS Nano* **7,** 6017–6023 (2013).
115. Liao, S., Holmes, K.-A., Tsaprailis, H. & Birss, V. I. High Performance PtRuIr Catalysts Supported on Carbon Nanotubes for the Anodic Oxidation of Methanol. *J. Am. Chem. Soc.* **128,** 3504–3505 (2006).
116. Shiju, N. R. & Guliants, V. V. Recent developments in catalysis using nanostructured materials. *Appl. Catal. Gen.* **356,** 1–17 (2009).
117. Subhramannia, M. & Pillai, V. K. Shape-dependent electrocatalytic activity of platinum nanostructures. *J. Mater. Chem.* **18,** 5858 (2008).
118. Long, N. V. *et al.* Synthesis and characterization of polyhedral Pt nanoparticles: Their catalytic property, surface attachment, self-aggregation and assembly. *J. Colloid Interface Sci.* **359,** 339–350 (2011).
119. Wang, C., Daimon, H., Lee, Y., Kim, J. & Sun, S. Synthesis of Monodisperse Pt Nanocubes and Their Enhanced Catalysis for Oxygen Reduction. *J. Am. Chem. Soc.* **129,** 6974–6975 (2007).
120. He, D., Mu, S. & Pan, M. Perfluorosulfonic acid-functionalized Pt/carbon nanotube catalysts with enhanced stability and performance for use in proton exchange membrane fuel cells. *Carbon* **49,** 82–88 (2011).
121. Kundu, P. *et al.* Ultrafast Microwave-Assisted Route to Surfactant-Free Ultrafine Pt Nanoparticles on Graphene: Synergistic Co-reduction Mechanism and High Catalytic Activity. *Chem. Mater.* **23,** 2772–2780 (2011).
122. Peng, Z. & Yang, H. Designer platinum nanoparticles: Control of shape, composition in alloy, nanostructure and electrocatalytic property. *Nano Today* **4,** 143–164 (2009).
123. Manthiram, A., Murugan, A. V., Sarkar, A. & Muraliganth, T. Nanostructured electrode materials for electrochemical energy storage and conversion. *Energy Environ. Sci.* **1,** 621–638 (2008).
124. Ahmadi, T. S., Wang, Z. L., Green, T. C., Henglein, A. & El-Sayed, M. A. Shape-Controlled Synthesis of Colloidal Platinum Nanoparticles. *Science* **272,** 1924–1926 (1996).
125. Liao, H.-G., Jiang, Y.-X., Zhou, Z.-Y., Chen, S.-P. & Sun, S.-G. Shape-controlled synthesis of gold nanoparticles in deep eutectic solvents for studies of structure-functionality relationships in electrocatalysis. *Angew. Chem. Int. Ed Engl.* **47,** 9100–9103 (2008).
126. Zhou, Z.-Y., Tian, N., Huang, Z.-Z., Chen, D.-J. & Sun, S.-G. Nanoparticle catalysts with high energy surfaces and enhanced activity synthesized by electrochemical method. *Faraday Discuss.* **140,** 81–92; discussion 93–112 (2008).
127. Chen, A. & Holt-Hindle, P. Platinum-Based Nanostructured Materials: Synthesis, Properties, and Applications. *Chem. Rev.* **110,** 3767–3804 (2010).
128. Willets, K. A. & Van Duyne, R. P. Localized Surface Plasmon Resonance Spectroscopy and Sensing. *Annu. Rev. Phys. Chem.* **58,** 267–297 (2007).
129. Kumar, C. *UV-VIS and Photoluminescence Spectroscopy for Nanomaterials Characterization*. (Springer Berlin Heidelberg, 2013).
130. Njoki, P. N. *et al.* Size Correlation of Optical and Spectroscopic Properties for Gold Nanoparticles. *J. Phys. Chem. C* **111,** 14664–14669 (2007).
131. Xue, C. & Mirkin, C. A. pH-Switchable Silver Nanoprism Growth Pathways. *Angew. Chem. Int. Ed.* **46,** 2036–2038 (2007).

132. Chen, H., Kou, X., Yang, Z., Ni, W. & Wang, J. Shape- and Size-Dependent Refractive Index Sensitivity of Gold Nanoparticles. *Langmuir* **24,** 5233–5237 (2008).
133. Nikoobakht, B. & El-Sayed, M. A. Preparation and Growth Mechanism of Gold Nanorods (NRs) Using Seed-Mediated Growth Method. *Chem. Mater.* **15,** 1957–1962 (2003).
134. Link, S., Mohamed, M. B. & El-Sayed, M. A. Simulation of the Optical Absorption Spectra of Gold Nanorods as a Function of Their Aspect Ratio and the Effect of the Medium Dielectric Constant. *J. Phys. Chem. B* **103,** 3073–3077 (1999).
135. Norman, T. J. *et al.* Near Infrared Optical Absorption of Gold Nanoparticle Aggregates. *J. Phys. Chem. B* **106,** 7005–7012 (2002).
136. Kelly, K. L., Coronado, E., Zhao, L. L. & Schatz, G. C. The Optical Properties of Metal Nanoparticles: The Influence of Size, Shape, and Dielectric Environment. *J. Phys. Chem. B* **107,** 668–677 (2003).
137. Xiao, Y., Shlyahovsky, B., Popov, I., Pavlov, V. & Willner, I. Shape and Color of Au Nanoparticles Follow Biocatalytic Processes. *Langmuir* **21,** 5659–5662 (2005).
138. Lee, K.-S. & El-Sayed, M. A. Gold and Silver Nanoparticles in Sensing and Imaging: Sensitivity of Plasmon Response to Size, Shape, and Metal Composition. *J. Phys. Chem. B* **110,** 19220–19225 (2006).
139. Orendorff, C. J., Sau, T. K. & Murphy, C. J. Shape-Dependent Plasmon-Resonant Gold Nanoparticles. *Small* **2,** 636–639 (2006).
140. Geneviève, M. *et al.* Biofunctionalization of gold nanoparticles and their spectral properties. *Microelectron. Eng.* **84,** 1710–1713 (2007).
141. Huang, H.-C. *et al.* Optically responsive gold nanorod-polypeptide assemblies. *Langmuir ACS J. Surf. Colloids* **24,** 14139–14144 (2008).
142. Nguyen, D. T., Kim, D.-J. & Kim, K.-S. Controlled synthesis and biomolecular probe application of gold nanoparticles. *Micron* **42,** 207–227 (2011).
143. Griffin, J. *et al.* Sequence-Specific HCV RNA Quantification Using the Size-Dependent Nonlinear Optical Properties of Gold Nanoparticles. *Small* **5,** 839–845 (2009).
144. Nappa, J., Russier-Antoine, I., Benichou, E., Jonin, C. & Brevet, P. F. Second harmonic generation from small gold metallic particles: From the dipolar to the quadrupolar response. *J. Chem. Phys.* **125,** 184712 (2006).
145. Chandra, M. & Das, P. K. 'Small-particle limit' in the second harmonic generation from noble metal nanoparticles. *Chem. Phys.* **358,** 203–208 (2009).
146. Salomon, A., Zielinski, M., Kolkowski, R., Zyss, J. & Prior, Y. Size and Shape Resonances in Second Harmonic Generation from Silver Nanocavities. *J. Phys. Chem. C* **117,** 22377–22382 (2013).
147. Schön, P. *et al.* Enhanced second-harmonic generation from individual metallic nanoapertures. *Opt. Lett.* **35,** 4063 (2010).
148. Xu, T., Jiao, X., Zhang, G.-P. & Blair, S. Second-harmonic emission from sub-wavelength apertures: Effects of aperture symmetry and lattice arrangement. *Opt. Express* **15,** 13894 (2007).
149. Klein, M. W., Enkrich, C., Wegener, M. & Linden, S. Second-Harmonic Generation from Magnetic Metamaterials. *Science* **313,** 502–504 (2006).
150. Ciracì, C., Poutrina, E., Scalora, M. & Smith, D. R. Origin of second-harmonic generation enhancement in optical split-ring resonators. *Phys. Rev. B* **85,** 201403 (2012).
151. Linden, S. *et al.* Collective Effects in Second-Harmonic Generation from Split-Ring-Resonator Arrays. *Phys. Rev. Lett.* **109,** 015502 (2012).
152. Valev, V. K. *et al.* Plasmonic Ratchet Wheels: Switching Circular Dichroism by Arranging Chiral Nanostructures. *Nano Lett.* **9,** 3945–3948 (2009).
153. Mamonov, E. A. *et al.* Anisotropy versus circular dichroism in second harmonic generation from fourfold symmetric arrays of G-shaped nanostructures. *Phys. Rev. B* **89,** 121113 (2014).

154. Valev, V. K., Baumberg, J. J., Sibilia, C. & Verbiest, T. Chirality and Chiroptical Effects in Plasmonic Nanostructures: Fundamentals, Recent Progress, and Outlook. *Adv. Mater.* **25,** 2517–2534 (2013).
155. Kolkowski, R., Petti, L., Rippa, M., Lafargue, C. & Zyss, J. Octupolar Plasmonic Meta-Molecules for Nonlinear Chiral Watermarking at Subwavelength Scale. *ACS Photonics* **2,** 899–906 (2015).
156. Kujala, S., Canfield, B. K., Kauranen, M., Svirko, Y. & Turunen, J. Multipole Interference in the Second-Harmonic Optical Radiation from Gold Nanoparticles. *Phys. Rev. Lett.* **98,** 167403 (2007).
157. Czaplicki, R. *et al.* Dipole limit in second-harmonic generation from arrays of gold nanoparticles. *Opt. Express* **19,** 26866 (2011).
158. Kujala, S., Canfield, B. K., Kauranen, M., Svirko, Y. & Turunen, J. Multipolar analysis of second-harmonic radiation from gold nanoparticles. *Opt. Express* **16,** 17196 (2008).
159. Agarwal, A. *et al.* Targeted gold nanorod contrast agent for prostate cancer detection by photoacoustic imaging. *J. Appl. Phys.* **102,** 064701 (2007).
160. Tagad, C. K. *et al.* Green synthesis of silver nanoparticles and their application for the development of optical fiber based hydrogen peroxide sensor. *Sens. Actuators B Chem.* **183,** 144–149 (2013).
161. Singh, P., Kim, Y.-J., Zhang, D. & Yang, D.-C. Biological Synthesis of Nanoparticles from Plants and Microorganisms. *Trends Biotechnol.* **0,** (2016).
162. Zeng, S. *et al.* A Review on Functionalized Gold Nanoparticles for Biosensing Applications. *Plasmonics* **6,** 491–506 (2011).
163. Radwan, S. H. & Azzazy, H. M. Gold nanoparticles for molecular diagnostics. *Expert Rev. Mol. Diagn.* **9,** 511–524 (2009).
164. Haick, H. Chemical sensors based on molecularly modified metallic nanoparticles. *J. Phys. Appl. Phys.* **40,** 7173 (2007).
165. Zayats, M., Baron, R., Popov, I. & Willner, I. Biocatalytic Growth of Au Nanoparticles: From Mechanistic Aspects to Biosensors Design. *Nano Lett.* **5,** 21–25 (2005).
166. Bunz, U. H. F. & Rotello, V. M. Gold Nanoparticle–Fluorophore Complexes: Sensitive and Discerning 'Noses' for Biosystems Sensing. *Angew. Chem. Int. Ed.* **49,** 3268–3279 (2010).
167. Zhao, W., Brook, M. A. & Li, Y. Design of Gold Nanoparticle-Based Colorimetric Biosensing Assays. *ChemBioChem* **9,** 2363–2371 (2008).
168. You, C.-C. *et al.* Detection and identification of proteins using nanoparticle–fluorescent polymer 'chemical nose' sensors. *Nat. Nanotechnol.* **2,** 318–323 (2007).
169. Anderson, J. A. CO oxidation over alumina supported platinum catalyst. *Catal. Lett.* **13,** 363–369 (1992).
170. McClure, S. M. & Goodman, D. W. New insights into catalytic CO oxidation on Pt-group metals at elevated pressures. *Chem. Phys. Lett.* **469,** 1–13 (2009).
171. Li, S., Dou, X., Yang, Y. & Xin, H. Supported Au, Pt Catalysts in the Reaction of CO Oxidation. *Rev. Adv. Sci. Eng.* **4,** 163–171 (2015).
172. Rashkeev, S. N., Lupini, A. R., Overbury, S. H., Pennycook, S. J. & Pantelides, S. T. Role of the nanoscale in catalytic CO oxidation by supported Au and Pt nanostructures. *Phys. Rev. B* **76,** 035438 (2007).
173. Haruta, M. *et al.* Low-Temperature Oxidation of CO over Gold Supported on TiO2, α-Fe2O3, and Co3O4. *J. Catal.* **144,** 175–192 (1993).
174. Liu, H. *et al.* Active Oxygen Species and Mechanism for Low-Temperature CO Oxidation Reaction on a TiO2-Supported Au Catalyst Prepared from Au(PPh3)(NO3) and As-Precipitated Titanium Hydroxide. *J. Catal.* **185,** 252–264 (1999).
175. Saavedra, J., Powell, C., Panthi, B., Pursell, C. J. & Chandler, B. D. CO oxidation over Au/TiO2 catalyst: Pretreatment effects, catalyst deactivation, and carbonates production. *J. Catal.* **307,** 37–47 (2013).
176. Bond, G. C. & Thompson, D. T. Gold-catalysed oxidation of carbon monoxide. *Gold Bull.* **33,** 41–50 (2000).

177. Butet, J. *et al.* Interference between Selected Dipoles and Octupoles in the Optical Second-Harmonic Generation from Spherical Gold Nanoparticles. *Phys. Rev. Lett.* **105,** (2010).
178. Zhang, Y., Grady, N. K., Ayala-Orozco, C. & Halas, N. J. Three-Dimensional Nanostructures as Highly Efficient Generators of Second Harmonic Light. *Nano Lett.* **11,** 5519–5523 (2011).
179. Butet, J. *et al.* Optical Second Harmonic Generation of Single Metallic Nanoparticles Embedded in a Homogeneous Medium. *Nano Lett.* **10,** 1717–1721 (2010).
180. Husu, H. *et al.* Metamaterials with Tailored Nonlinear Optical Response. *Nano Lett.* **12,** 673–677 (2012).
181. Bautista, G. *et al.* Second-Harmonic Generation Imaging of Metal Nano-Objects with Cylindrical Vector Beams. *Nano Lett.* **12,** 3207–3212 (2012).
182. Sauerbeck, C. *et al.* Shedding Light on the Growth of Gold Nanoshells. *ACS Nano* **8,** 3088–3096 (2014).
183. Butet, J. *et al.* Sensing with Multipolar Second Harmonic Generation from Spherical Metallic Nanoparticles. *Nano Lett.* **12,** 1697–1701 (2012).
184. Billot, L. *et al.* Surface enhanced Raman scattering on gold nanowire arrays: Evidence of strong multipolar surface plasmon resonance enhancement. *Chem. Phys. Lett.* **422,** 303–307 (2006).
185. Mendes, P. M. *et al.* Gold Nanoparticle Patterning of Silicon Wafers Using Chemical e-Beam Lithography. *Langmuir* **20,** 3766–3768 (2004).
186. Smythe, E. J., Cubukcu, E. & Capasso, F. Optical properties of surface plasmon resonances of coupled metallic nanorods. *Opt. Express* **15,** 7439 (2007).
187. Birtcher, R. C., Donnelly, S. E. & Schlutig, S. Nanoparticle ejection from gold during ion irradiation. *Nucl. Instrum. Methods Phys. Res. Sect. B Beam Interact. Mater. At.* **215,** 69–75 (2004).
188. Lung, J.-K. *et al.* Preparation of gold nanoparticles by arc discharge in water. *J. Alloys Compd.* **434–435,** 655–658 (2007).
189. Sakamoto, M., Fujistuka, M. & Majima, T. Light as a construction tool of metal nanoparticles: Synthesis and mechanism. *J. Photochem. Photobiol. C Photochem. Rev.* **10,** 33–56 (2009).
190. Zhou, Y., Wang, C. Y., Zhu, Y. R. & Chen, Z. Y. A Novel Ultraviolet Irradiation Technique for Shape-Controlled Synthesis of Gold Nanoparticles at Room Temperature. *Chem. Mater.* **11,** 2310–2312 (1999).
191. Krinke, T. J., Deppert, K., Magnusson, M. H., Schmidt, F. & Fissan, H. Microscopic aspects of the deposition of nanoparticles from the gas phase. *J. Aerosol Sci.* **33,** 1341–1359 (2002).
192. Li, Q. *Anisotropic Nanomaterials-Preparation, Properties, and Applications*. (Springer International Publishing, 2015).
193. Fang, F. & Xu, Z. in *CIRP Encyclopedia of Production Engineering* (eds. Laperrière, L., Reinhart, G. & Engineering, T. I. A. for P.) 717–721 (Springer Berlin Heidelberg, 2014).
194. Turkevich, J., Stevenson, P. C. & Hillier, J. A study of the nucleation and growth processes in the synthesis of colloidal gold. *Discuss. Faraday Soc.* **11,** 55–75 (1951).
195. Frens, G. Controlled Nucleation for the Regulation of the Particle Size in Monodisperse Gold Suspensions. *Nature* **241,** 20–22 (1973).
196. Szunerits, S., Spadavecchia, J. & Boukherroub, R. Surface plasmon resonance: signal amplification using colloidal gold nanoparticles for enhanced sensitivity. *Rev. Anal. Chem.* **33,** 153–164 (2014).
197. Voliani, V. *Update on gold nanoparticles: from cathedral windows to nanomedicine*. (Smithers Rapra, 2013).
198. Brust, M., Walker, M., Bethell, D., Schiffrin, D. J. & Whyman, R. Synthesis of thiol-derivatised gold nanoparticles in a two-phase Liquid–Liquid system. *J. Chem. Soc. Chem. Commun.* 801–802 (1994).
199. Liz-Marzán, L. M. Gold nanoparticle research before and after the Brust–Schiffrin method. *Chem. Commun.* **49,** 16–18 (2012).
200. Kiely, C. J., Fink, J., Brust, M., Bethell, D. & Schiffrin, D. J. Spontaneous ordering of bimodal ensembles of nanoscopic gold clusters. *Nature* **396,** 444–446 (1998).

201. Bigall, N. C. *et al.* Monodisperse Platinum Nanospheres with Adjustable Diameters from 10 to 100 nm: Synthesis and Distinct Optical Properties. *Nano Lett.* **8,** 4588–4592 (2008).
202. Lu, X., Rycenga, M., Skrabalak, S. E., Wiley, B. & Xia, Y. Chemical Synthesis of Novel Plasmonic Nanoparticles. *Annu. Rev. Phys. Chem.* **60,** 167–192 (2009).
203. Sajanlal, P. R. & Pradeep, T. Mesoflowers: A new class of highly efficient surface-enhanced Raman active and infrared-absorbing materials. *Nano Res.* **2,** 306–320 (2009).
204. Sajanlal, P. R., Sreeprasad, T. S., Samal, A. K. & Pradeep, T. Anisotropic nanomaterials: structure, growth, assembly, and functions. *Nano Rev.* **2,** (2011).
205. Niu, W., Zhang, L. & Xu, G. Seed-mediated growth of noble metal nanocrystals: crystal growth and shape control. *Nanoscale* **5,** 3172 (2013).
206. Murphy, C. J., Gole, A. M., Hunyadi, S. E. & Orendorff, C. J. One-Dimensional Colloidal Gold and Silver Nanostructures. *Inorg. Chem.* **45,** 7544–7554 (2006).
207. Gole, A. & Murphy, C. J. Seed-Mediated Synthesis of Gold Nanorods: Role of the Size and Nature of the Seed. *Chem. Mater.* **16,** 3633–3640 (2004).
208. Sau, T. K. & Murphy, C. J. Seeded High Yield Synthesis of Short Au Nanorods in Aqueous Solution. *Langmuir* **20,** 6414–6420 (2004).
209. Wu, H.-Y., Chu, H.-C., Kuo, T.-J., Kuo, C.-L. & Huang, M. H. Seed-Mediated Synthesis of High Aspect Ratio Gold Nanorods with Nitric Acid. *Chem. Mater.* **17,** 6447–6451 (2005).
210. Kundu, S. & Liang, H. Photoinduced Formation of Shape-Selective Pt Nanoparticles. *Langmuir* **26,** 6720–6727 (2010).
211. Xiong, Y. & Xia, Y. Shape-Controlled Synthesis of Metal Nanostructures: The Case of Palladium. *Adv. Mater.* **19,** 3385–3391 (2007).
212. Ray, P. C. Size and Shape Dependent Second Order Nonlinear Optical Properties of Nanomaterials and Their Application in Biological and Chemical Sensing. *Chem. Rev.* **110,** 5332–5365 (2010).
213. Maker, P. D. Spectral Broadening of Elastic Second-Harmonic Light Scattering in Liquids. *Phys. Rev. A* **1,** 923–951 (1970).
214. Brasselet, S. & Zyss, J. Multipolar molecules and multipolar fields: probing and controlling the tensorial nature of nonlinear molecular media. *J. Opt. Soc. Am. B* **15,** 257 (1998).
215. Brasselet, S. & Zyss, J. Relation between quantum and geometric dimensionalities in molecular nonlinear optics: beyond the two-level model for anisotropic systems. *J. Nonlinear Opt. Phys. Mater.* **05,** 671–693 (1996).
216. Darbha, G. K., Rai, U. S., Singh, A. K. & Ray, P. C. Gold-Nanorod-Based Sensing of Sequence Specific HIV-1 Virus DNA by Using Hyper-Rayleigh Scattering Spectroscopy. *Chem. – Eur. J.* **14,** 3896–3903 (2008).
217. Yi, T. *et al.* J-Aggregated Dye–MnPS3 Hybrid Nanoparticles with Giant Quadratic Optical Nonlinearity. *Adv. Mater.* **17,** 335–338 (2005).
218. Le Bozec, H. *et al.* Supramolecular Octupolar Self-Ordering Towards Nonlinear Optics. *Adv. Mater.* **13,** 1677–1681 (2001).
219. Capretti, A., Pecora, E. F., Forestiere, C., Dal Negro, L. & Miano, G. Size-dependent second-harmonic generation from gold nanoparticles. *Phys. Rev. B* **89,** 125414 (2014).
220. Pang, X., He, D., Luo, S. & Cai, Q. An amperometric glucose biosensor fabricated with Pt nanoparticle-decorated carbon nanotubes/TiO2 nanotube arrays composite. *Sens. Actuators B Chem.* **137,** 134–138 (2009).
221. Dey, R. S. & Raj, C. R. Development of an Amperometric Cholesterol Biosensor Based on Graphene−Pt Nanoparticle Hybrid Material. *J. Phys. Chem. C* **114,** 21427–21433 (2010).
222. Sankaran, K. J. *et al.* Gold nanoparticle-ultrananocrystalline diamond hybrid structured materials for high-performance optoelectronic device applications. *Nanoscale* **7,** 4377–4385 (2015).

223. Hu, M.-S. *et al.* Photosensitive gold-nanoparticle-embedded dielectric nanowires. *Nat Mater* **5,** 102–106 (2006).
224. Law, W.-C., Yong, K.-T., Baev, A. & Prasad, P. N. Sensitivity Improved Surface Plasmon Resonance Biosensor for Cancer Biomarker Detection Based on Plasmonic Enhancement. *ACS Nano* **5,** 4858–4864 (2011).
225. Ghosh, S. K., Alam, M. M. & Mandal, D. The in situ formation of platinum nanoparticles and their catalytic role in electroactive phase formation in poly(vinylidene fluoride): a simple preparation of multifunctional poly(vinylidene fluoride) films doped with platinum nanoparticles. *RSC Adv* **4,** 41886–41894 (2014).
226. Ren, X., Meng, X., Chen, D., Tang, F. & Jiao, J. Using silver nanoparticle to enhance current response of biosensor. *Biosens. Bioelectron.* **21,** 433–437 (2005).
227. Choi, H. *et al.* Versatile surface plasmon resonance of carbon-dot-supported silver nanoparticles in polymer optoelectronic devices. *Nat Photon* **7,** 732–738 (2013).
228. Bastús, N. G., Comenge, J. & Puntes, V. Kinetically Controlled Seeded Growth Synthesis of Citrate-Stabilized Gold Nanoparticles of up to 200 nm: Size Focusing versus Ostwald Ripening. *Langmuir* **27,** 11098–11105 (2011).
229. Perrault, S. D. & Chan, W. C. W. Synthesis and Surface Modification of Highly Monodispersed, Spherical Gold Nanoparticles of 50−200 nm. *J. Am. Chem. Soc.* **131,** 17042–17043 (2009).
230. Busbee, B. d., Obare, S. o. & Murphy, C. j. An Improved Synthesis of High-Aspect-Ratio Gold Nanorods. *Adv. Mater.* **15,** 414–416 (2003).
231. Jana, N. R., Gearheart, L. & Murphy, C. J. Wet Chemical Synthesis of High Aspect Ratio Cylindrical Gold Nanorods. *J. Phys. Chem. B* **105,** 4065–4067 (2001).
232. Murphy, C. J., Sau, T. K., Gole, A. & Orendorff, C. J. Surfactant-Directed Synthesis and Optical Properties of One-Dimensional Plasmonic Metallic Nanostructures. *MRS Bull.* **30,** 349–355 (2005).
233. Huang, X., Neretina, S. & El-Sayed, M. A. Gold Nanorods: From Synthesis and Properties to Biological and Biomedical Applications. *Adv. Mater.* **21,** 4880–4910 (2009).
234. Pérez-Juste, J., Pastoriza-Santos, I., Liz-Marzán, L. M. & Mulvaney, P. Gold nanorods: Synthesis, characterization and applications. *Coord. Chem. Rev.* **249,** 1870–1901 (2005).
235. Murphy, C. J. *et al.* Gold nanorod crystal growth: From seed-mediated synthesis to nanoscale sculpting. *Curr. Opin. Colloid Interface Sci.* **16,** 128–134 (2011).
236. Hao, E., Bailey, R. C., Schatz, G. C., Hupp, J. T. & Li, S. Synthesis and Optical Properties of 'Branched' Gold Nanocrystals. *Nano Lett.* **4,** 327–330 (2004).
237. Nehl, C. L., Liao, H. & Hafner, J. H. Optical Properties of Star-Shaped Gold Nanoparticles. *Nano Lett.* **6,** 683–688 (2006).
238. Boca, S., Rugina, D., Pintea, A., Barbu-Tudoran, L. & Astilean, S. Flower-shaped gold nanoparticles: synthesis, characterization and their application as SERS-active tags inside living cells. *Nanotechnology* **22,** 055702 (2011).
239. Goubet, N., Ding, Y., Brust, M., Wang, Z. L. & Pileni, M.-P. A Way To Control the Gold Nanocrystals Size: Using Seeds with Different Sizes and Subjecting Them to Mild Annealing. *ACS Nano* **3,** 3622–3628 (2009).
240. Jain, T., Westerlund, F., Johnson, E., Moth-Poulsen, K. & Bjørnholm, T. Self-Assembled Nanogaps *via* Seed-Mediated Growth of End-to-End Linked Gold Nanorods. *ACS Nano* **3,** 828–834 (2009).
241. Wang, Y. *et al.* Synthesis of Silver Octahedra with Controlled Sizes and Optical Properties *via* Seed-Mediated Growth. *ACS Nano* **7,** 4586–4594 (2013).
242. Harfouch, Y. E. *et al.* Effect of a thioalkane capping layer on the first hyperpolarizabilities of gold and silver nanoparticles. *J. Phys. Condens. Matter* **24,** 124104 (2012).

243. Nappa, J., Russier-Antoine, I., Benichou, E., Jonin, C. & Brevet, P.-F. Wavelength dependence of the retardation effects in silver nanoparticles followed by polarization resolved hyper Rayleigh scattering. *Chem. Phys. Lett.* **415,** 246–250 (2005).
244. Johnson, P. B. & Christy, R. W. Optical Constants of the Noble Metals. *Phys. Rev. B* **6,** 4370–4379 (1972).
245. Hu, J.-Q. *et al.* A Simple and Effective Route for the Synthesis of Crystalline Silver Nanorods and Nanowires. *Adv. Funct. Mater.* **14,** 183–189 (2004).
246. Clays, K., Hendrickx, E., Triest, M. & Persoons, A. Second-order nonlinear optics in isotropic liquids: Hyper-Rayleigh scattering in solution. *J. Mol. Liq.* **67,** 133–155 (1995).
247. Gomez, L. *et al.* Stability and biocompatibility of photothermal gold nanorods after lyophilization and sterilization. *Mater. Res. Bull.* **48,** 4051–4057 (2013).
248. Kang, Y. *et al.* Shape-Controlled Synthesis of Pt Nanocrystals: The Role of Metal Carbonyls. *ACS Nano* **7,** 645–653 (2013).
249. Wang, L., Hu, C., Nemoto, Y., Tateyama, Y. & Yamauchi, Y. On the Role of Ascorbic Acid in the Synthesis of Single-Crystal Hyperbranched Platinum Nanostructures. *Cryst. Growth Des.* **10,** 3454–3460 (2010).
250. Mankin, M. N., Mazumder, V. & Sun, S. One-Pot Synthesis of Pt Nanocubes and Nanopods via Burst Nucleation and Controlled Secondary Growth. *Chem. Mater.* **23,** 132–136 (2011).
251. Song, H., Kim, F., Connor, S., Somorjai, G. A. & Yang, P. Pt Nanocrystals: Shape Control and Langmuir−Blodgett Monolayer Formation. *J. Phys. Chem. B* **109,** 188–193 (2005).
252. Hu, X., Wang, T. & Dong, S. Rapid Synthesis of Cubic Pt Nanoparticles and Their Use for the Preparation of Pt Nanoagglomerates. *J. Nanosci. Nanotechnol.* **6,** 2056–2061 (2006).
253. Yu, W., Tu, W. & Liu, H. Synthesis of Nanoscale Platinum Colloids by Microwave Dielectric Heating. *Langmuir* **15,** 6–9 (1999).
254. Miyabayashi, K., Nakamura, S. & Miyake, M. Synthesis of Small Platinum Cube with Less Than 3 nm by the Control of Growth Kinetics. *Cryst. Growth Des.* **11,** 4292–4295 (2011).
255. Teranishi, T., Hosoe, M., Tanaka, T. & Miyake, M. Size Control of Monodispersed Pt Nanoparticles and Their 2D Organization by Electrophoretic Deposition. *J. Phys. Chem. B* **103,** 3818–3827 (1999).
256. Palik, E. D. *Handbook of optical constants of solids*. (Academic Press, 1985).
257. Russier-Antoine, I. *et al.* Non-linear optical properties of gold quantum clusters. The smaller the better. *Nanoscale* **6,** 13572–13578 (2014).
258. Millstone, J. E., Hurst, S. J., Métraux, G. S., Cutler, J. I. & Mirkin, C. A. Colloidal gold and silver triangular nanoprisms. *Small* **5,** 646–664 (2009).
259. Chen, L. *et al.* High-Yield Seedless Synthesis of Triangular Gold Nanoplates through Oxidative Etching. *Nano Lett.* **14,** 7201–7206 (2014).
260. Ma, X. *et al.* PEGylated gold nanoprisms for photothermal therapy at low laser power density. *RSC Adv* **5,** 81682–81688 (2015).
261. Millstone, J. E., Métraux, G. S. & Mirkin, C. A. Controlling the Edge Length of Gold Nanoprisms via a Seed-Mediated Approach. *Adv. Funct. Mater.* **16,** 1209–1214 (2006).
262. Li, C., Cai, W., Li, Y., Hu, J. & Liu, P. Ultrasonically Induced Au Nanoprisms and Their Size Manipulation Based on Aging. *J. Phys. Chem. B* **110,** 1546–1552 (2006).
263. Scarabelli, L., Coronado-Puchau, M., Giner-Casares, J. J., Langer, J. & Liz-Marzán, L. M. Monodisperse Gold Nanotriangles: Size Control, Large-Scale Self-Assembly, and Performance in Surface-Enhanced Raman Scattering. *ACS Nano* **8,** 5833–5842 (2014).
264. Ha, T. H., Koo, H.-J. & Chung, B. H. Shape-Controlled Syntheses of Gold Nanoprisms and Nanorods Influenced by Specific Adsorption of Halide Ions. *J. Phys. Chem. C* **111,** 1123–1130 (2007).

265. Joshi, G. K. *et al.* Designing Efficient Localized Surface Plasmon Resonance-Based Sensing Platforms: Optimization of Sensor Response by Controlling the Edge Length of Gold Nanoprisms. *J. Phys. Chem. C* **116,** 20990–21000 (2012).
266. Millstone, J. E. *et al.* Observation of a Quadrupole Plasmon Mode for a Colloidal Solution of Gold Nanoprisms. *J. Am. Chem. Soc.* **127,** 5312–5313 (2005).
267. Pelaz, B. *et al.* Tailoring the Synthesis and Heating Ability of Gold Nanoprisms for Bioapplications. *Langmuir* **28,** 8965–8970 (2012).
268. Straney, P. J., Andolina, C. M. & Millstone, J. E. Seedless Initiation as an Efficient, Sustainable Route to Anisotropic Gold Nanoparticles. *Langmuir* **29,** 4396–4403 (2013).
269. DuChene, J. S. *et al.* Halide Anions as Shape-Directing Agents for Obtaining High-Quality Anisotropic Gold Nanostructures. *Chem. Mater.* **25,** 1392–1399 (2013).
270. Fan, X. *et al.* Size-controlled growth of colloidal gold nanoplates and their high-purity acquisition. *Nanotechnology* **21,** 105602 (2010).
271. Ah, C. S. *et al.* Size-Controlled Synthesis of Machinable Single Crystalline Gold Nanoplates. *Chem. Mater.* **17,** 5558–5561 (2005).
272. Shuford, K. L., Ratner, M. A. & Schatz, G. C. Multipolar excitation in triangular nanoprisms. *J. Chem. Phys.* **123,** 114713 (2005).
273. Oudar, J. L. Optical nonlinearities of conjugated molecules. Stilbene derivatives and highly polar aromatic compounds. *J. Chem. Phys.* **67,** 446–457 (1977).

université PARIS-SACLAY
ÉCOLE DOCTORALE
Physique et ingénierie : électrons, photons, sciences du vivant (EOBE)

Titre : Propriétés optiques non linéaires de molécules et de nanoparticules métalliques pour la photonique

Mots clés : optique non linéaire, nanoparticule, génération de second harmonique

Résumé : L'optique non linéaire est un outil très puissant pour l'étude des propriétés photoniques de molécules, de matériaux et de nanostructures. La taille et la forme des nanoparticules de métaux nobles (NMNPs) influencent fortement leurs propriétés optiques non linéaires du second ordre. Dans cette thèse, nous proposons une étude systématique de l'influence de la surface de nanoparticules sur leurs valeurs de première hyperpolarisabilité β. Des nanoparticules en poudre d'argent (de diamètres ~7 nm) ainsi que des solutions colloïdales sur NMNPs - avec différentes compositions, tailles et formes -ont été synthétisés : des nanosphères d'argent (de diamètres ~10 nm), des nanosphères d'or (de diamètres 3,0; 11,6; 15,8; 17,4; 20,0 et 43,0 nm), des nanobâtonnets d'or (de rapports d'aspect 1,47; 1,63 et 2,30), des nanobâtonnets d'argent (de rapports d'aspect 5,0; 6,3; 7,5; 8,2 et 9,7), des nanofleurs de platine (de diamètres 7,0; 8,0; 10,0; 14,0; 20,0 et 31,0 nm) ainsi que des nanoprismes d'or (d'une longueur de côtés de 47,5 à 112,3 nm). La diffusion harmonique de la lumière (HLS) à 1064 nm est utilisée pour étudier la génération du second harmonique des NMNPs colloïdaux, et d'en déduire leurs valeurs de première hyperpolarisabilité β. Pour les nanosphères et les nanobâtonnets étudiés dans ce travail, nous démontrons que leurs valeurs de β présentent une forte dépendance avec leur surface, qui est le paramètre dominant dans l'évolution des valeurs de β. Par ailleurs, la rugosité de la surface des particules ainsi que la forme des irrégularités des nanofleurs sont responsables de valeurs exceptionnellement élevées de β. En outre, nous démontrons expérimentalement, pour la première fois dans la littérature, que les valeurs de β des nanoprismes présentent non seulement une dépendance linéaire par rapport à la surface, mais sont également sensibles aux courbures des sommets du triangle.

Title : Nonlinear optical properties of molecules and metallic nanoparticles for photonics

Keywords : nonlinear optics, nanoparticle, second harmonic generation

Abstract : Nonlinear optics is well known to be a highly powerful tool to investigate the photonic properties of molecules, materials and nanostructures. Size and shape of noble metal nanoparticles (NMNPs) strongly influence their second-order nonlinear optical properties. In this PhD thesis, we propose a systematic investigation of the influence of the nanoparticle surface area on their first hyperpolarizability β values. Powdery-silver nanoparticles (diameters ~7 nm) and colloidal solutions on NMNPs with different composition, sizes and shapes have been synthesized, *i.e.* silver nanospheres (diameters ~10 nm), gold nanospheres (diameters 3.0; 11.6; 15.8; 17.4; 20.0 and 43 nm), gold nanorods (aspect ratios 1.47; 1.63 and 2.30), silver nanorods (aspect ratios 5.0; 6.3; 7.5; 8.2 and 9.7), platinum nanoflowers (diameters 7.0; 8.0; 10.0; 14.0; 20.0 and 31.0 nm) and gold nanoprisms (edge length tuned from 47.5 to 112.3 nm). Harmonic light scattering (HLS) at 1064 nm is used to investigate the second harmonic generation from colloidal NMNPs, and to infer their first hyperpolarizability tensor β. For the nanospheres and nanorods investigated in this work, we demonstrate that their β values display a strong dependence with their surface area, which is the dominant parameter in the evolution of β values. Otherwise, particle surface corrugation and shape irregularities of nanoflowers are responsible for exceptionally high β values. Moreover, we report for the first time in the literature that the β values of nanoprisms display not only a linear dependence with respect to the surface area, but are also sensitive to the sharpness of the triangle vertices.

Université Paris-Saclay
Espace Technologique / Immeuble Discovery
Route de l'Orme aux Merisiers RD 128 / 91190 Saint-Aubin, France